Tampere University

JUHANI VIRTANEN

Development of Measurement Concepts for Canine Dry Electrode Electrocardiogram and Human Cardiac Construct Contraction Force Measurements

Tampere University Dissertations 267

Tampere University Dissertations 267

JUHANI VIRTANEN

Development of Measurement Concepts for Canine Dry Electrode Electrocardiogram and Human Cardiac Construct Contraction Force Measurements

ACADEMIC DISSERTATION
To be presented, with the permission of
the Faculty of Medicine and Health Technology of Tampere University
for public discussion at Tampere University,
on 21 August 2020, at 12 o'clock.

ACADEMIC DISSERTATION
Tampere University, Faculty of Medicine and Health Technology (MET)
Finland

Responsible supervisor and Custos	Associate Professor Sampo Tuukkanen Tampere University Finland	
Supervisor	Docent Antti Vehkaoja Tampere University Finland	
Pre-examiners	Associate Professor Abdenbi Mohand-Ousaid Université de Franche-Comté France	Professor Tapio Fabritius University of Oulu Finland
Opponent	Professor Gijs Krijnen University of Twente The Netherlands	

The originality of this thesis has been checked using the Turnitin OriginalityCheck service.

Cover design: Roihu Inc.

ISBN 978-952-03-1596-2 (print)
ISBN 978-952-03-1597-9 (pdf)
ISSN 2489-9860 (print)
ISSN 2490-0028 (pdf)
http://urn.fi/URN:ISBN:978-952-03-1597-9

PunaMusta Oy – Yliopistopaino
Tampere 2020

ACKNOWLEDGEMENTS

This thesis work was carried out at Tampere University, Faculty of Medicine and Health technology under the Business Finland funded project 'Turre ja Toivoset 2.0' (Buddy and the Smiths 2.0) and Academy of Finland funded project 'Toiminnallinen ihmissolupohjainen sydänmalli biolääketieteelliseen tutkimukseen ja testaukseen' (*In Vitro* Cardio).

I would like to thank my thesis work supervisors Associate Professor Sampo Tuukkanen and Assistant Professor Antti Vehkaoja, and my thesis steering group member Assistant Professor Veikko Sariola for excellent guidance during the thesis writing and also enabling my personal growth as a scientist. I would like to express my gratitude to fellow researchers that have participated in the work. I feel honored to have been able to work with such great colleagues and inspiring community. I also thank Business Finland and Academy of Finland who funded my research and whose backing was critical. Without them the thesis work would not have been possible.

I would also thank my son Vesa and daughter Salla for the support during this endeavor and for the most inspiring discussions about the thesis covering technology, biology and physics.

.

Tampere, May 3, 2020
Juhani Virtanen

ABSTRACT

Interest towards personal health has been growing during recent years. Heart rate (HR) monitoring has become an everyday life practice. The importance of this can be put to a context with the fact that approximately 40% of human deaths are caused by cardiac diseases. In its most basic forms HR monitoring does not reveal all information which would be available with methods such as electrocardiogram (ECG).

The trend of health monitoring is also becoming more and more common with pets and animals. HR monitoring systems are available for these applications but as with humans they seldom offer opportunity to explore the ECG outside the clinical environment. There the equipment can be bulky and require attention to operate properly. Known issues with the ECG electrodes in animal applications are that they may require shaving, use of electrically conductive gel or may be painful for the animal. Therefore, low maintenance dry ECG electrodes would be beneficial for these applications.

Cardiac diseases can be treated with various therapy methods which often involve the use of cardiac drugs. Drug development however is expensive and time consuming. The development work includes drug toxicity testing which has been carried out with, for example, animal testing. This raises ethical questions in the development work. Also, it has been proven that these toxicity research results may not provide accurate information about the cardiac drug toxicity to humans; in addition, the efficiency of the drug may often vary from patient to patient. Advances in stem cell culturing has enabled the opportunity to fabricate human genome cardiac constructs which can be used in the drug testing. Action- and biopotential measurements can be carried out in the drug development testing procedures. However cardiac contraction force measurement has been proposed to reveal more information about the drug efficacy and toxicity than the biopotential measurements.

In this thesis two cardiac cycle measurement topics were studied 1) the dry canine ECG electrodes and 2) contraction force measurement system for human induced

cardiac constructs. In order to study anomalies and abnormalities of the measured cardiac cycles, a pattern matcher analysis method is proposed for a classification and detection of those.

Five different dry canine ECG electrodes were constructed, and their performance was tested. None of these ECG electrodes required shaving or application of electrically conductive gel. The testing procedure was used to resemble everyday use of the electrodes. The highest average proportion of the correctly detected heartbeats of 95% was achieved with gold plated electrodes in a standing and sitting posture while the lowest figure was 41% with 12- pin polymeric electrode during walking.

Cardiac construct contraction force was studied with a single and dual axis piezoelectric cantilever force measurement systems. These were developed, fabricated, and evaluated for contraction force measurement of cardiac constructs *in vitro*. Maximum measured contraction forces ranged from 3.0 to 11.2 μN during the cycle. The coefficient of variation of these force measurements varied from 1.0% to 16.8% depending on the configuration of the measurement.

CONTENTS

ABBREVIATIONS

ADC	Analog to digital conversion
ADP	Adenosine diphosphate
AFM	Atomic force microscope
ATP	Adenosine triphosphate
AV	Atrioventricular node
BPM	Beats per minute
CV	Coefficient of variation
DSP	Digital signal processing
ECG	Electrocardiogram
EEG	Electroencephalogram
EHT	Engineered heart tissue.
EIS	Electrochemical impedance spectroscopy
EMG	Electromyogram
ERP	Effective refractory period
FEM	Finite element method
hiPSC	Human induced pluripotent stem cell
HR	Heart rate
IIR	Infinite impulse response
LTI	Linear time invariant
MEA	Micro electrode array
MEMS	Micro electro mechanical system
PDMS	Polydimethylsiloxane
PEDOT:PSS	Poly(3,4-ethylenedioxythiophene) polystyrene sulfonate
PZT	Lead zirconate titanate
SA	Sinoatrial node
STED	Stimulated Emission Depletion
USB	Universal serial bus

ORIGINAL PUBLICATIONS

P1 J. Virtanen, S. Somppi, H. Törnqvist, V. Jeyhani, P. Fiedler, Y. Gizatdinova, P. Majaranta, H. Väätäjä, A. Valldeoriola-Cardó, J. Lekkala, S. Tuukkanen, O. Vainio, V. Surakka, and A. Vehkaoja, Evaluation of novel dry electrodes in canine heart rate monitoring, Sensors 18(6) (2018) 1757. Doi: 10.3390/s18061757.

P2 J. Virtanen, J. Leivo, A. Vehkaoja, S. Somppi, H. Törnqvist, P. Fiedler, H. Väätäjä, V. Surakka, Dry contact electrodes performance in canine ECG, Proceedings of ACI 2018 : Fifth International Conference on Animal-Computer Interaction (ACM), Atlanta, United States (2018). Doi: 10.1145/3295598.3295609.

P3 J. Virtanen, A. Pammo, A. Vehkaoja, S. Tuukkanen, Piezoelectric dual axis cantilever force measurement probe, IEEE Sensors (in press, 2019). Doi: 10.1109/JSEN.2019.2950765.

P4 J. Virtanen, M. Toivanen, T. Toimela, T. Heinonen, S. Tuukkanen, Direct measurement of contraction force in human cardiac tissue model using piezoelectric cantilever sensor technique, Current Applied Physics 20(1) (2020) 155-160, Doi: 10.1016/j.cap.2019.10.020.

Unpublished manuscript

M1 J. Virtanen, M. Koivisto, T. Toimela, A. Vehkaoja, T. Heinonen, S. Tuukkanen, Direct measurement of construction force in engineered heart tissue in 2D- plane using dual-axis cantilever sensor.

AUTHORS CONTRIBUTION

Publication 1 (P1)

In this publication the performance of three different dry electrocardiogram electrodes is studied. The author has designed and fabricated the metal electrodes, all electrode housings, conducted the data analysis on the measurement results, and written the article for the most parts. Patrique Fiedler has provided the polymer electrodes. Vala Jeyhani has designed and fabricated the electrocardiogram measurement device. Sanni Somppi has developed the testing scheme and Sanni Somppi and Heini Törnqvist have conducted the measurements.

Publication 2 (P2)

In this publication the performance of two different dry electrocardiogram electrodes further developed from electrodes presented in P1 is studied. The author has designed fabricated the metal electrodes all housings, conducted the data analysis on the measurement results and written the article for the most parts. Patrique Fiedler has provided the polymer electrode which was further tailored by the author. Joni Leivo has developed polystyrene sulfonate coating procedure for the metal electrodes. The application of the coating was carried out by him and the author. Vala Jeyhani has designed and fabricated the electrocardiogram measurement device. Sanni Somppi and Heini Törnqvist have conducted the measurements.

Publication 3 (P3)

This publication studies a dual axis piezoelectric cantilever sensor system with an embedded signal processing unit. The author has planned the calibration tests, developed and fabricated the all sensors, electronics and written the software. Calibration measurements have been carried out by Arno Pammo and the author. The author has also carried out the data analysis presented in the publication and written the article for the most parts.

Publication 4 (P4)

This publication studies *in vitro* cardiac construct contraction force measurement using and a single axis piezoelectric cantilever force sensor. The author has planned the calibration tests, and the *in vitro* force measurement scheme, developed and fabricated the sensor system and performed the data analysis. Maria Koivisto (née Toivanen) has cultured the cardiac constructs. Maria Koivisto (née Toivanen) and the author have carried out the measurement. The author has written the article for the most parts except the cardiac construct culturing part which has been written by Maria Koivisto (née Toivanen).

Manuscript 1 (Unpublished manuscript) (M1)

This publication studies *in vitro* cardiac construct contraction force measurement using a dual axis piezoelectric cantilever force sensor. The author has planned the calibration tests, and the *in vitro* force measurement scheme, has developed and fabricated the sensor system and performed the data analysis. Maria Koivisto has cultured cardiac constructs and developed the perforated silicone sheet culture procedure. Maria Koivisto and the author have carried out the measurements. The author and Maria Koivisto have written the article with equal contribution.

1 INTRODUCTION

The heart is an organ which produces periodically repetitive contractions and pumps blood into the vessels and blood circulation system. Cardiomyocytes and electrically conductive myocardial cells called Purkinje fibers form the muscular tissue of a heart. The contraction of the heart is governed by the individual cell action potential signals resulting in a synchronous contractile action in the cardiac tissue. The action potential of a cell is caused by the ion currents moving in and out of individual cardiac cells. The summarized ion current signal or action potential changes can be measured as an electrocardiogram (ECG) signal which represents a macroscopic view of the cell action potentials in the heart. (Klabunde 2011)

Cardiovascular diseases have been estimated to have caused 40% of the human deaths in Europe in 2017 (Timmis et al. 2017). The most common individual cardiovascular condition causing deaths is ischemic heart disease. It has been estimated that 20% of the mortality in Finland was caused by ischemic heart disease in 2017 (Official Statistics of Finland 2017). Electrical operation of the heart during cardiac cycle can be observed to reveal health information of a heart. This means measuring and monitoring heart functionality with, for example, ECG signal recording. ECG measurements have been known since the 1800s (do Vale Madeiro et al. 2018) and due to its importance, ECG is a very well understood biological signal. Electrocardiogram has traditionally been a gold standard in measuring the operation of the heart.

Growing awareness and interest in personal health has set a need for health monitoring not only for humans but also animals. Wearable electronics (Cima et al. 2014; Stoppa et al. 2014; Heo et al. 2018; Liu et al. 2017) is a discipline addressing this trend. Wearable electronics enable monitoring of biopotential signals such as ECG, electroencephalogram (EEG) and electromyogram (EMG) (Mukhopadhyay et al. 2014; Windmiller et al. 2013; Nag et al. 2017) and the measurements require electrodes. Biopotential measurements are commonly done using wet electrodes. Wet electrodes need electrically conductive gel to be applied between the electrode

and skin for proper and reliable operation (Wiese et al. 2004; Pani et al. 2015). The application of the electrically conductive gel should also be considered in everyday life or when performing long term cardiac and other biopotential measurements. Wet electrodes which are used in the animal ECG measurements may also require shaving of fur to provide reliable results (Brugarolas et al. 2014; 2015). Repetitive removal of fur is not convenient for the animal or the owner. A maintenance-free dry electrode system could provide a solution which allows constant and reliable monitoring of ECG over long periods of time.

Advances in stem cell tissue engineering has opened opportunities for using cardiac cell culture (Takahashi et al. 2007; Burridge et al. 2012; Mummery et al. 2002). Even though the cultured stem cell construct will not represent the organ, such as a heart, as a whole, the methodology opens an opportunity to study the cardiac cycle *in vitro*, in controlled environments (Mills et al. 2019). This has allowed new application possibilities in the fields of personalized medicine and drug development (Mannhardt et al. 2017; Sasaki et al. 2018). Some of the research in medicine development can be done using animals such as zebrafish (McGrath et al. 2008; Parng et al. 2002, 2005) or carrying out the testing with organs obtained from living animals (Olson et al. 2000). However, the animal models and methods using them have not been proven very accurate when studying the effects of drugs on humans (Heinonen 2015; Mills et al. 2019). Also growing ethical concerns toward animal testing (Combes et al. 2003; Ranganatha et al. 2012; Doke et al. 2015) motivates finding other testing approaches. Human induced pluripotent stem cells (hiPSC) may provide better accuracy in drug toxicity and drug efficacy testing (Braam et al. 2010; Hirt et al. 2015; Vuorenpää et al. 2014, 2017) and eliminate the need for animal testing. Moreover, the research of cardiac genetic diseases and their therapy may also benefit from possibilities stem cell culturing and engineering (Matsa et al. 2011, Moretti et al. 2013; Karakikes et al. 2015).

Cell action potential signals of a cardiac construct can be measured for example with a micro electrode array (MEA) (Li et al. 2016; Reppel et al. 2005; Caspi et al. 2009; Harris et al. 2013; Qu et al. 2015; Oyunbaatar et al. 2019). Also, fluorescence imaging with, for example, calcium ions can be used for action potential monitoring (Li et al. 2016; Lee et al. 2012; Lopez et al. 2014; Pointon et al. 2014; Feaster et al. 2015). With those methods, despite being able to reveal cardiac behavior such as beat rate and cell action potential it is not possible to monitor the contraction force of the cardiac construct. Contraction force measurement capability may allow new information for

the cardiac drug development (Mannhardt et al. 2017). Recently demonstrated methods for *in vitro* cardiac contraction force measurement require complex setup (Borin et al. 2018), engineered heart tissues (EHT) (Mannhardt et al. 2017) or cultivation on top of specialized substrates (Kim et al. 2017; Park et al. 2005; Rajan et al. 2018). A simple and reliable cardiac cell contraction force measurement setup which can be used in standard culture environments such as petri dishes or well plates could resolve some of the above-mentioned challenges.

In this work, two different proof of concept cardiac cycle topics were studied 1) canine ECG measurements using five different dry contact electrodes and 2) direct single and dual axis contraction force measurements of hiPSC originated cardiovascular constructs. The ECG electrode measurements were conducted in different postures aiming for everyday use of the system. The force measurement was carried out using piezoelectric cantilever sensors aiming for a use of inexpensive cell culture environments such as standardized petri dishes. Both of these cardiac cycle measurements possess different challenges but can however be approached using similar types of signal processing and analysis methods. A pattern matching signal processing methodology was used in analysis of the measurement data in both canine ECG and cardiac construct contraction force measurements.

This thesis work is structured such that the physiological ground of a human heart is described in the 'Background' chapter. The chapter contains an explanation of electrical activity of the heart and a basic principle of the myocardial cell contraction mechanism. Following that in the 'Previous research' chapter the current state of the relevant research in the thesis scope is reviewed. The aims of the thesis, which are further reflected in the 'Summary and conclusions' chapter, are presented next. The theory of the research methodology is explained in the 'Theory' chapter with the 'Materials and methods' chapter describing the practical the methodology used in the research work. Finally, the obtained results are presented in the 'Results and Discussion' chapter and the conclusions reflecting the aims, finalizing the thesis, are presented in the 'Summary and Conclusions' chapter.

2 BACKGROUND

2.1 Cell action potential and electrocardiogram

Electrocardiogram is a time domain biopotential signal revealing the spontaneous electrical activity of the heart. Biopotential here is understood as a sum of cell level action potential signals. Action potential signals are caused by the charges (ions) moving in and out of the cardiac cells during the cardiac cycle. Depending on the state, the cells exchange mainly calcium, sodium, potassium and chloride ions through ion pumps and ion channels in the cell membrane. This ion transfer process consumes energy which is produced inside the cells by mitochondria and transferred to the ion channels and pump with adenosine triphosphate (ATP). ATP is then consumed to adenosine diphosphate (ADP) releasing energy to enable the ion pumping. (Bronzino et al. 2014)

There are four main myocardial cell types in the heart participating in the governance of the cardiac contraction by the electrical stimulus. These are ordinary cardiomyocytes which can be beating or smooth cells, pacemaker cells, which are a special type of cardiomyocytes, and electrically conducting cells called Purkinje fibers. Each of these cell types have a different role in the making of the contraction cycle. Pacemaker cells are mainly responsible for producing the spontaneous repetitive beating stimulus which initiates the cardiac cycle. The fast acting (beating) cardiac muscle cells are responsible for the contraction relaxation work in the cardiac cycle. The smooth myocardial cells operate at a much slower pace. They regulate for example the shape and volume of the heart depending on the different operation conditions. The electrically conducting cardiomyocytes resemble nerve cells and do not contract but transmit the electrical stimulus in the heart tissue. They conduct the electrical signals approximately four times faster than the contracting cardiac muscle cells, which enables simultaneous contraction of different areas in the heart. (Klabunde 2011; Hamrell 2018)

Cardiac cells have two main potential states in their operation - polarized and depolarized. Polarized state means that the cells try to maintain a negatively charged

state towards the outside of the cell membrane. The polarized state is also called the resting phase. The resting potential is maintained by excess potassium ions inside the cardiac cell. The concentration gradient drives these ions outside of the cell, resulting in an action potential across the cell membrane. This potential difference can be measured and is approximately -90 mV. (Klabunde 2011; Hamrell 2018)

During the cardiac cycle there are five distinct phases in an action potential curve of a single beating cardiomyocyte. These and the respective ion currents are illustrated in Figure 1 where potassium, calcium and sodium ion currents are noted with g_{K+}, g_{Ca++} and g_{Na+} respectively. Cycle 0 starts from calcium stimulation outside the cell tubule receptors which open the ion channels in the cell membrane. This results in a rapid depolarization of the cardiac cell as the ion concentrations balance inside and outside of the cell membrane. In the depolarized state cells have a neutral charge relative to the outside of the cell and action potential over the cell membrane is then approximately 0 mV. Next in phase 1 an initial repolarization takes place as the sodium channels close and potassium concentration starts to slowly increase inside the cell. During phase 2 calcium is still flowing into the cell, partially canceling the effect of potassium influx, which causes the plateau in the action potential signal. Repolarization takes place during phase 3 when potassium influx continues and calcium flows outside of the cell. Finally, in phase 4 potassium concentration reaches the repolarization equilibrium. The period between phase 0 and phase 4 called effective refractory period (ERP), during which the cardiac cell contraction occurs. During depolarization the cardiac cell does not react to additional stimulation and maintains its low electrically conductive state. (Klabunde 2011; Barrett et al. 2010; Hamrell 2018)

The hearts of large mammals generally resemble each other very much, even though there are differences in the organs of different species. However, there are only small differences with a human heart and a dog heart. For example, a minor difference in the shape of the organ. The heart of a human and the heart of a dog are structurally and functionally very similar. (Hill et al. 2015)

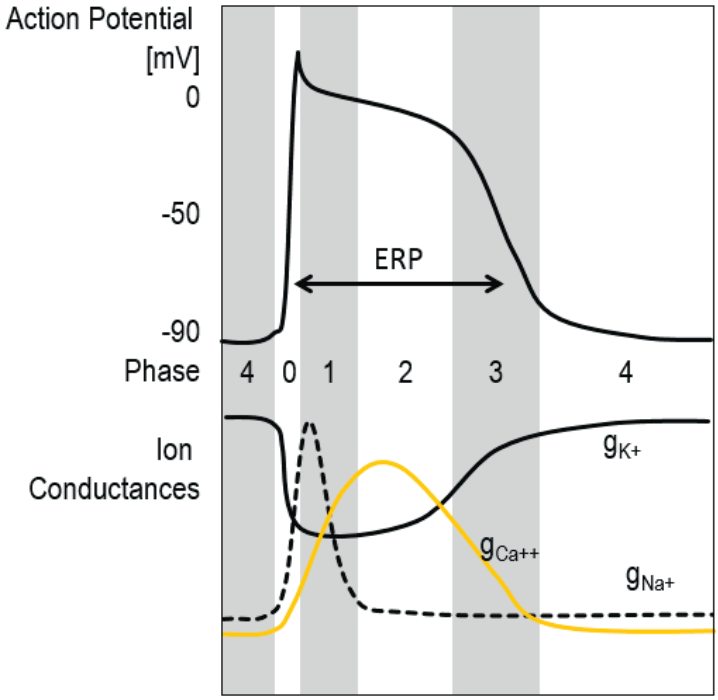

Figure 1. An action potential cycle of a single cardiomyocyte with corresponding potassium (g_{K+}), calcium (g_{Ca++}) and sodium (g_{Na+}) ion conductances.

Pacemaker cells generate the beating stimulus in the heart and can be found for example at sinoatrial node (SA node). The pacemaker cells have similar cycle behavior to the ordinary beating myocardial cells, with the exception that there is no definite resting potential in the cells. Therefore depolarization (phase 0) and repolarization (phase 3) characterize the pacemaker cell cycle. Figure 2 illustrates the pacemaker cell action potential curve behavior where potassium and calcium ion currents are noted with g_{K+} and g_{Ca++} respectively. In the pacemaker cells the ion currents are slower than with ordinary beating myocardial cells. The depolarization (phase 0) is mainly caused by slow influx of calcium ions, which is then followed by repolarization by influx of potassium ions (phase 3). During the resting phase the action potential slowly changes at approximately -50 mV. In pacemaker cells this repolarization-polarization cycle happens spontaneously, and they initiate the cardiac contraction and relaxation. The stimulus cycle then propagates along the cardiac tissue also with electrically conducting cells distributing the stimulus signal in the heart. (Klabunde 2011; Barrett et al. 2010)

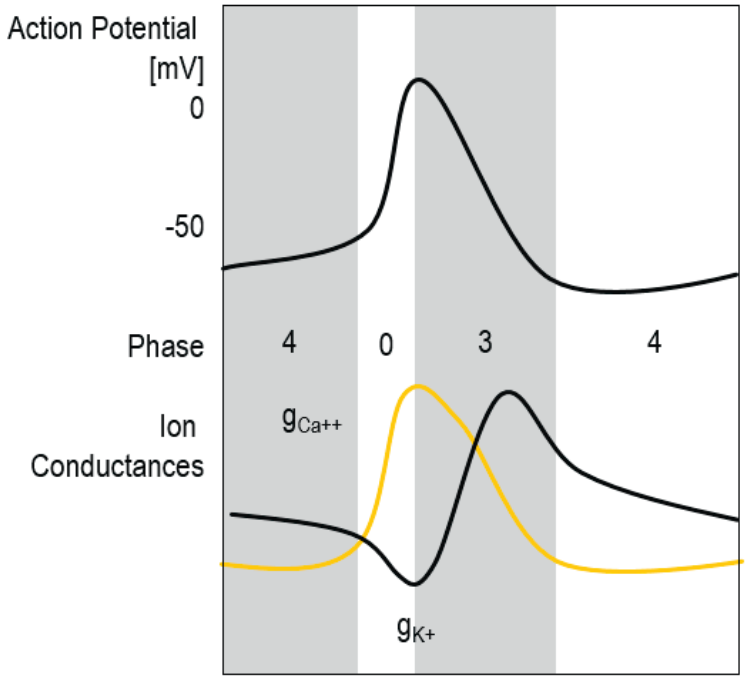

Figure 2. An action potential cycle of a pacemaker cell with corresponding potassium (g_{K+}) and calcium (g_{Ca++}) ion conductances.

Combined synchronous ion transfer currents of large number of myocardial cells result in an integral representation of the action potential signals which is then called a biopotential signal. In the case of a heart, this biopotential signal is called electrocardiogram. The action potential stimulation wave propagates in the different parts of the heart resulting in a macroscopic ECG signal which is illustrated in Figure 3. The cardiac contraction cycle is initiated by the pacemaker cells located in the SA node. There are also pacemaker cells at the atrioventricular node (AV node). The SA node is however the primary location stimulating the cardiac cycle. The AV node does not initiate the stimulus cycle unless the process has failed at the SA node. The electrical stimulus wave then propagates through the organ to complete an ECG cycle. The ECG signal is characterized with different phases denoted with letters P-U. The QRS- complex is located in the middle of the ECG curve. (Hamrell 2018; Barrett et al. 2010)

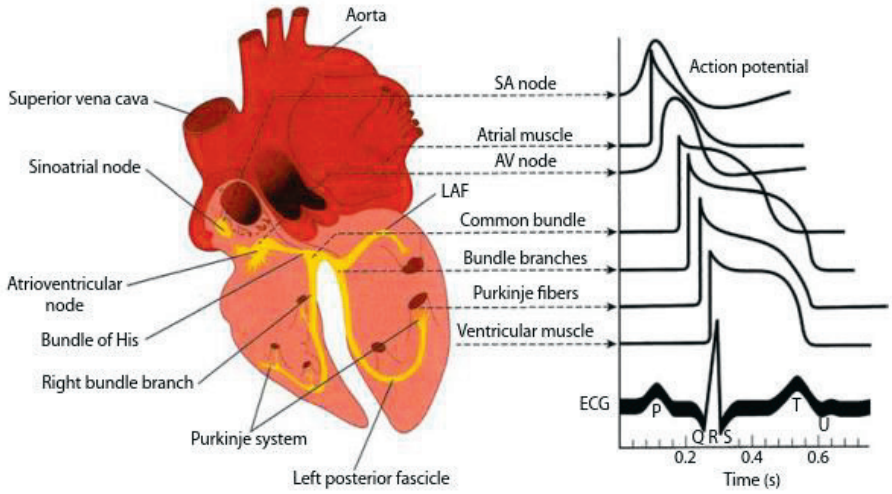

Figure 3. Main components of a heart with cell action potential signals forming an ECG signal (Barrett et al. 2010). (Reproduced with permission from McGraw Hill, Lange, USA)

2.2 Myocardial cell contraction and force generation

Cardiac cell contraction work happens with two proteins, actin and myosin, interacting inside a cardiomyocyte. The protein system also involves a third protein, titin, which connects the myosin filaments to the cell walls which are attached to the neighboring cardiomyocytes. The elastic properties of the titin affect the contraction system and titin also directs actin-myosin movement. During the contraction of the cardiomyocyte, actin and myosin filaments are able to slide relative to each other, shortening the length of a cardiac cell and thus performing contraction work. During the relaxation phase actin and myosin return to their expanded state. (Klabunde 2011)

Contraction and expansion of a cardiac cell both consume energy. During the cell contraction ATP, which has been bound to myosin, is releasing energy and becomes ADP. This released energy is then used for doing the contraction work by the cell. The contraction is initiated by an action potential signal from a neighboring cell and this signal is received by a tubule receptor of the cell. The receptor opens a calcium ion channel in the cell membrane and calcium is released outside the cell, which then causes the cell contraction process to take place. This contraction cycle is illustrated in Figure 4. (Klabunde 2011)

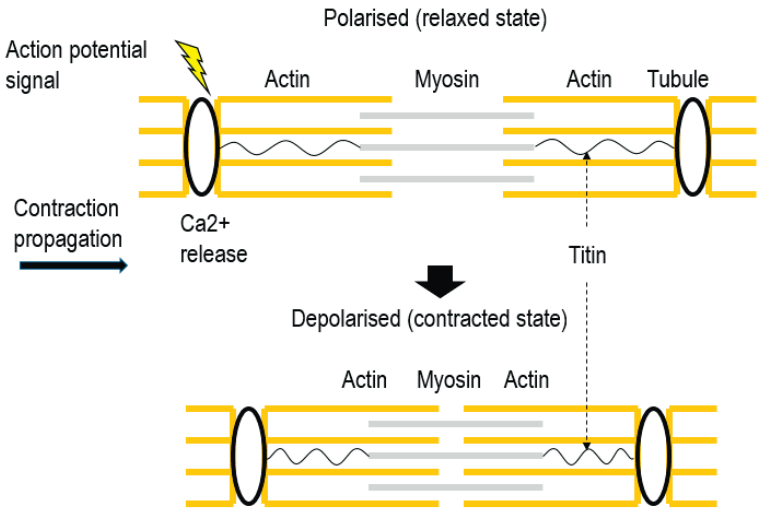

Figure 4. Cardiac cell contraction mechanism with actin, myosin and titin participating in the contraction process.

3 PREVIOUS RESEARCH

3.1 Dry electrodes in biopotential measurement

Dry electrodes are a class of biopotential electrodes which do not need electrically conductive gel or electrolyte to operate properly. Dry electrodes have been used in biopotential recordings with both humans and animals (Chi et al. 2010; Gargiulo et al. 2010). Dry electrodes can also be classified into dry contact, insulated or non-contact dry electrodes (Chi et al. 2010). The main difference in the operation principle between the dry contact and insulated or non-contact electrodes is the charge coupling mechanism between the skin and the electrode. In the contact electrode this coupling mechanism is dominantly resistive, while the other two have dominantly capacitive charge transfer.

In the biopotential measurements there are alternatives for the dry electrodes. The gold standard being a wet electrode, which has electrolyte between the skin contact and the electrode. Along with more traditional passive electrodes there has been efforts to use active electrodes. An active electrode has a biopotential amplifier in the electrode to improve the performance. (Di Flumeri et al. 2019)

Wearable electronics is an application area in which there is an interest of using dry biopotential electrodes. Different dry ECG contact electrode design concepts have been proposed for human use. For example, Chlaihawi et al. (2018) have reported embedding carbon nanotubes into the electrodes to enhance electrical conductivity and improve skin electrode contact. For the same purpose of fabricating an elastic and electrically conductive electrode, silver nanowires with polydimethylsiloxane (PDMS) matrix has been proposed by Myers et al. (2015). These silver nanowire electrodes have shown very similar performance compared with the electrodes from Chlaihawi et al. (2018), especially when high enough contact pressure (1.72 psi) was used. As with the carbon nanotube electrodes above, the data recorded using the silver nanowire electrodes showed a good correlation with wet reference electrode waveforms.

Dry biopotential electrodes can be fabricated with three-dimensional printing techniques. Salvo et al. (2012) have proposed a 3d- printed resin electrode which is plated with titanium and gold layers after the printing process. The gold-titanium interface reduces the risk of skin irritation. The Ag/AgCl reference electrode and this 3d- printed electrode had a very similar performance.

Instead of polymer matrix also fabric can be used as a structural element in dry ECG electrodes (Paradiso et al. 2015; Beckmann et al. 2010; Puurtinen et al. 2006). Despite similar designs, the method to fabricate the actual conductive part of the electrode varies. Paradiso et al. (2015) studied a knitted conductor design with stainless steel wires knitted into the fabric. The proposed electrodes showed a good waveform match with reference electrodes. A QRS- complex failure rate of 1.85% during 1570 observed heartbeats was reported. Beckmann et al. (2010) have studied both knitted and woven dry electrode materials. With the various approaches studied, the skin electrode contact impedance remained low enough to enable reliable biopotential signal recording.

Compared to wet electrodes, all of the dry electrode types are likely to have higher skin contact impedance which leads to higher susceptibility to noise and interference. Despite the somewhat unfavorable measurement conditions of the dry electrodes in terms of noise, the advances in the electronics and signal processing have made it possible to reliable record biopotential signals with dry electrodes (Gargiulo et al. 2010).

3.2 Dry Canine Electrocardiogram electrode

Traditionally, canine ECG measurement has been done by using wet electrodes and a Holter type ECG recording device (Hill 1968). Alternatively, "alligator clips" have been used in clinical environments especially during anesthesia (Brugarolas et al. 2015). Wet ECG electrodes require shaving with furry animals and application of electrically conductive gel to operate reliably. The "alligator clips" may be more practical not having to have the conductive gel but may become painful for the animal during the measurement. In contrast to the wet ECG electrodes, dry electrodes have been used without shaving or application of conductive gel. This approach has enabled acceptable results in canine ECG measurement. (Brugarolas et al. 2015)

Previously there has not been extensive research on the application of dry electrodes in canine ECG measurements. Brugarolas et al. (2014; 2015) have been studying this subject using gold, stainless steel and PEDOT:PSS coated metal pin electrodes. In these studies, the pin count of these tested electrodes has varied between one and ten. The electrodes were characterized using Ag/AgCl reference electrode in a buffered saline solution. Also, a skin-electrode impedance model was presented and the model characterization was done using electrochemical impedance spectroscopy (EIS). The dry electrode impedances reported by Brugarolas et al. (2015) were rather high from approximately 300 kΩ to 1 MΩ. The PEDOT:PSS coating on the electrode reduced the skin electrode contact impedance approximately by a factor of 3.

Brugarolas et al. (2015) present little results on *in vivo* performance of these electrodes and only the 6- pin gold electrode was evaluated in comparison to a Holter device. The effect of posture or activity (lying and walking) on the QRS- complex detection was studied, and more dynamic walking had larger QRS- complex detection deviation when compared to the Holter device measurement results. (Brugarolas et al. 2015)

3.3 Myocardial cell contraction force measurement

Previously, cardiac cell and construct contraction force has been measured with various approaches such as PDMS cantilever (Kim et al. 2008; You et al. 2014), PDMS pillars (Tanaka et al. 2006), SU-8 cantilever (Kim et al. 2016), flexible sheet (Shimizu et al. 2010; Sasaki et. 2018) or Atomic force microscope (AFM) (Qu et al 2019; Borin et al. 2018). The peak contraction force has been reported to vary in the range from nano newtons (Rodriguez et al. 2014) to over a hundred micro newtons (Mannhardt et al. 2016) up to one milli newton (Sasaki et al. 2018). Cardiac cell contraction force has also been measured from various biological entities such as neonatal cardiac rat cells (Linder et al. 2010; Kim, Dong-Su et al. 2017; Birla et al. 2005), embryonic cardiomyocytes (Eschenhagen et al. 1997) or hiPSC originated cell cultures such as cardiac constructs (Rodriquez et al. 2014; Pesl et al. 2016).

The contraction force measurement principles can be categorized into direct or indirect measurements. In the direct force measurement systems, the force sensor outputs a signal that is proportional to the applied force. This can be a mechanical

system such as cantilever (Borin et al. 2018; Vyas et al. 2017) or a flexible sheet (Linder et al. 2010; Kim et al. 2017). Indirect measurement principle means that the contraction force is estimated using an imaging system. Known mechanical properties such as Young's modulus of the cultivation substrate (Tanaka et al. 2006) or a cantilever (Balaban et al. 2001) allow a computation of the contraction force. Passive carbon fiber cantilever (Sugiura et al. 2006; Myachina et al. 2018) or an embedded magnetic bead matrix (Yin et al. 2005) have also been used in combination with video imaging to measure the contraction force. The displacement resolution of the optical measurement is limited by diffraction of light to approximately 0.5 μm.

It is possible to have a below diffraction limit resolution with high resolution microscopy. For example, Stimulated Emission Depletion (STED) microscopy is one possible alternative. However, STED requires a fluorescent staining of the observed elements and a high intensity laser light exposure, which may induce phototoxicity effects to the studied samples. (Niewhuizen et al. 2013) With this regard, especially when the measurement system is aimed to be used in the drug toxicity evaluation, these methods were not considered applicable.

3.3.1 Atomic force microscopy

Atomic force microscopy is a form of a cantilever force measurement. A cantilever is on the other end attached to a fixed point and the tip at the other end is in contact with contracting cells or tissue. Depending on the spring constant of the cantilever, the applied force creates a displacement change at the cantilever tip. AFM has been used to measure the cardiac cell contraction force (Borin et al. 2018; Vyas et al. 2017; Chang et al. 2013). With AFM it is possible to achieve measurement resolution down to the nano newton range (Borin et al. 2018), while the higher limit reported has been up to a micro newton range (Vyas et al. 2017). This sensitivity range makes it possible to observe forces caused by a single beating cardiac cell or larger populations such as cardiac constructs.

3.3.2 Polymer cantilevers

Cantilevers for force measurement can also be prepared from polymers such as PDMS (Park et al. 2005; Kim et al. 2017). Park et al. (2005) have fabricated a PDMS cantilever array for observing contraction forces. This cantilever structure is

essentially passive and acts only as a cultivation substrate. The method requires image processing capability to be able to measure contraction forces. Kim et al. (2017) have demonstrated a PDMS cantilever structure with a piezoresistive sensor element. Contrary to the passive PDMS cantilever sensor this approach does not need video imaging for the force measurement. Both of these methods are capable of very low contraction force measurements.

3.3.3 Carbon fiber based measurement systems

A passive carbon fiber cantilever can be attached to a cell. This creates a mechanical system where the carbon fiber is physically bent by the force exerted by a contracting cell. The displacement is then optically measured by using a microscope and digital imaging (Sugiura et al. 2006; Myachina et al. 2018). The measurement scheme allows contractile force measurement below one micronewton. Myachina et al. noted that the carbon fiber attachment to the cell membrane may cause it to slide along the membrane and thus distort the measurement results. A cantilever normally imposes a limitation of applying a predefined load to the measured subject. Therefore, the measurement results may be induced by the cantilever itself. Sidorov et al. (2017) developed a system where varying load can be applied to an EHT. Cardiac constructs are grown between fixed pillars and the variable load is achieved by moving carbon fiber cantilevers, which are in contact with the EHT and moved in respect of the EHT. Video imaging is then used to obtain the displacement of the loading carbon fibers (Sidorov et al. 2017). This measurement principle is illustrated in Figure 5.

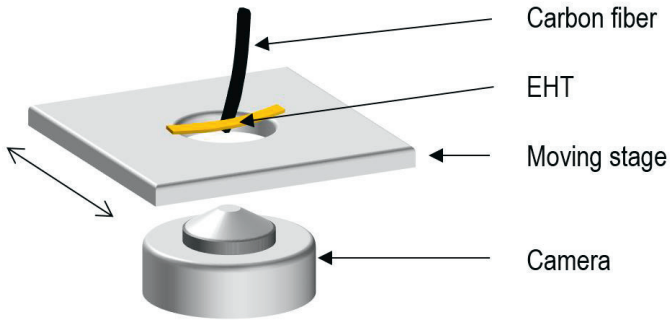

Figure 5. An illustration of a contraction force measurement principle using moving stage, carbon fiber cantilever and a camera (Sidorov et al. 2017).

3.3.4 Cell drum

Linder et al. have proposed a use of a membrane ('Cell Drum') for contraction force measurement. Cells are cultured on a collagen monolayer on top of a 10 micrometer thick PDMS membrane which is loaded with gas pressure. Cardiac contraction modulates the chamber pressure, which can be varied, and the displacement of the membrane can then be measured with a laser beam deflection. Known mechanical properties of the membrane are then used to obtain the contraction force from the displacement information. (Linder et al. 2010). The 'Cell Drum' system is illustrated in Figure 6.

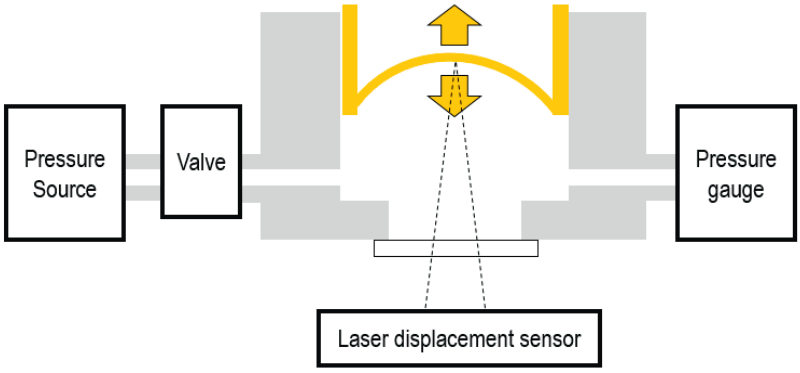

Figure 6. 'Cell Drum' cardiac contraction force measurement system (Linder et al. 2010).

3.3.5 Flexible sheet

Flexible sheets with cells cultured on them have been proposed for contraction force measurement by Sasaki et al. (2018) and Shimizu et al. (2010). A culturing substrate sheet is prepared from a biocompatible material such as collagen or fibrin. Cell populations are cultured on the sheet and once the beating and contraction of the cardiac tissue structure is detected the force measurement is carried out with a load cell or other force measurement device. The measured forces recorded by Sasaki et al. (2018) were in the range of 1 millinewton.

3.3.6 Magnetic bead

Magnetic beads in combination with video microscope have been proposed for cardiac cell contraction force measurement (Yin et al. 2005). Yin et al. have demonstrated a measurement concept which is capable of measuring contraction forces from piconewtons to micronewtons. In this method magnetic beads are attached to the cells and the beads are then applied to different magnetic forces creating a variable load for the cells. The displacement of the beads is recorded with a microscope and video imaging device. Yin et al. (2005) recorded contraction forces of a single cardiomyocyte in the order of micronewtons with displacement of few micrometers.

3.3.7 Summary of the contraction force measurement methods

The myocardial cell contracting forces can be measured with different methodologies. Each of these methods have a different nature and thus there may be a different application area for each of these methods. The summary of the methods discussed above in addition to their advantages and weaknesses is listed in Table 1.

Table 1. Summary of the myocardial cell contraction force methods.

Principle	Force range	Advantages of the measurement principle	Weakness of the measurement principle
AFM	10 pN - 10 μN	High force measurement resolution	Only small displacement measurements are possible. Difficult setup.
Polymer cantilever	Down to 1 nN	Very low spring constant is possible	Specialized cell culture environment is required, passive cantilever needs imaging solution
Cell Drum	Down to 1 μN	Load adjustment is possible	Specialized cell culture environment is needed.
Flexible sheet	Up to 1 mN	High force generation is possible	Specialized cell culture environment is needed.
Magnetic bead	1 pN - 1 μN	High resolution, possibility to adjust load	Magnetic beads have to be attached to cells, imaging equipment needed.
Carbon fiber	Below 1 uN	Load adjustment is possible	Imaging equipment is needed. EHT:s are necessary

4 AIMS OF THE THESIS

The detailed aims of the work are divided into two categories, where the first is dealing with dry canine ECG electrodes and their performance and the second with the *in vitro* cardiac construct contraction force measurements. In the first category, the aims were to design, fabricate, and to evaluate the performance of five different dry ECG electrodes and specifically study:

1) The effect of different electrode designs and electrode materials on the coverage ratio of QRS- complex detection from canine ECG signal.

2) The effect of posture and activity, i.e. standing, sitting, lying or walking, on the QRS- complex detection from the measured ECG signal.

Regarding the cardiac construct contraction force measurements, the aims were to:

3) Develop and fabricate a cost-efficient micronewton range force measurement system for cardiac construct contraction force measurement.

4) Carry out *in vitro* contraction force measurements with this developed force measurement system in order to validate measurement concept.

5) Study the differences of single and dual axis *in vitro* cardiac construct contraction force measurements.

5 THEORY

5.1 ECG measurement and its challenges

ECG measurement is subjected to noise and interference due to various reasons. Mainly these are electromagnetic interference and movement-based artefacts. Electromagnetic interference components may contain noise such as powerline interference and signal from other electromagnetic sources (Limaye et al. 2016). In addition, there may be unwanted biopotential signals such as EMG caused by muscular activity in the body (Haritha et al. 2016). These interference components are difficult to avoid due to the ECG measurement principle. The electromagnetic noise can couple capacitively, inductively and resistively to the ECG signal. An ECG measurement setup naturally forms an induction loop, and capacitive noise coupling happens with the body of the measurement subject. The properties of the electrode skin interface affect the induced noise and it is beneficial to try to minimize the skin - electrode contact impedance in the measurement setup. (Khandpur 2005)

The capacitive coupling of powerline interference to an ECG measurement is illustrated in Figure 7 where the measurement leads are marked with RA (right arm), LA (left arm) and LL (left leg). The 50 Hz power line interference current is denoted with I_n and couples to the body through capacitances C_n and C_g via a floating ground plane. The inductive noise is coupled via mutual inductance L_n. (Kaniusas 2019)

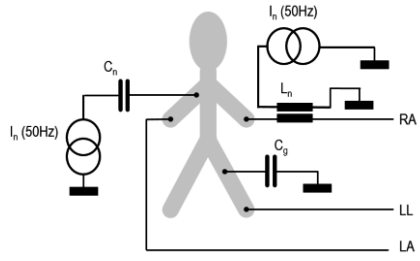

Figure 7. Common mode powerline interference coupling into an ECG measurement with interference coupling capacitance C_n, floating ground coupling capacitance C_g.and a mutual inductance L_n. Measurement electrode are marked with RA (right arm), LA (left arm) and LL (left leg).

Muscular activity near the electrodes also induces motion artefact disturbance to the measured signals due to stretching of the skin (Ottenbacher et al. 2009; Muhlsteff et al. 2004). These unwanted signals are mainly caused by the change of electrical properties in the skin electrode contact and therefore creation of a modulating error signal to the ECG measurement. As with the electromagnetically coupled interference, the amplitude of the noise amplitude may be much larger than the measured ECG signal itself, which will set requirements to the measurement electronics and post processing of the measured signals.

5.2 Location of the ECG electrodes

The shape of the ECG signal is affected by the location of the measurement electrodes. As the ECG is a macroscopic view of the summarized cell action potentials this can be understood by observing ECG on a projection plane (here on the frontal plane). This concept is illustrated in Figure 8 where the Einthoven triangle for humans is defined by electrodes RA (right arm), LA (left arm) and LL (left leg). Bipolar ECG leads I, II and III are then formed, measuring the respective potential differences between the electrodes. These ECG leads are superimposed on the heart to form electrical reference axes of the heart as shown on the right in Figure 8. Each of the leads I, II and III signals provide different information on the heart functionality, thus having different ECG curve shapes. (Klabunde 2011)

Due to different physiology of animals the measurement configuration and the location of the electrodes may be different. Therefore, it is necessary to carefully define the electrode locations during the EGC measurement for repeatable and comparable measurement results.

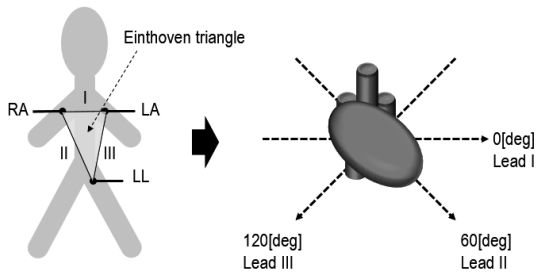

Figure 8. Einthoven triangle and the corresponding electrical axes of the heart.

5.3 Biopotential electrode equivalent circuit

Biopotential electrodes can be electrically modeled to represent the electrical properties of skin, electrode and the skin electrode interface. The different layers of the skin may be modeled with resistances, capacitances and current sources (Chi et al. 2010).

The dry biopotential electrode model in canine environment can be simplified from a wet electrode model, as there is no electrolyte component in the skin electrode interface. The equivalent circuit model therefore has only three main components: a resistance representing the body, cabling and connections and a resistive and capacitive component in parallel at the skin electrode interface (Brugarolas et al. 2015; Chlaihawi et al. 2018; Chi et al. 2010). The dry electrode model is illustrated in Figure 9, where R_{ct} and C_{el} represent the electrode skin interface and R_{el} represents the resistance of the rest of the measurement system including body, cabling and connections.

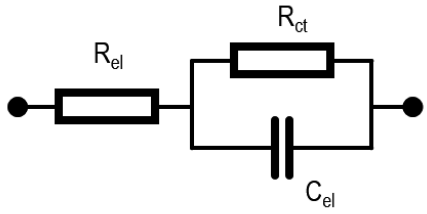

Figure 9. Dry biopotential electrode equivalent circuit for canine ECG measurement. R_{ct} and C_{el} represent the electrode skin interface and R_{el} represents the resistance of the rest of the measurement system (Brugarolas et al. 2015).

5.4 Low force measurement

A cantilever can be used to measure force and displacement (Duc et al. 2006; Su et al. 2004; Ziegler et al. 2004). The cantilever force measurement principle is based on linear elastic properties of the cantilever material. A cantilever can be characterized with a cantilever spring constant. The displacement of the cantilever tip is linearly proportional to the applied force as long as there is no plastic deformation in the cantilever.

A cantilever beam which is fixed at one end and force applied to the other end is illustrated in Figure 10. Parameters defining the behavior of this cantilever are shown in Equations (1a) and (1b). The dimensions of the cantilever are defined by its length L, width b, and height h. The spring constant K (Equation (1a)) is, in addition to the dimensions, dependent on the Young's modulus E of the cantilever material and the moment of inertia I (Equation (1a)). The shorter the cantilever beam and the larger the cross section with a constant length of a cantilever, the higher the spring constant K of the cantilever will become, therefore making the cantilever stiffer. (Rao 1995)

As a mechanical system, a cantilever has a natural frequency ω_0. This is defined by L, b, h, E and the mass of the cantilever m as shown in Equation (1b). The natural frequency of the cantilever becomes higher, the smaller mass and the stiffer the cantilever beam is. (Rao 1995)

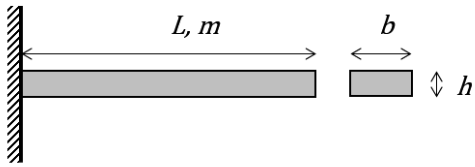

Figure 10. A Cantilever beam which is fixed from the other end.

$$K = \frac{3EI}{L^3}, \qquad I = \frac{bh^3}{12} \tag{1a}$$

$$\omega_0 = (1.875)^2 \sqrt{\frac{EI}{mL^4}} \tag{1b}$$

The presented linear elastic cantilever model characterizes the cantilever behavior only in one dimension. For example, the torsional effects or the elongation of the cantilever are not included in this model.

5.4.1 Piezoelectric principle

Low forces can be measured exploiting various physical principles such as piezoresistivity, piezoelectricity or capacitance (Wei et al. 2015; Ştefănescu et al.

2013). A piezoelectric sensor is suitable for low force measurement due to its high sensitivity and large dynamic range (Liang et al. 2014; Gautschi 2002).

Piezoelectricity is a physical phenomenon where a charge distribution in a material changes as a response to an applied mechanical stress. The change in the charge distribution then results in a potential difference across the material, depending on the material properties. A converse piezoelectric effect also exists in piezoelectric materials. This means that an electric field causes stress and strain in piezoelectric material, changing the shape of the material. These phenomena make piezoelectric materials suitable for different kinds of sensing applications such as force, displacement and acceleration sensing. (Gautschi 2002)

The piezoelectric phenomenon exists in materials that have polar molecule structure. This can happen in natural crystals such as quartz or in the materials where the polar molecules are randomly oriented. Random molecular orientation in the material is not desirable in a piezoelectric sensor operation. To achieve more uniform orientation in the piezoelectric material the molecules can be poled. In the poling process the molecule orientation is adjusted with an electric field and usually the poled material is also heated above the Curie point during the poling. This process results in a piezoelectric material which still retains a molecule orientation after the poling electric field is removed. Poled material is better suitable for sensing applications such as force measurement. The poling process is illustrated in Figure 11 where (a) material is randomly oriented, (b) being poled and (c) after poling.

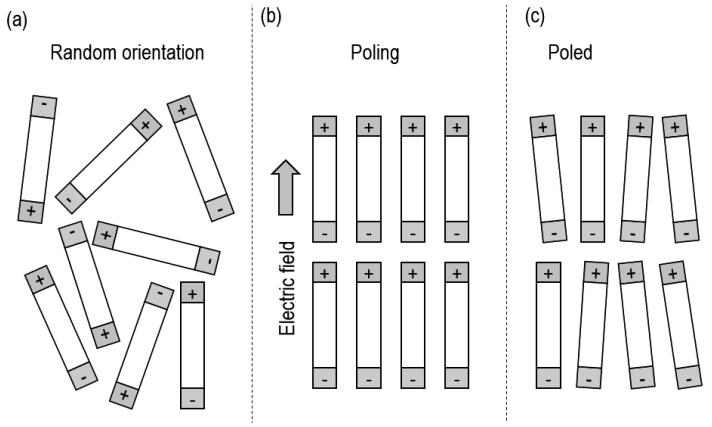

Figure 11. Piezoelectric dipole molecules in (a) random (b) being poled and (c) poled orientation.

5.4.1.1 Piezoelectric properties

Piezoelectric material behavior can be modeled with two characteristic matrices for direct and converse piezoelectric behavior. These characterize how the piezoelectric material behaves in different mechanical stress conditions and electric fields. The parameters define the piezoelectric coefficients and the dielectricity in three dimensions. The applied stress in this representation is characterized as direct stress and shear stress components. The output voltage of the piezoelectric sensor is defined by the applied stress and dielectric properties of the material. It is common to express this in terms of piezoelectric gauge factor, where the sensor output is normalized by capacitance such that piezo crystal has characteristic capacitance and capacitance/charge ratio. (Gautschi 2002)

The tensor matrix for a converse piezoelectric effect of a polarized material is shown in Equation (2a), while the direct piezoelectric effect is shown in the same notation in Equation (2b). $\boldsymbol{S}$, $\boldsymbol{T}$ and $\boldsymbol{E}$ denote the strain, stress and electric field vectors respectively, while $\boldsymbol{s^E}$ and $\boldsymbol{d}$ denote the tensor matrices with elastic constants, piezoelectric constants respectively and $\boldsymbol{\epsilon^T}$ denotes the dielectric constants. In matrix notation (2c) a characteristic matrix of piezoelectric effect is presented for a polarized lead zirconate titanate (PZT) material. This is in de Voigt notation such that the first three coefficients are associated with direct stress while the latter are for shear stress in three cartesian dimensions. In these representations the stress components and the electrical components are given separately. Certain components of the matrix become zero due to the polarization, which ideally makes the material transversely isotropic. (Gautschi 2002; Yang 2005)

$$\boldsymbol{S} = \boldsymbol{s^E T} + \boldsymbol{d^T E} \tag{2a}$$

$$\boldsymbol{D} = \boldsymbol{d\,T} + \boldsymbol{\epsilon^T E} \tag{2b}$$

$$\begin{bmatrix} D_1 \\ D_2 \\ D_3 \end{bmatrix} = \begin{bmatrix} 0 & 0 & 0 & 0 & d_{15} & 0 \\ 0 & 0 & 0 & d_{15} & 0 & 0 \\ d_{31} & d_{32} & d_{33} & 0 & 0 & 0 \end{bmatrix} \begin{bmatrix} T_1 \\ T_2 \\ T_3 \\ T_4 \\ T_5 \\ T_6 \end{bmatrix} + \begin{bmatrix} \epsilon_{11} & 0 & 0 \\ 0 & \epsilon_{22} & 0 \\ 0 & 0 & \epsilon_{33} \end{bmatrix} \begin{bmatrix} E_1 \\ E_2 \\ E_3 \end{bmatrix} \tag{2c}$$

Practical piezoelectric sensor materials can be crystalline but also polymeric or sintered such as PZT. Depending on the fabrication methods of the sensor material, the properties of it may become anisotropic. If this is desirable to some extent these

effects can also be achieved during the poling of the material. The sintering process also naturally results in porosity and anisotropic behavior. Porosity also affects the linear elastic properties of the piezoelectric material. (Li et al. 2003; Kar-Gupta et al. 2006; Dunn et al. 1993)

5.4.1.2 Electrical model of a piezoelectric sensor

Piezoelectric sensor is a dynamic sensor which means that it cannot measure stationary properties reliably. This is due to the non-ideal electrical properties of the materials and sensor interfaces which leak charge, resulting in a sensor output becoming zero in time. Thus, truly static phenomenon cannot be measured with a piezoelectric sensor. However, in many cases the sensor properties can be made 'pseudo static' which means that the time constant during which the sensor charge leaks away is large enough. The piezoelectric sensor has a high pass behavior in the measurement system. (Gautschi 2002)

A piezoelectric force sensor equivalent circuit can be modeled with a current generator where a mechanical stress creates charge with a relationship to the displacement and with a parallel capacitance representing the dielectric component. This is illustrated in Figure 12, where the piezoelectric current generator is in parallel with the capacitive component of the sensor C_s, the capacitance of the cable C_c and the load resistance of the measurement system R_l. Together these form a total load of Z as shown in Equation (3) at the input of a measurement device. (Bentley 2005)

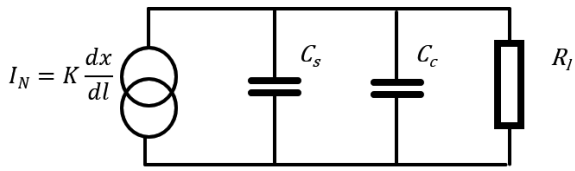

Figure 12. Electromechanical equivalent circuit model of a piezoelectric sensor (Bentley 2005).

$$Z = \frac{R_l}{1+R_l(C_s+C_c)s} \qquad (3)$$

5.4.2 Multi Axis force measurement

In the multi axis force measurement several sensor elements are needed, depending on the degrees of freedom to be measured. A dual axis sensor can be designed with two sensor elements. However due to fabrication challenges posed by a two-element sensor (Liang et al. 2014) it may be beneficial to use planar sensor structures such as micro electromechanical system (MEMS) (Enikov et al. 2000). For example, a planar four element sensor is capable of sensing force in three dimensions (Kristiansen et al. 2008). This concept is illustrated in Figure 13. There both tensile and compressive stresses are present simultaneously on the sensor with the loading F to the x- axis direction. Due to the symmetrical design, the operation is the same also to the y- axis direction, which in this case is perpendicular to the x- and z- axes. Despite the more complex mechanical construction of a multi axis sensor, it is also characterized by the spring constant, mass and properties of the piezoelectric material (Tibrewala et al. 2009).

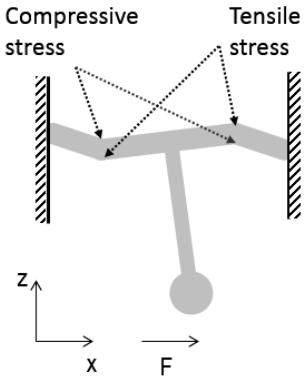

Figure 13. Schematic side view of a multi axis force measurement probe with compressive and tensile stress areas identified with arrows.

5.4.3 Digital signal processing

Digital signal processing (DSP) is a methodology where discrete time or frequency domain signals are processed in numerical format. In particular, DSP is convenient with linear time invariant (LTI) systems. Contrary to the analog signal processing digital signal processing methods require analog signal digitization to have it in a usable format. The digitization is done with analog to digital conversion (ADC) of

the desired analog signal. The conversion is limited by a sampling frequency which limits the maximum bandwidth of the unaliased sampled signal to a half of the sampling frequency. The differences between continuous analog and discrete digital signals and their filtering are illustrated in Figure 14(a) where a continuous analog signal and a corresponding analog filter is shown and in Figure 14(b) with a digital signal and the applied filtering (Buck et al. 1998).

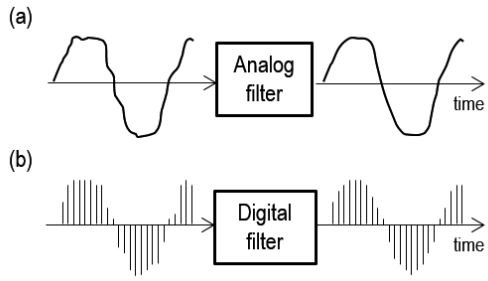

Figure 14. Illustration of (a) an analog and (b) a digital filter operation.

5.4.4 Infinite impulse response signal processing

Infinite impulse response (IIR) system is a digital signal processing system which has a feedback loop resulting in the filter response becoming infinite (Buck et al. 1998). IIR filter is characterized by the Equation (4), where $h(k)$, a_k and b_k are the impulse response of the filter, feedback loop and forward loop coefficients, respectively, while the $x(n)$ and $y(n)$ are the input and output sequence of the signals, respectively (Ifeachor et al. 2002).

$$y(n) = \sum_{k=0}^{\infty} h(k)x(n-k) = \sum_{k=1}^{N} a_k x(n-k) - \sum_{k=1}^{M} b_k y(n-k) \qquad (4)$$

An IIR filter operation is illustrated in Figure 15. The forward branch ($H_a(n)$) and the feedback branch ($H_b(n)$) combine the input signal $x(n)$ and the feedback signal and processes it to an output signal $y(n)$ (Buck et al. 1998).

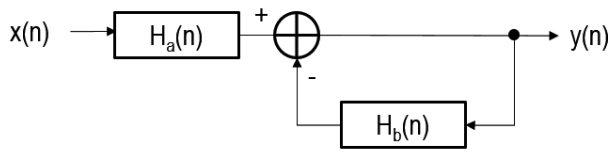

Figure 15. IIR filter system schematic drawing with forward ($H_a(n)$) and feedback ($H_b(n)$) branches (Buck et al. 1998).

6 MATERIALS AND METHODS

6.1 Dry Canine ECG electrodes

Five different dry ECG electrodes were fabricated, and their performance was studied in terms of a coverage ratio. The coverage ratio is defined here as a ratio of successfully recovered ECG cycles divided by the total measurement duration. This results in a normalized number of the electrode performance which was later used in the electrode analysis. A coverage ratio of 1 represents a situation where all cycles during the measurement are successfully detected while coverage ratio of 0 represents a situation where no cycles have been detected. The ECG signal was captured and stored with Spiritcore9D (Jeyhani 2017) measurement device and transferred to a personal computer for further analysis. Out of the five different electrode types three were spring loaded metal electrodes and two polymeric electrodes with Ag/AgCl coating on their surface. These are shown in Figure 16 where there is (a) 37- pin spring loaded nickel plated metal electrode, (b) 12- pin gold plated metal electrode, (c) 30- pin polymeric electrode, (d) 12- pin gold plated metal electrode with polystyrene sulfonate doped polymer blend (PEDOT:PSS) coating and (e) 12- pin polymeric electrode.

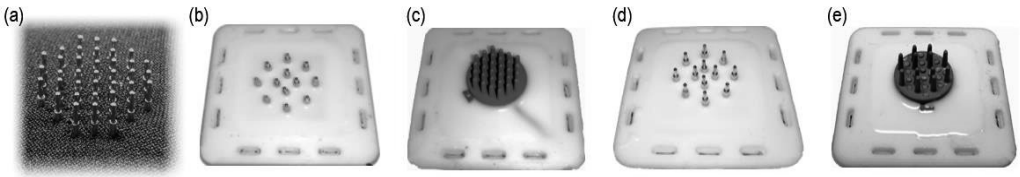

Figure 16. The evaluated dry ECG electrodes. (a) 37- pin electrode, (b) 12- pin gold plated electrode, (c) 30- pin polymeric electrode, (d) 12- pin electrode with PEDOT coating, (e) 12- pin polymeric electrode.

6.1.1 Testing procedure of the canine ECG measurement

Before the ECG measurement the electrodes were attached to a harness which was then dressed on a dog. This setup is illustrated in Figure 17, where electrodes were located on the side of the dog torso inside the harness and are marked with yellow circles.

Figure 17. The ECG measurement harness dressed on a dog with electrode locations marked with yellow circles.

The ECG measurement was carried out with the procedure consisting of three different measurement sessions. Before each session the measurement harness was dressed on the dog and it was removed after the session. During a single session a sequence of 1 min stand - 1 min sit - 1 min lie 1 min walk was repeated three times. The testing procedure is illustrated in Figure 18. The testing was carried out with three different dogs with each electrode resulting in 540 minutes of test data.

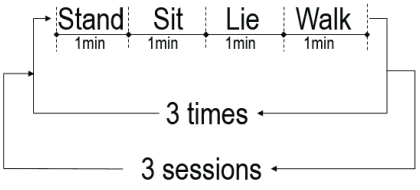

Figure 18. The Canine ECG electrode testing procedure.

6.1.2 R- peak detection and coverage ratio

In order to improve the raw ECG signal quality, it was pre-processed on a personal computer. The ECG signal was first filtered with a bandpass filter having corner frequencies of 2 and 30 Hz. These corner frequencies were selected to retain the approximately 100 ms long QRS- complex information and on the other hand minimize the baseline wander effect in the signal. A 50 Hz notch filter was also applied to remove unwanted powerline interference noise.

This filtered signal was further used to detect QRS- complexes. This detection was done by applying a pattern matching method which compares a predefined template and the measured signal. The pattern matcher methodology is also proposed to be used to detect the abnormalities. The exact criteria for the similarity are difficult to define as it connected to the phenomena to be studied. However, the pattern matcher can be set to detect and classify either normal or abnormal cycles, but it requires a cardio physiology expertise to define the required template shape to be matched.

High enough similarity between the template and the signal shape marks that a QRS-complex is found. In this process a normalized template window is moved over the observed data, which is normalized to local maxima found at the window equaling the length of the template. The distance between the template and the observed signal is then obtained by summing the squared difference at each point of the template length. When the distance is below a predefined threshold level, a QRS-complex detection is triggered. The ECG signal varies with respect to the electrode location and therefore the template was heuristically selected in each case to represent the typical ECG pattern with that measurement case. The block diagram of the applied signal processing chain is illustrated in Figure 19.

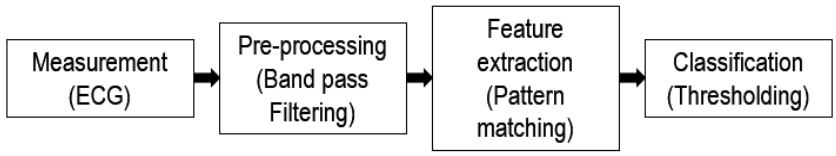

Figure 19. A block chain of the canine ECG signal conditioning and QRS- complex pattern matching.

An example of the template pattern which was used in the analysis is shown in Figure 20. The length of the pattern was chosen to be 0.25 s and it has a normalized amplitude where the local maxima peak amplitude is normalized to the value of 1.

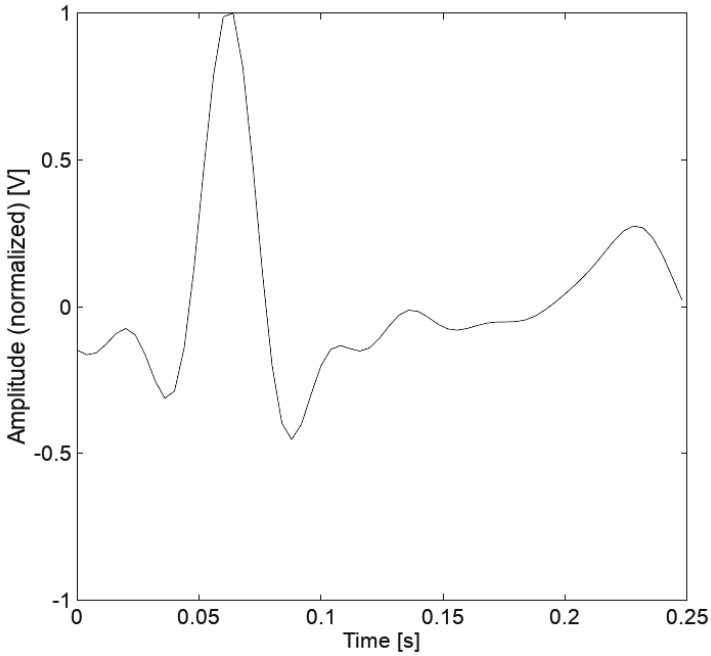

Figure 20. ECG pattern matcher template example for the canine QRS- complex detection.

The pattern matching methodology was also applied to the cardiac construct force measurement results. The focus was to classify the data enabling detection of anomalies for further analysis. The classification in this respect is beneficial when considering analysis of large amounts of measured data. The pattern matching method was improved when compared to the canine ECG QRS- complex detection. A template generation mechanism was added to initiate the method. The template in the force measurement analysis was obtained by first observing a particularly successful data set and computing a median curve from it. This median curve was then used as a template for the pattern matcher. For the decision making the threshold level was then set to a level where all the cardiac cycles of this particularly successful data set would be considered to be matching the template. A normalized template which was used in the cardiac construct contraction force measurement analysis is shown in Figure 21.

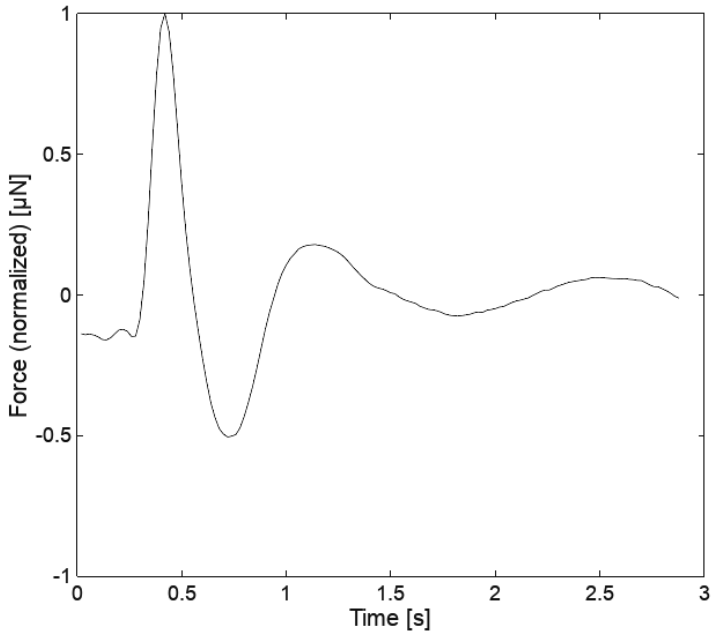

Figure 21. A median template for the *in vitro* contraction force measurement pattern matcher obtained from a particularly successful data set.

6.2 Cardiac cell contraction force measurement

6.2.1 Single axis piezoelectric cantilever sensor

A finite element method (FEM) simulation of the cantilever behavior was conducted to find the spring constant, piezoelectric behavior and the natural frequency of the proposed cantilever force sensor. The simulation was carried out by using a COMSOL Multiphysics (Comsol AB, Stockholm, Sweden) simulator on a personal computer. Both linear elastic and piezoelectric models were used in combination. Mechanical properties and the sensitivity computations were carried out in a stationary linear elastic piezoelectric simulation assuming zero charge leakage in the piezoelectric material. The natural frequency simulation was carried out using a harmonic load and performing the simulation in different frequencies. Later the simulation results were validated by actual measurements. The simulation results are

illustrated in Figure 22, panel (a) showing cantilever displacement at 200 μN load and panel (b) electric potential in the sensor element with the same load.

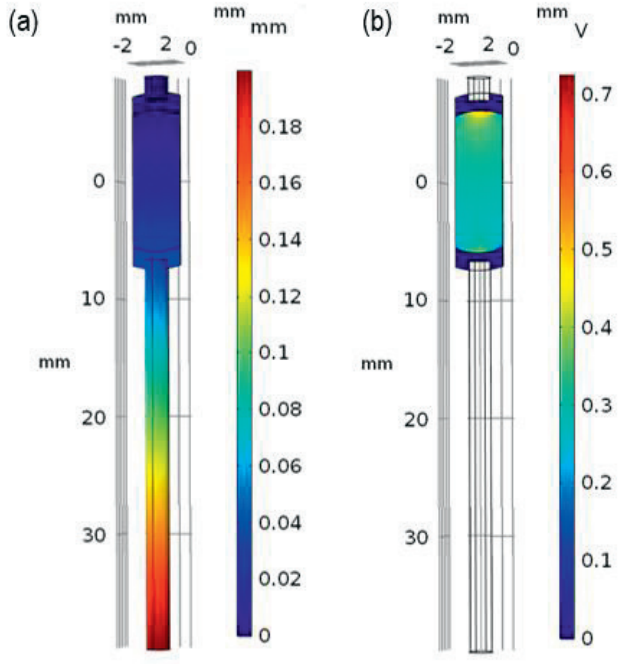

Figure 22. FEM simulation results of the single axis sensor (a) the displacement and (b) the electric potential.

6.2.2 Dual axis force sensor

The first version of the dual axis force sensor design was carried out with the same procedure as with the single axis sensor. Therefore, COMSOL was used to compute the spring constant and piezoelectric behavior of the dual axis sensor. The sensor construction is illustrated in Figure 23, where four sensor elements are shown and are numbered E1, E2, E3 and E4. The force sensing probe is pointing backwards in the figure. A prototype multi axis sensor was constructed and the simulation results were validated by calibration measurements.

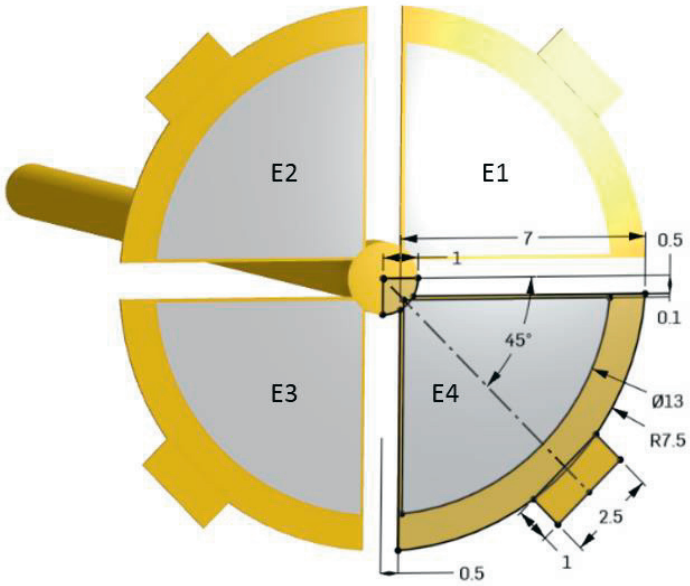

Figure 23. A schematic drawing of the first version of the dual axis force sensor (from publication P3).

In this sensor configuration the x- and y- axis force components are formed as a linear combination of the sensor element outputs as shown in Equations (5a) and (5b). U_x and U_y represent the x- and y- axis voltage signals respectively and $U_1 - U_4$ represent the individual sensor element output voltages.

$$U_x = U_1 + U_2 - U_3 - U_4 \qquad (5a)$$

$$U_y = U_1 - U_2 - U_3 + U_4 \qquad (5b)$$

6.2.3 L- shaped dual axis force sensor

An L- shaped version of the dual axis force sensor was designed to better suit the cardiac construct measurement setup. This was also a less rigid sensor with lower spring constant than the first version of the dual axis sensor, thus enabling larger displacement in the measurement with a similar loading. The operation of the sensor was simulated with COMSOL as with the previous versions of the force measurement sensors. The simulation results are presented in Figure 24 with (a) the

displacement and (b) the electric potential with 100 μN load applied to both x- and y- directions.

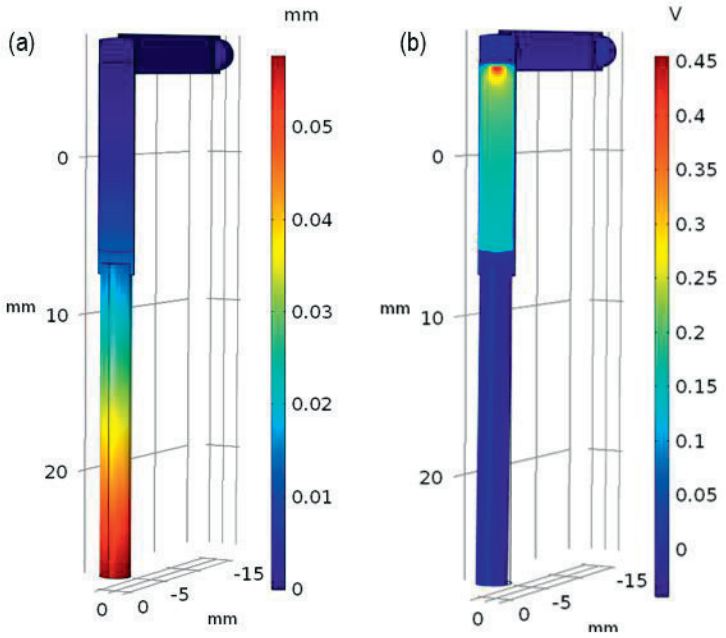

Figure 24. The L- shaped xy cardiac construct contraction force measurement probe. Panel (a) shows displacement and panel (b) electric potential with 100 μN load in both x- and y- directions.

6.2.4 Microscope setup

The *in vitro* cardiac construct contraction force measurements were performed under an optical microscope. In order to minimize the interference in the measurement results the setup was located on a stone table, which reduced the effect of conducted vibrations to the system. Furthermore, the setup was placed into a Faraday cage to minimize electromagnetic interference. The Faraday cage also functioned as a blocking structure for surrounding air flow which was detected to cause low frequency interference to the measurement results. The measurement setup with the microscope, stone table and the Faraday cage is shown in Figure 25.

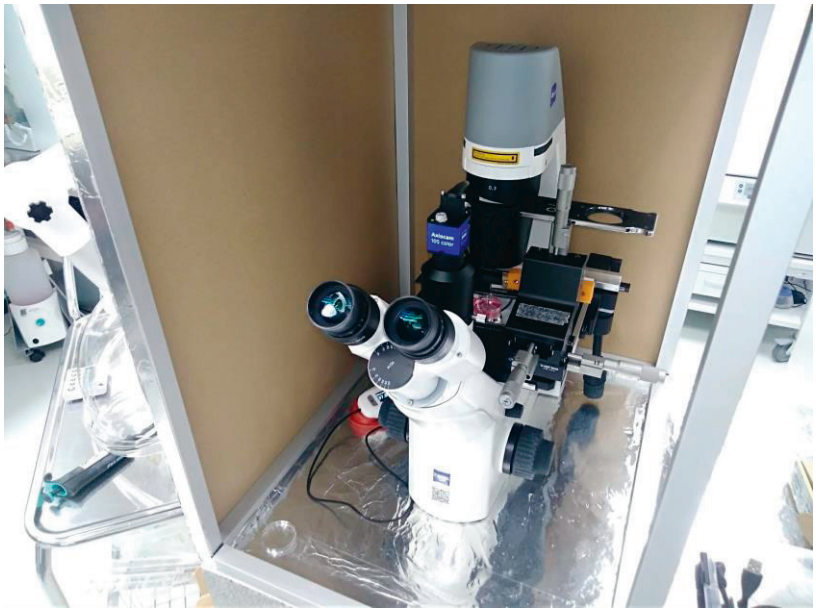

Figure 25. Cardiac construct contraction force measurement setup with the microscope, stone table and the Faraday cage (from M1).

The cardiac constructs in a petri dish were placed on a heated plate under the microscope and the force measurement probe was attached to them by using a micromanipulator. The measurement setup is illustrated in Figures 26(a) with single axis force measurement probe and (b) with a dual axis force measurement probe.

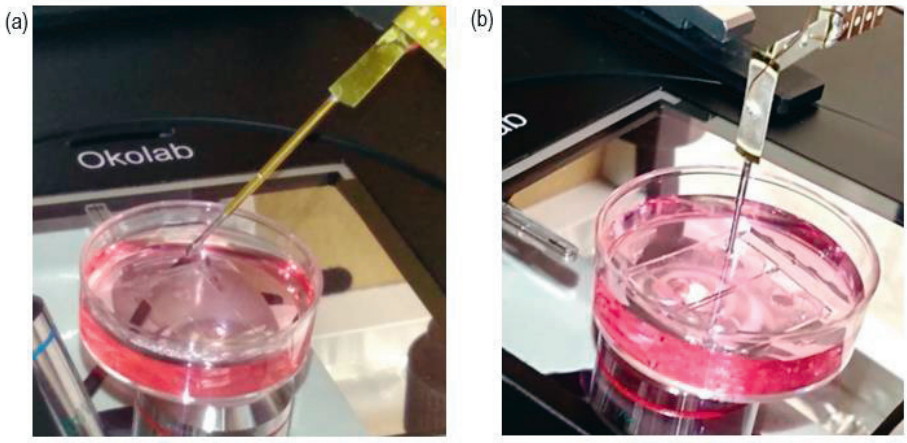

Figure 26. Force measurement setup and the probe location (a) single axis measurement probe (b) dual axis measurement probe (from M1).

6.2.5 Hardware and Software used in this work

A voltage amplifier was used to buffer the piezoelectric sensor element. The amplifier had a 50 MΩ input resistance and the sensor element capacitance was approximately 10 nF. The buffering amplifier design is described in more detail in publication P3.

The single axis and the first dual axis measurements were carried out using Arduino Due (www.arduino.cc) embedded hardware. Arduino Due was selected for this because it has higher computing capacity and more peripheral circuitry than Arduino Uno (www.arduino.cc). Arduino Due also has a native universal serial bus (USB) port which enables faster data transmission between the Arduino Due and a personal computer. The embedded hardware was changed to Teensy 3.6 (PJRC.COM LLC., Sherwood, USA) for the L- shaped dual axis sensor to achieve better ADC resolution. Teensy 3.6 board is very similar in functionality to the Arduino Due except that it has higher clock frequency and 16- bit ADC. In Figure 27 the block diagram of the measurement system is shown.

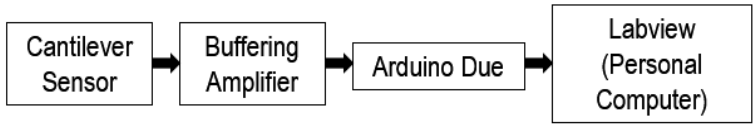

Figure 27. Measurement system block diagram.

To improve the force measurement signal quality, an IIR digital filter consisting of a bandpass and a 50 Hz notch filter was implemented on each sensor channel. The computing was done on the embedded hardware using floating point arithmetic. In the embedded processing the measured signal was further down sampled to 50 Hz in order to reduce the data flow between the measurement hardware and the personal computer. The amplitude and phase response of the digital filter used in the processing are shown in Figure 28. The frequency range of the measurement system combining the sensor, amplifier and the embedded digital filtering was approximately 0.5 to 10 Hz. The digital filter implementation is described in more detail in publication P3.

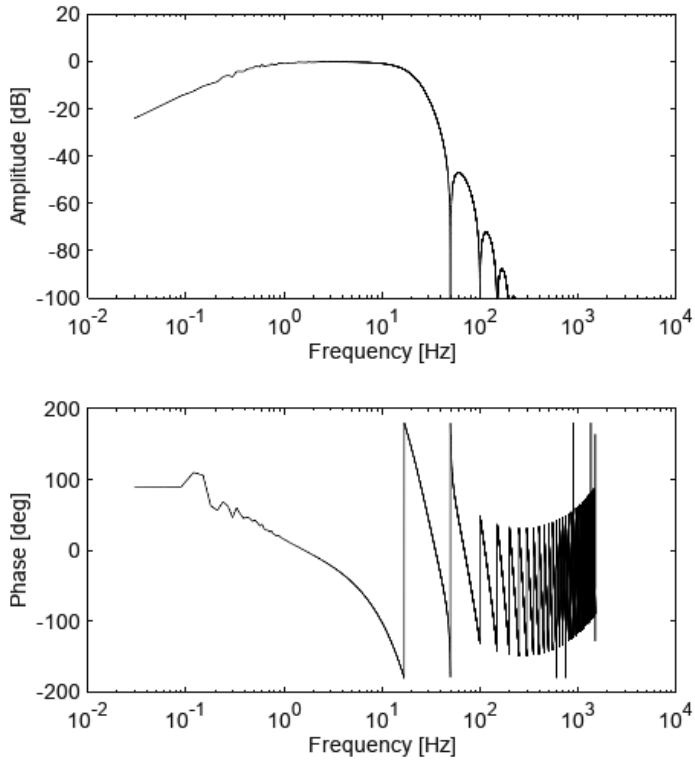

Figure 28. Frequency and phase response of the IIR filter implementation on the Arduino hardware.

6.2.6 Post processing of the measurement data

The post processing of all the measurement data in this work was carried out using Octave (GNU Octave, John W. Eaton,David Bateman, Søren Hauberg and Rik Wehbring). Octave is a computing package similar to MATLAB (The MathWorks, Inc., Natick, USA) to perform scientific and engineering computing on a personal computer or larger computer systems. The post processing included the QRS-complex detection in the canine ECG measurements. In the force measurements, force calibration results and *in vitro* contraction force measurements were post processed, including beat detection and cardiac cycle pattern matching analysis.

6.2.7 Piezoelectric force measurement sensors

The piezoelectric sensor elements were fabricated by hand. In short, first a commercial PZT piezo disc was cut to a desired shape and the parts were then soldered together to form a complete sensor. The fabricated sensors are shown in Figures 29. Panel (a) shows a single axis sensor, (b) first version of the dual axis sensor and (c) - (d) the L- shaped dual axis sensor with a side and front view respectively. The fabrication procedure is explained in more detail in (Virtanen et al. 2018) and in publications P3, P4 and M1.

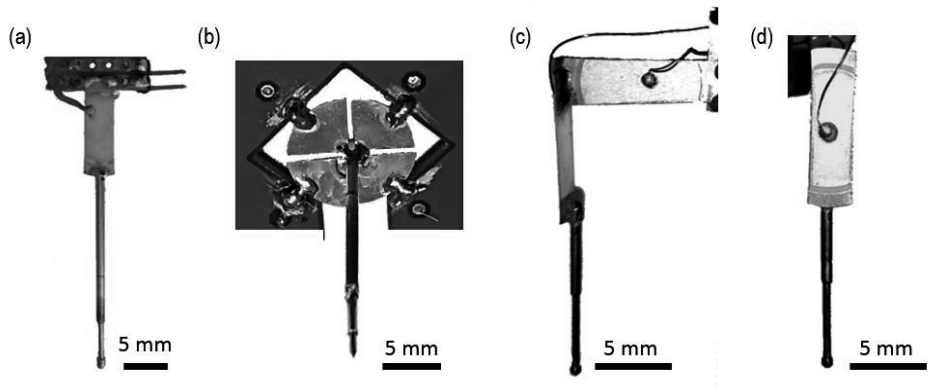

Figure 29. Force measurement sensor probes (a) the single axis sensor (b) the first version of the dual axis sensor probe (c) - (d) the L- shaped dual axis sensor side and front view respectively.

6.2.8 Sensor calibration method

The sensitivity calibration for the cantilever sensors was carried out using Stable Micro Systems TA.XTPlus texture analyzer (Stable Micro Systems Ltd, Surrey, United Kingdom). The calibration was done by applying a 1 Hz sine wave excitation with 200 μm amplitude to the cantilever tip. The sensor output and the texture analyzer force signal were measured with this excitation and the calibration was computed according to this data. This calibration method and data analysis are described in more detail in (Virtanen et al. 2018) and in publications P3, P4 and M1.

6.2.9 Software development tools

The embedded software was developed using Arduino development tools. The embedded software combined sampling of the signal, the proposed time domain IIR filtering and the communication to Labview software, which was running on a personal computer. The Labview interface was then used to record and store the data and provide a user interface to the measurement system.

6.2.10 Cardiac construct interfaces for the force measurement probe

Cardiac construct clusters were partially separated from the culture substrate prior to the force measurements. This was done to enable the cardiac construct to exert more force on the probe tip rather than on the culturing substrate. There were two different procedures to do the separation. In both cases the cardiac construct culturing was done using perforated PDMS sheets. The hole diameter in those PDMS sheets was approximately 5 mm in the first separation and 3 mm in the second separation. The thickness of the PDMS sheet was approximately 1 mm in both cases. The measurement with the first version separation method was carried out in a non-buffered medium without a heating plate under the microscope and the force measurement data was recorded for 10 s. The stability of the measurement setup in overall was not good in the first *in vitro* contraction force measurement trials and therefore the recording time was limited to 10s. However, this was considered appropriate as this was a proof of a principle of the cantilever measurement concept. The measurements using the second separation method had a heating plate, buffered culture medium and the measurements were carried out for 60 s.

In the first version of the separation the cardiac construct was detached from the culture substrate at the boundary of the construct. The center of the cardiac construct remained attached to the substrate at the bottom of the petri dish. The measurement probe tip was then attached to the detached parts of the cardiac construct. This separation method was used only with the single axis measurement probe. A non-scale schematic drawing of the measurement setup with the first version cardiac constructs separation method is illustrated in Figure 30.

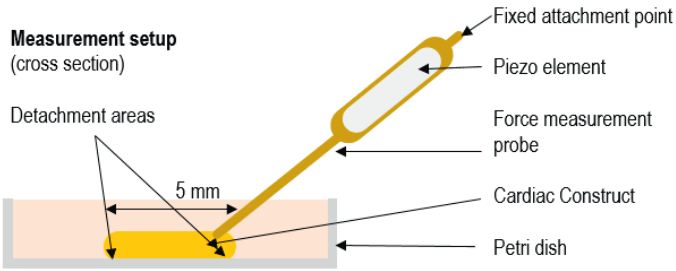

Figure 30. First version of the cardiac construct separation with the single axis force measurement probe tip located at the edge of the cardiac construct.

In the second version separation method the cardiac construct edges remained attached to the walls of the PDMS sheet hole. Contrary to the first version separation method, the cardiac construct was detached from the center from the culturing substrate. The separated construct in a PDMS sheet was then placed on another PDMS sheet with slightly larger holes to allow the cardiac construct contract as freely as possible. This separation method was used with both single axis probe and L-shaped dual axis probe measurements and is described in more detail in publication M1. A non-scale schematic drawing of the measurement setup with the L- shaped force measurement probe setup is illustrated in Figure 31(a) while the microscope image of the L- shaped probe tip placed onto a cardiac construct is shown in Figure 31(b).

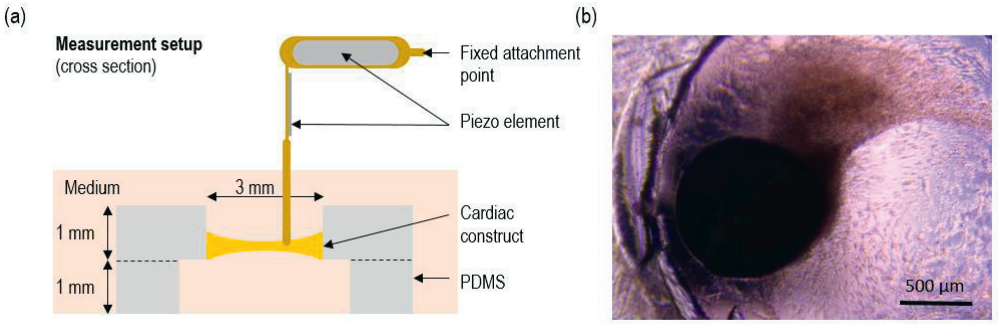

Figure 31. The measurement setup of the second version construct separation method with the L-shaped dual axis measurement probe. (a) a non- scale schematic drawing of the probe - construct location (b) microscope image of the probe tip at the construct (from M1).

7 RESULTS AND DISCUSSION

7.1 Dry canine ECG electrodes

The coverage ratio data was analyzed in 1 min sequences such that each test case (for example nickel plated electrode, standing posture) had 27 1-minute data samples. Due to the relatively small amount of the measurement data, these results are more indicative than conclusive. The average coverage ratios with all electrodes and all postures varied between 0.41 and 0.95. The highest average coverage ratio of 0.95 was achieved with the gold-plated electrode in a sitting posture while the smallest average coverage ratio of 0.41 was with the 12- pin polymeric electrode during walking. The summarized data of each electrode test cases is presented in Figure 32. There boxplots represent the 27 sample group values and the dashed lines represent the average values computed from the measured 1-minute samples.

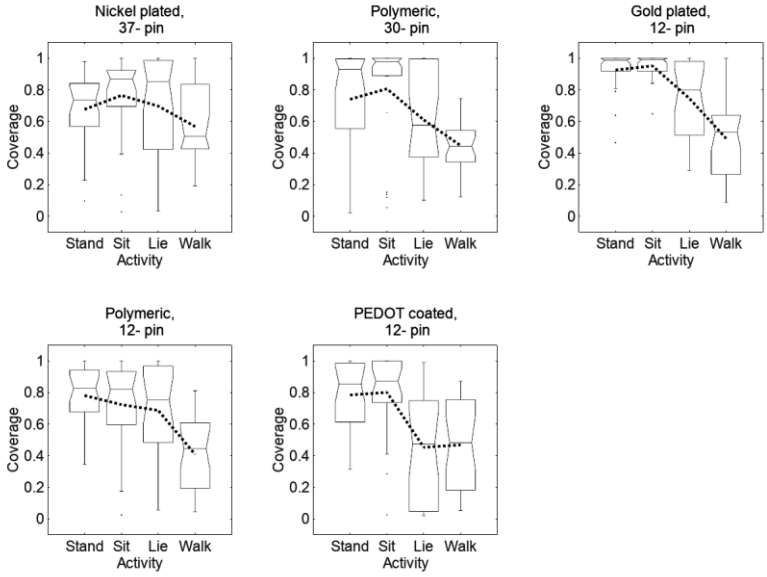

Figure 32. Tested dry electrode coverage ratio performance in the canine ECG measurements in different configurations. Average coverage ratios in each case are denoted with a dashed line.

The results show that the electrodes have different coverage ratios in different activity modes. Over 90% average ECG coverage ratio value is achievable in favorable measurement cases. The gold-plated electrodes in standing and sitting postures yielded the highest coverage ratio results with almost a 100% median coverage ratio. Except for the two favorable measurement cases with the gold plated electrodes, the material or the design of the electrodes does not appear to have large impact on electrode performance. The results are similar to those obtained previously by Brugarolas et al. (2015).

The results also show a trend where the measured coverage ratios fall during walking. This is visible with all electrodes and the trend can be seen in the average coverage ratio values. This can be explained with the presence of motion artifacts, which are more intense during walking than in a stationary posture such as standing. Another observation is that the variation of the coverage ratio is high in the lying posture with all electrodes. Since the lying posture is relatively stationary, this effect is likely not to be caused by the motion artefacts. When a dog is lying, the shape of its torso changes. Depending on the electrode location on the dog's body, this shape change may have caused a weak or complete loss of the skin electrode contact. This results in a ECG signal disruption and leads to low in the coverage ratio value.

To improve the electrode performance, the design of the electrode should have more adaptability to the motion and torso shape changes. Therefore, larger mechanical movement than of a few millimeters, as was achievable with the tested electrodes, would be desirable. Larger electrode contact area improving the probability of having sufficient electrical contact could also enhance the electrode performance. Other than the electrodes, the harness i.e. its design and the location of the electrodes may have an impact on the results.

7.2 Contraction force measurements

The force measurement system capability for the cardiac construct contraction force measurement was evaluated with calibration measurements and *in vitro* conditions. The calibration measurements consisted of a sensitivity measurement and an impulse response measurement which was used to obtain the frequency response of the measurement system. With two of the three fabricated sensors designs, the single

axis and the L- shaped dual axis force measurement probe, measurements were also carried out *in vitro* with cardiac cell constructs.

7.2.1 Sensitivity and frequency response

The sensitivities and the spring constants of the measurement probes varied due to different mechanical probe designs. The sensitivity of the single axis probe was 1.97 kV/N and the spring constant 0.78 N/m. Due to the symmetrical design of the first version dual axis probe, the sensitivity and the spring constant were approximately the same within the calibration measurement accuracy in x- and y- directions and were 0.93 kV/N and 209 N/m respectively. For the L- shaped dual axis probe the sensitivity and the spring constants were different in x- and y- axis. The measured sensitivity was 0.86 kV/N and 0.46 kV/N in x- and y- axis, respectively, and the spring constants 8.8 N/m and 4.3 N/m respectively. The coefficient of variation (CV) of the calibration sensitivity measurements were 1.4%, 2.9%, 0.5% and 0.6% for the single axis, dual axis and L- shaped dual axis probe in x- and y- directions respectively. These values are listed in Table 2.

Table 2. Force measurement system calibration results of the different measurement probe configurations.

Sensor	Sensitivity [kV/N]	Spring constant [N/m]	CV calibration [%]
Single axis	1.97	0.78	1.4
Dual axis (x- and y- axis)	0.93	209	2.9
L- shaped dual axis	0.86 (x- axis) 0.46 (y- axis)	8.8 (x- axis) 4.3 (y- axis)	0.5% (x- axis) 0.6% (y- axis)

Spectrum analysis was carried out to an *in vitro* measurement signal sampled at 6 kHz sampling rate and with the bandwidth of the measurement system of 250 Hz. Significant signal energy was not observed above 5 Hz. The lower frequency limit was set according to the beat rate which is assumed to be over 30 BPM. Therefore, the acceptable frequency range for the measurement systems was approximately from 0.5 Hz to 10 Hz. This was considered suitable for the *in vitro* cardiac construct contraction force measurements. The frequency response of the measurement system was obtained by computing a Fourier transform from the impulse response measurement data which satisfied the above mentioned criteria.

7.2.2 In vitro contraction force measurement results

In vitro peak contraction force and the beat rate obtained by the single axis probe and the first version of the separation method measurements were approximately 6 μN and 48 BPM respectively. A typical 10 s force curve is shown in Figure 33(a). The corresponding peak contraction force and beat rate of this measurement are shown in Figures 33(b) and (c), respectively. Further measurement data analysis was not carried out for these data, as this was a proof of concept experiment regarding the measurement principle. However, the beating of the construct and the movement of the measurement probe tip was visually inspected and confirmed from a video recording which is in supplementary material in publication P4.

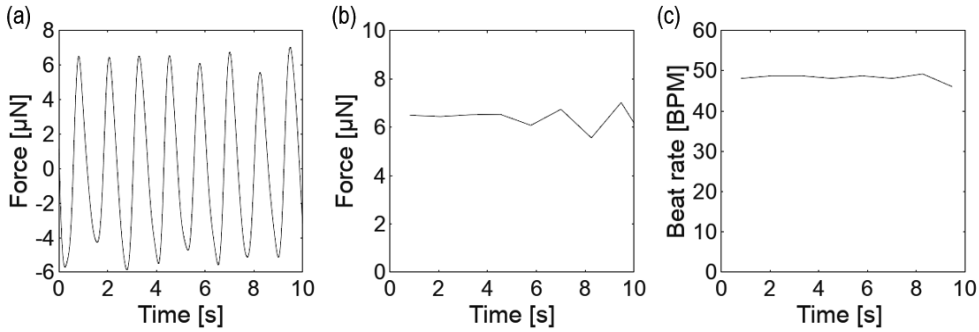

Figure 33. Single axis *in vitro* force measurement results with the first version separation method (a) the contraction force curve (b) the maximum cycle contraction force (c) beats per minute observed.

The single axis cantilever probe measurements were also carried out *in vitro* with the second version separation method. This measurement was repeated four times for a 60 s period. The peak contraction force varied between 3.4 and 6.7 μN, the standard deviation between 0.13 and 0.22 μN. In these measurements the coefficient of variation was between 3.3 and 4.1%. Due to the dynamic working principle of the piezoelectric sensor and the filtering of the measured signal, the bias level in the force measurement is approximately zero. Therefore, the force readings can also have negative values. A typical waveform shape, peak contraction force and beat rate of the single axis force measurement with the second version of the cardiac construct separation method is presented in Figures 34(a) - (c) respectively.

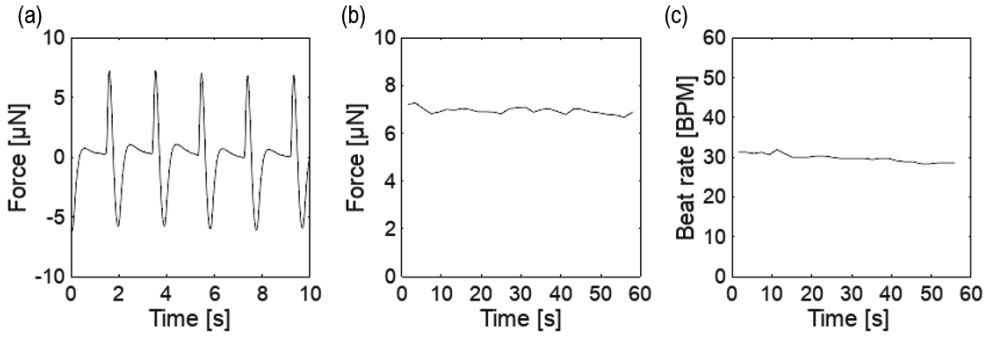

Figure 34. Single axis *in vitro* contraction force measurement results with the second version separation method (a) the contraction force curve (b) the maximum cycle contraction force (c) beats per minute observed.

The typical captured contraction force curve shapes of the *in vitro* single axis measurements are different. The difference in the curve shapes may be explained with the different location of the measurement probe relative to the cardiac construct. With the first version of the separation method the single axis probe tip was attached to the cell construct on the outer edge, while in the force measurement with the second version separation method, the single axis probe tip was placed in the middle of the structure. Despite the differences in the curve shapes, the measured peak contraction forces and the beat rates have similar magnitudes.

In vitro cardiac construct contraction force measurements were also carried out with the L- shaped dual axis measurement probe. The maximum contraction force varied between 9.5 - 11.2 µN, standard deviation between 0.11 - 0.35 µN and the CV values between 1 and 2.5% in the measurements. The displacement amplitude of the force measurement L- shaped probe tip was approximately 1 µm in x- direction and 0.5 µm y- direction. Such small displacements are difficult to measure with optical microscope imaging, which has an inherent resolution limit of approximately 0.5 µm. Typical results obtained with the L- shaped measurement probe is illustrated in Figure 35(a) total force curve, (b) the tip displacement trajectory, (c) measured peak contraction force and (d) beat rate.

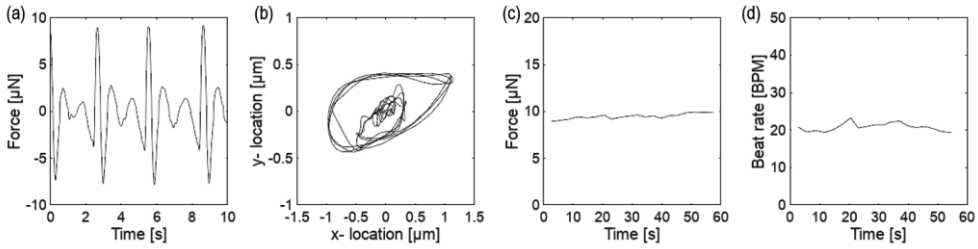

Figure 35. L- shaped dual axis *in vitro* contraction force measurement results with the second version of the separation method. (a) the contraction force curve (b) the measurement probe tip trajectory (c) the maximum cycle contraction force (d) beats per minute observed.

The measured maximum contraction force, the maximum force standard deviation and the corresponding CV of all conducted *in vitro* cardiac construct measurements and are summarized in Table 3.

Table 3. Summary of the *in vitro* contraction force measurement results.

Sensor	Maximum Contraction force [µN]	STD [µN]	CV [%]
Single axis with first separation method	3.0 - 6.7	0.54 - 1.4	9.2 - 16.8
Single axis with second separation method	3.4 - 6.7	0.13 - 0.22	3.3 - 4.1
L- shaped dual axis with second separation method	9.5 - 11.2	0.11 - 0.35	1.0 - 2.5

7.2.3 Pattern matching with the contraction force measurements

A pattern matching technique was applied to the L- shaped dual axis *in vitro* contraction force measurement data to classify the data into two categories. The classification was carried out based on how closely each measured cardiac cycle resembled a predefined template. The classification of the cycles is illustrated in Figures 36(a) - (c) where mean, median and 95% confidence level curves are shown from (a) the unprocessed cardiac cycle data where all the measured and identified cycles are present, (b) the matching cycles and (c) the discarded cycles. The largest deviation in the 95% confidence level curves show the areas of the greatest variation between the cycles and it appears to be at the bottom force peak and the end of the measured contraction cycles.

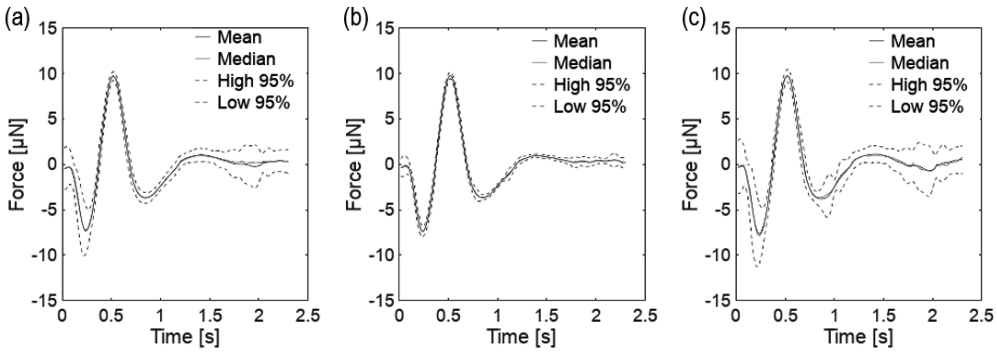

Figure 36. Mean, median and 95% confidence levels of (a) set of typical cardiac cycles, (b) the matching cycles and (c) the discarded cycles obtained by the L- shaped dual axis *in vitro* measurement system.

7.2.4 Summary of the *in vitro* force measurements

Both single and dual axis force measurement methods are capable of measuring force at the desired micro newton force range. The coefficients of variation of the *in vitro* peak force measurements were found relatively small in all test cases suggesting that the reliability of the measurement concept is good. Exact quantitative estimation of the variation caused by the measurement setup in the *in vitro* force measurements is difficult. It is not possible to know how large variation is contributed to the results by the variation in cardiac construct contraction force. Based on the measurement results, both studied contraction force measurement methods can be considered to be reliable measurement approaches for the cardiac construct contraction force measurement. Even though the repeatability of the measurement system is good when considering cycle to cycle variation, there might be error in the accuracy of the measurement as the long term effects of the measurements system were not studied.

The recorded peak forces obtained in the *in vitro* measurement were higher in the dual axis measurements compared to the single axis measurements. The location and orientation of the cantilever tip relative to the cardiac construct is likely to have an effect on the measurement results, especially in the case of the single axis measurements. Moreover, the mechanical properties of the measurement probe may also influence the results. The spring constant of the single axis cantilever probe was approximately 1 N/m, compared to the dual axis probe having spring constant of approximately 5 or 9 N/m, depending on the orientation of the measurement probe.

The smaller spring constant may have caused the single axis measurement to be more of a displacement measurement than a force measurement if the probe tip loading for the cardiac construct is too small.

Variation in contraction peak forces is likely to appear between different cardiac construct samples. Despite the fact that all the measured cell populations originated from the same cell batches and were cultured with the same procedure, the size, location(s) and orientation of the contracting tissue differ between populations. The measurements were carried out in different days, which has been shown to have an effect on the recorded peak cardiac contraction force readings (Kim et al. 2016; Kim et al. 2017).

Large variation of the measured cardiac contraction forces has been reported in the literature. Single cell cardiac contraction forces have been observed in nano newton range (Qu et al. 2019; Pesl et al. 2016; Rodriguez et al. 2014). With cardiac clusters or constructs the reported contraction forces are higher, in the order of hundred micro newtons (You et al. 2014; Mannhardt et al. 2016) to hundreds of micro newtons (Birla et al. 2005; Sasaki et al. 2018). The measured maximum contraction forces recorded in this work are in the middle of this range in the order of few micro newtons.

There is a difference in the measured contraction force curve shape depending on the separation method with both single and dual axis force measurements. The curve shape of the contraction force measured with the single axis cantilever and the first version of the separation method resemble those reported in the literature (Chang et al. 2013; Tanaka et al. 2006; Birla et al. 2005; Kim et al. 2016). On the other hand Pesl et al. (2016) have observed similar curve shapes which were obtained with AFM to resemble the contraction force curve shapes obtained with the second version separation method.

In the dual axis force measurement concept, the probe tip can move in two directions proving a two-dimensional representation of the cardiac construct contraction force. With the dual axis setup, the measured contraction force curve shapes appeared to have two different sized circles or ellipses in them. This suggests that the single axis force measurement concept may have limitations and may not work ideally in the *in vitro* force measurement setup in all cases.

8 SUMMARY AND CONCLUSIONS

Regarding the canine ECG measurement with dry electrodes the results of this thesis work can be summarized as the following:

1) Dry ECG electrodes can be successfully used in everyday canine ECG measurements without shaving or use of electrically conductive gel. Over 90% average coverage ratio is achievable with studied gold-plated electrodes in standing and sitting postures. Other than those two favorable test cases all studied electrodes have very similar coverage ratio performance and the design or material does not appear to have a significant impact on the QRS- complex detection.

2) Sitting posture yields the highest average coverage ratio values with all electrodes except the 12- pin polymeric electrode. Standing and sitting postures also result in higher overall coverage ratio values than lying posture or walking even if a robust QRS- complex detection algorithm is used. However overall average coverage ratios were above 40% in all of the test cases.

Regarding the cardiac construct contraction force measurement, the results can be summarized as the following:

3) A piezoelectric force measurement probe and an Arduino based electronics can be successfully and reliably used in micro newton range force measurements.

4) The cardiac construct contraction force measurement can be carried out *in vitro* with the proposed system using a piezoelectric force measurement probe as the sensor. The resolution of the force measurement achieved with this measurement concept is difficult to achieve *in vitro* with microscope imaging based force measurement approaches. The proposed methodology also allows the measurements to be performed in a complete darkness minimizing the photo toxicity effects during the measurements.

5) The *in vitro* cardiac construct contraction force measurement can be performed in a single and dual axis modes with the studied piezoelectric cantilever probes. The dual axis measurement approach may reveal more information of the contraction cycle than the single axis approach. Since the dual axis probe is capable of sensing in two dimensions it can reveal a probe tip trajectory. In the dual axis *in vitro* measurements carried out in this this appeared not to be linear but rather has circular or elliptical shape in it.

It is obvious that the performance of the dry ECG electrodes when used with hairy animals can be improved in many ways. One of the greatest challenges appears to be the electrode operation during movement or motion. By resolving this problem, it makes it truly possible to carry out long term biopotential measurements or more specifically ECG measurements with animals. As a consequence, this would enable data which is not available currently but which could reveal unknown information about dog, horse or other animal physiology or behavior.

A high-resolution contraction force measurement with two or even three dimensional force measurement capability could also open great opportunities. For example, it is currently not known how cardiac drugs affect the probe tip trajectory in the force measurements. This could be essential, since the heart as an organ operates in three dimensions and the contraction movement is also likely not to be linear.

Simultaneous contraction force measurement in multiple locations using a direct cantilever probe has not been explored. Further developing the force measurement concept presented in this work, a multiple location measurement could be carried out with a probe matrix. This could also provide better opportunity to compare action potential data obtained by an MEA system to the contraction force measurement results.

Heart is an organ which faces variable load during the operation. Therefore, development of the force measurement concepts where the loading could be dynamically changed in order to better mimic the real operation conditions of a heart would be desirable.

In conclusion, both of the studied topics in this work, especially if developed further, have the potential to change the way we understand human and animal physiology.

9 REFERENCES

Balaban, N. Q., Schwarz, U. S., Riveline, D., Goichberg, P., Tzur, G., Sabanay, I., ... & Geiger, B. (2001). Force and focal adhesion assembly: a close relationship studied using elastic micropatterned substrates. Nature cell biology, 3(5), 466.

Barrett, K., Barman, S., & Boitan, S. (2010). Ganong's review of medical physiology, McGraw Hill. Lange, USA.

Beckmann, L., Neuhaus, C., Medrano, G., Jungbecker, N., Walter, M., Gries, T., & Leonhardt, S. (2010). Characterization of textile electrodes and conductors using standardized measurement setups. Physiological measurement, 31(2), 233.

Bentley, J. P. (2005). Principles of measurement systems. Pearson education.

Birla, R. K., Borschel, G. H., Dennis, R. G., & Brown, D. L. (2005). Myocardial engineering in vivo: formation and characterization of contractile, vascularized three-dimensional cardiac tissue. Tissue engineering, 11(5-6), 803-813.

Borin, D., Pecorari, I., Pena, B., & Sbaizero, O. (2018, January). Novel insights into cardiomyocytes provided by atomic force microscopy. In Seminars in cell & developmental biology (Vol. 73, pp. 4-12). Academic Press.

Braam, S. R., Tertoolen, L., van de Stolpe, A., Meyer, T., Passier, R., & Mummery, C. L. (2010). Prediction of drug-induced cardiotoxicity using human embryonic stem cell-derived cardiomyocytes. Stem cell research, 4(2), 107-116.

Bronzino, J. D., & Peterson, D. R. (2014). Biomedical engineering fundamentals. CRC press.

Brugarolas, R., Dieffenderfer, J., Walker, K., Wagner, A., Sherman, B., Roberts, D., & Bozkurt, A. (2014, November). Wearable wireless biophotonic and biopotential sensors for canine health monitoring. In SENSORS, 2014 IEEE (pp. 2203-2206). IEEE.

Brugarolas, R., Latif, T., Dieffenderfer, J., Walker, K., Yuschak, S., Sherman, B. L., ... & Bozkurt, A. (2015). Wearable heart rate sensor systems for wireless canine health monitoring. IEEE Sensors Journal, 16(10), 3454-3464.

Buck, J. R., Oppenheim, A. V. V., & Schafer, A. V. (1998). Discrete-time signal processing.

Burridge, P. W., Keller, G., Gold, J. D., & Wu, J. C. (2012). Production of de novo cardiomyocytes: human pluripotent stem cell differentiation and direct reprogramming. Cell stem cell, 10(1), 16-28.

C. Mummery, D. Ward, C.E. Van den Brink, S.D. Bird, P.A. Doevendans, T. Opthof, D. La Riviere, A. Brutel, L. Tertoolen, M. Van Der Heyden (others) J. Anat., 200 (2002), pp. 233-242

Caspi, O., Itzhaki, I., Kehat, I., Gepstein, A., Arbel, G., Huber, I., ... & Gepstein, L. (2009). In vitro electrophysiological drug testing using human embryonic stem cell derived cardiomyocytes. Stem cells and development, 18(1), 161-172.

Chang, W. T., Yu, D., Lai, Y. C., Lin, K. Y., & Liau, I. (2013). Characterization of the mechanodynamic response of cardiomyocytes with atomic force microscopy. Analytical chemistry, 85(3), 1395-1400.

Chang, W. T., Yu, D., Lai, Y. C., Lin, K. Y., & Liau, I. (2013). Characterization of the mechanodynamic response of cardiomyocytes with atomic force microscopy. Analytical chemistry, 85(3), 1395-1400.

Chi, Y. M., Jung, T. P., & Cauwenberghs, G. (2010). Dry-contact and noncontact biopotential electrodes: Methodological review. IEEE reviews in biomedical engineering, 3, 106-119.

Chlaihawi, A. A., Narakathu, B. B., Emamian, S., Bazuin, B. J., & Atashbar, M. Z. (2018). Development of printed and flexible dry ECG electrodes. Sensing and bio-sensing research, 20, 9-15.

Cima, M. J. (2014). Next-generation wearable electronics. Nature biotechnology, 32(7), 642.

Combes, R. D., Berridge, T., Connelly, J., Eve, M. D., Garner, R. C., Toon, S., & Wilcox, P. (2003). Early microdose drug studies in human volunteers can minimise animal testing: Proceedings of a workshop organised by Volunteers in Research and Testing. European journal of pharmaceutical sciences, 19(1), 1-11.

Di Flumeri, G., Aricò, P., Borghini, G., Sciaraffa, N., Di Florio, A., & Babiloni, F. (2019). The dry revolution: evaluation of three different EEG dry electrode types in terms of signal spectral features, mental states classification and usability. Sensors, 19(6), 1365.

do Vale Madeiro, J. P., Cortez, P. C., Monteiro Filho, J. M. D. S., & Brayner, A. R. A. (Eds.). (2018). Developments and Applications for ECG Signal Processing: Modeling, Segmentation, and Pattern Recognition. Academic Press.

Doke, S. K., & Dhawale, S. C. (2015). Alternatives to animal testing: A review. Saudi Pharmaceutical Journal, 23(3), 223-229.

Duc, T. C., Creemer, J. F., & Sarro, P. M. (2006). Piezoresistive cantilever beam for force sensing in two dimensions. IEEE sensors journal, 7(1), 96-104.

Dunn, M. L., & Taya, M. (1993). Electromechanical properties of porous piezoelectric ceramics. Journal of the American Ceramic Society, 76(7), 1697-1706.

Enikov, E. T., & Nelson, B. J. (2000). Three-dimensional microfabrication for a multi-degree-of-freedom capacitive force sensor using fibre-chip coupling. Journal of Micromechanics and Microengineering, 10(4), 492.

Eschenhagen, T., Fink, C., Remmers, U., Scholz, H., Wattchow, J., Weil, J., ... & Wakatsuki, T. (1997). Three-dimensional reconstitution of embryonic cardiomyocytes in a collagen matrix: a new heart muscle model system. The FASEB journal, 11(8), 683-694.

Feaster, T. K., Cadar, A. G., Wang, L., Williams, C. H., Chun, Y. W., Hempel, J. E., ... & Knollmann, B. C. (2015). Matrigel mattress: a method for the generation of single contracting human-induced pluripotent stem cell–derived cardiomyocytes. Circulation research, 117(12), 995-1000.

Gargiulo, G., Bifulco, P., McEwan, A., Tehrani, J. N., Calvo, R. A., Romano, M., ... & Mohamed, A. (2010, August). Dry electrode bio-potential recordings. In 2010 Annual International Conference of the IEEE Engineering in Medicine and Biology (pp. 6493-6496). IEEE.

Gargiulo, G., Bifulco, P., McEwan, A., Tehrani, J. N., Calvo, R. A., Romano, M., ... & Mohamed, A. (2010, August). Dry electrode bio-potential recordings. In 2010 Annual International Conference of the IEEE Engineering in Medicine and Biology (pp. 6493-6496). IEEE.

Gautschi, G. (2002). Piezoelectric sensors. In Piezoelectric Sensorics (pp. 73-91). Springer, Berlin, Heidelberg.

Hamrell, B. B. (2018). Cardiovascular Physiology: A Text and E-Resource for Active Learning. CRC Press.

Haritha, C., Ganesan, M., & Sumesh, E. P. (2016, March). A survey on modern trends in ECG noise removal techniques. In 2016 International Conference on Circuit, Power and Computing Technologies (ICCPCT) (pp. 1-7). IEEE.

Harris, K., Aylott, M., Cui, Y., Louttit, J. B., McMahon, N. C., & Sridhar, A. (2013). Comparison of electrophysiological data from human-induced pluripotent stem cell–derived cardiomyocytes to functional preclinical safety assays. toxicological sciences, 134(2), 412-426.

Heinonen, T. (2015). Better science with human cell-based organ and tissue models. Alternatives to Laboratory Animals, 43(1), 29-38.

Heo, J. S., Eom, J., Kim, Y. H., & Park, S. K. (2018). Recent Progress of Textile-Based Wearable Electronics: A Comprehensive Review of Materials, Devices, and Applications. Small, 14(3), 1703034.

Hill, A. J., & Iaizzo, P. A. (2015). Comparative cardiac anatomy. In Handbook of cardiac anatomy, physiology, and devices (pp. 89-114). Springer, Cham.

Hill, J. D. (1968). The electrocardiogram in dogs with standardized body and limb positions. Journal of electrocardiology, 1(2), 175-182.

Hirt, M. N., Hansen, A., & Eschenhagen, T. (2014). Cardiac tissue engineering: state of the art. Circulation research, 114(2), 354-367.

Ifeachor, E. C., & Jervis, B. W. (2002). Digital signal processing: a practical approach. Pearson Education.

Jeyhani, V. (2017). A Wireless Device for Ambulatory Cardiac and Respiratory Monitoring-Design Considerations and Essential Performance.

Kaniusas, E. (2019). Biomedical Signals and Sensors III: Linking Electric Biosignals and Biomedical Sensors. Springer.

Karakikes, I., Ameen, M., Termglinchan, V., & Wu, J. C. (2015). Human induced pluripotent stem cell–derived cardiomyocytes: insights into molecular, cellular, and functional phenotypes. Circulation research, 117(1), 80-88.

Kar-Gupta, R., & Venkatesh, T. A. (2006). Electromechanical response of porous piezoelectric materials. Acta Materialia, 54(15), 4063-4078.

Khandpur, R. S. (2005). Biomedical instrumentation: Technology and applications (Vol. 1). New York: McGraw-Hill.

Kim, Dong-Su, et al. "Piezoresistive sensor-integrated PDMS cantilever: A new class of device for measuring the drug-induced changes in the mechanical activity of cardiomyocytes." Sensors and Actuators B: Chemical 240 (2017): 566-572.

Kim, J. Y., Choi, Y. S., Lee, B. K., & Lee, D. W. (2016). Surface-patterned SU-8 cantilever arrays for preliminary screening of cardiac toxicity. Biosensors and Bioelectronics, 80, 456-462.

Kim, J., Park, J., Na, K., Yang, S., Baek, J., Yoon, E., ... & Park, S. (2008). Quantitative evaluation of cardiomyocyte contractility in a 3D microenvironment. Journal of biomechanics, 41(11), 2396-2401.

Klabunde, R. (2011). Cardiovascular physiology concepts. Lippincott Williams & Wilkins.

Kristiansen, K., McGuiggan, P., Carver, G., Meinhart, C., & Israelachvili, J. (2008). 3D force and displacement sensor for SFA and AFM measurements. Langmuir, 24(4), 1541-1549.

Lee, P., Klos, M., Bollensdorff, C., Hou, L., Ewart, P., Kamp, T. J., ... & Jalife, J. (2012). Simultaneous voltage and calcium mapping of genetically purified human induced pluripotent stem cell–derived cardiac myocyte monolayers. Circulation research, 110(12), 1556-1563.

Li, J. F., Takagi, K., Ono, M., Pan, W., Watanabe, R., Almajid, A., & Taya, M. (2003). Fabrication and evaluation of porous piezoelectric ceramics and porosity–graded piezoelectric actuators. Journal of the American Ceramic Society, 86(7), 1094-1098.

Li, X., Zhang, R., Zhao, B., Lossin, C., & Cao, Z. (2016). Cardiotoxicity screening: a review of rapid-throughput in vitro approaches. Archives of toxicology, 90(8), 1803-1816.

Liang, Q., Zhang, D., Coppola, G., Wang, Y., Wei, S., & Ge, Y. (2014). Multi-dimensional MEMS/micro sensor for force and moment sensing: A review. IEEE Sensors Journal, 14(8), 2643-2657.

Limaye, H., & Deshmukh, V. V. (2016). ECG noise sources and various noise removal techniques: a survey. International Journal of Application or Innovation in Engineering & Management, 5(2), 86-92.

Linder, P., Trzewik, J., Rüffer, M., Artmann, G. M., Digel, I., Kurz, R., ... & Artmann, A. T. (2010). Contractile tension and beating rates of self-exciting monolayers and 3D-tissue constructs of neonatal rat cardiomyocytes. Medical & biological engineering & computing, 48(1), 59.

Liu, Y., Pharr, M., & Salvatore, G. A. (2017). Lab-on-skin: a review of flexible and stretchable electronics for wearable health monitoring. ACS nano, 11(10), 9614-9635.

Lopez-Izquierdo, A., Warren, M., Riedel, M., Cho, S., Lai, S., Lux, R. L., ... & Jou, C. J. (2014). A near-infrared fluorescent voltage-sensitive dye allows for moderate-throughput electrophysiological analyses of human induced pluripotent stem cell-derived cardiomyocytes. American Journal of Physiology-Heart and Circulatory Physiology, 307(9), H1370-H1377.

Mannhardt, I., Breckwoldt, K., Letuffe-Brenière, D., Schaaf, S., Schulz, H., Neuber, C., ... & Klampe, B. (2016). Human engineered heart tissue: analysis of contractile force. Stem cell reports, 7(1), 29-42.

Matsa, E., Rajamohan, D., Dick, E., Young, L., Mellor, I., Staniforth, A., & Denning, C. (2011). Drug evaluation in cardiomyocytes derived from human induced pluripotent stem cells carrying a long QT syndrome type 2 mutation. European heart journal, 32(8), 952-962.

McGrath, P., & Li, C. Q. (2008). Zebrafish: a predictive model for assessing drug-induced toxicity. Drug discovery today, 13(9-10), 394-401.

Mills, R. J., Parker, B. L., Quaife-Ryan, G. A., Voges, H. K., Needham, E. J., Bornot, A., ... & Drowley, L. (2019). Drug screening in human PSC-cardiac organoids identifies pro-proliferative compounds acting via the mevalonate pathway. Cell stem cell.

Moretti, A., Laugwitz, K. L., Dorn, T., Sinnecker, D., & Mummery, C. (2013). Pluripotent stem cell models of human heart disease. Cold Spring Harbor perspectives in medicine, 3(11), a014027.

Muhlsteff, J., & Such, O. (2004, September). Dry electrodes for monitoring of vital signs in functional textiles. In The 26th Annual International Conference of the IEEE Engineering in Medicine and Biology Society (Vol. 1, pp. 2212-2215). IEEE.

Mukhopadhyay, S. C. (2014). Wearable sensors for human activity monitoring: A review. IEEE sensors journal, 15(3), 1321-1330.

Myachina, T., Khokhlova, A., Antsygin, I., & Lookin, O. (2018, May). An Approach for Improvement of Carbon Fiber Technique to Study Cardiac Cell Contractility. In IOP

Conference Series: Materials Science and Engineering (Vol. 350, No. 1, p. 012011). IOP Publishing.
Myers, A. C., Huang, H., & Zhu, Y. (2015). Wearable silver nanowire dry electrodes for electrophysiological sensing. Rsc Advances, 5(15), 11627-11632.
Nag, A., Mukhopadhyay, S. C., & Kosel, J. (2017). Wearable flexible sensors: A review. IEEE Sensors Journal, 17(13), 3949-3960.
Nieuwenhuizen, R. P., Lidke, K. A., Bates, M., Puig, D. L., Grünwald, D., Stallinga, S., & Rieger, B. (2013). Measuring image resolution in optical nanoscopy. Nature methods, 10(6), 557.
Official Statistics of Finland (OSF): Causes of death [e-publication]. ISSN=1799-5078. 2017, 1. Causes of death in 2017 . Helsinki: Statistics Finland [referred: 17.1.2020].Access method: http://www.stat.fi/til/ksyyt/2017/ksyyt_2017_2018-12-17_kat_001_en.html
Olson, H., Betton, G., Robinson, D., Thomas, K., Monro, A., Kolaja, G., ... & Dorato, M. (2000). Concordance of the toxicity of pharmaceuticals in humans and in animals. Regulatory Toxicology and Pharmacology, 32(1), 56-67.
Ottenbacher, J., & Heuer, S. (2009). Motion artefacts in capacitively coupled ECG electrodes. In World Congress on Medical Physics and Biomedical Engineering, September 7-12, 2009, Munich, Germany (pp. 1059-1062). Springer, Berlin, Heidelberg.
Oyunbaatar, N. E., Shanmugasundaram, A., & Lee, D. W. (2019). Contractile behaviors of cardiac muscle cells on mushroom-shaped micropillar arrays. Colloids and Surfaces B: Biointerfaces, 174, 103-109.
Pani, D., Dessì, A., Saenz-Cogollo, J. F., Barabino, G., Fraboni, B., & Bonfiglio, A. (2015). Fully textile, PEDOT: PSS based electrodes for wearable ECG monitoring systems. IEEE Transactions on Biomedical Engineering, 63(3), 540-549.
Paradiso, R., Loriga, G., & Taccini, N. (2005). A wearable health care system based on knitted integrated sensors. IEEE transactions on Information Technology in biomedicine, 9(3), 337-344.
Park, J., Ryu, J., Choi, S. K., Seo, E., Cha, J. M., Ryu, S., ... & Lee, S. H. (2005). Real-time measurement of the contractile forces of self-organized cardiomyocytes on hybrid biopolymer microcantilevers. Analytical chemistry, 77(20), 6571-6580.
Parng, C. (2005). In vivo zebrafish assays for toxicity testing. Current opinion in drug discovery & development, 8(1), 100-106.
Parng, C., Seng, W. L., Semino, C., & McGrath, P. (2002). Zebrafish: a preclinical model for drug screening. Assay and drug development technologies, 1(1), 41-48.
Pesl, M., Pribyl, J., Acimovic, I., Vilotic, A., Jelinkova, S., Salykin, A., ... & Rotrekl, V. (2016). Atomic force microscopy combined with human pluripotent stem cell derived cardiomyocytes for biomechanical sensing. Biosensors and Bioelectronics, 85, 751-757.
Pointon, A., Harmer, A. R., Dale, I. L., Abi-Gerges, N., Bowes, J., Pollard, C., & Garside, H. (2014). Assessment of cardiomyocyte contraction in human-induced pluripotent stem cell-derived cardiomyocytes. Toxicological Sciences, 144(2), 227-237.
Puurtinen, M. M., Komulainen, S. M., Kauppinen, P. K., Malmivuo, J. A., & Hyttinen, J. A. (2006, August). Measurement of noise and impedance of dry and wet textile electrodes, and textile electrodes with hydrogel. In 2006 International Conference of the IEEE Engineering in Medicine and Biology Society (pp. 6012-6015). IEEE.

Qu, Y., & Vargas, H. M. (2015). Proarrhythmia risk assessment in human induced pluripotent stem cell-derived cardiomyocytes using the maestro MEA platform. Toxicological Sciences, 147(1), 286-295.

Qu, Y., Zhao, F., Wang, X., Liu, J., Li, J., Song, Z., & Wang, Z. (2019). Cardiomyocyte contractile force changes in response to AGRWE detected by AFM. Micro & Nano Letters, 14(5), 511-514.

Rajan, D. K., Kreutzer, J., Välimäki, H., Pekkanen-Mattila, M., Ahola, A., Skogberg, A., ... & Lekkala, J. (2018). A Portable Live-Cell Imaging System With an Invert-Upright-Convertible Architecture and a Mini-Bioreactor for Long-Term Simultaneous Cell Imaging, Chemical Sensing, and Electrophysiological Recording. IEEE Access, 6, 11063-11075.

Ranganatha, N., & Kuppast, I. J. (2012). A review on alternatives to animal testing methods in drug development. International Journal of Pharmacy and Pharmaceutical Sciences, 4(SUPPL 5), 28-32.

Rao, S. S. (1995). Mechanical Vibrations Laboratory Manual. Year, Edition Addison-Wesley Publishing Company.

Reppel, M., Pillekamp, F., Brockmeier, K., Matzkies, M., Bekcioglu, A., Lipke, T., ... & Hescheler, J. (2005). The electrocardiogram of human embryonic stem cell–derived cardiomyocytes. Journal of electrocardiology, 38(4), 166-170.

Rodriguez, M. L., Graham, B. T., Pabon, L. M., Han, S. J., Murry, C. E., & Sniadecki, N. J. (2014). Measuring the contractile forces of human induced pluripotent stem cell-derived cardiomyocytes with arrays of microposts. Journal of biomechanical engineering, 136(5), 051005.

Salvo, P., Raedt, R., Carrette, E., Schaubroeck, D., Vanfleteren, J., & Cardon, L. (2012). A 3D printed dry electrode for ECG/EEG recording. Sensors and Actuators A: Physical, 174, 96-102.

Sasaki, D., Matsuura, K., Seta, H., Haraguchi, Y., Okano, T., & Shimizu, T. (2018). Contractile force measurement of human induced pluripotent stem cell-derived cardiac cell sheet-tissue. PloS one, 13(5), E0198026.

Shimizu, Koushi, et al. "Multi-scale reconstruction and performance of insect muscle powered bioactuator from tissue to cell sheet." Biomedical Robotics and Biomechatronics (BioRob), 2010 3rd IEEE RAS and EMBS International Conference on. IEEE, 2010.

Sidorov, V. Y., Samson, P. C., Sidorova, T. N., Davidson, J. M., Lim, C. C., & Wikswo, J. P. (2017). I-Wire Heart-on-a-Chip I: Three-dimensional cardiac tissue constructs for physiology and pharmacology. Acta biomaterialia, 48, 68-78.

Ştefănescu, D. M., & Anghel, M. A. (2013). Electrical methods for force measurement–A brief survey. Measurement, 46(2), 949-959.

Stoppa, M., & Chiolerio, A. (2014). Wearable electronics and smart textiles: a critical review. sensors, 14(7), 11957-11992.

Su, C., Huang, L., & Kjoller, K. (2004). Direct measurement of tapping force with a cantilever deflection force sensor. Ultramicroscopy, 100(3-4), 233-239.

Sugiura, Seiryo, et al. "Carbon fiber technique for the investigation of single-cell mechanics in intact cardiac myocytes." Nature protocols 1.3 (2006): 1453.

Takahashi, K., Tanabe, K., Ohnuki, M., Narita, M., Ichisaka, T., Tomoda, K., & Yamanaka, S. (2007). Induction of pluripotent stem cells from adult human fibroblasts by defined factors. cell, 131(5), 861-872.

Tanaka, Y., Morishima, K., Shimizu, T., Kikuchi, A., Yamato, M., Okano, T., & Kitamori, T. (2006). Demonstration of a PDMS-based bio-microactuator using cultured cardiomyocytes to drive polymer micropillars. Lab on a Chip, 6(2), 230-235.

Tibrewala, A., Hofmann, N., Phataralaoha, A., Jäger, G., & Büttgenbach, S. (2009). Development of 3D force sensors for nanopositioning and nanomeasuring machine. Sensors, 9(5), 3228-3239.

Timmis, A., Townsend, N., Gale, C., Grobbee, R., Maniadakis, N., Flather, M., ... & Blum, M. (2017). European Society of Cardiology: cardiovascular disease statistics 2017. European heart journal, 39(7), 508-579.

Virtanen, J., Sariola, V., & Tuukkanen, S. (2018, August). Piezoelectric cantilever force sensor sensitivity measurements. In Journal of Physics: Conference Series (Vol. 1065, No. 4, p. 042005). IOP Publishing.

Vuorenpää, H., Ikonen, L., Kujala, K., Huttala, O., Sarkanen, J. R., Ylikomi, T., ... & Heinonen, T. (2014). Novel in vitro cardiovascular constructs composed of vascular-like networks and cardiomyocytes. In Vitro Cellular & Developmental Biology-Animal, 50(4), 275-286.

Vuorenpää, H., Penttinen, K., Heinonen, T., Pekkanen-Mattila, M., Sarkanen, J. R., Ylikomi, T., & Aalto-Setälä, K. (2017). Maturation of human pluripotent stem cell derived cardiomyocytes is improved in cardiovascular construct. Cytotechnology, 69(5), 785-800.

Vyas, V., Nagarajan, N., Zorlutuna, P., & Huey, B. D. (2017). Nanostethoscopy: atomic force microscopy probe contact force versus measured amplitude of cardiomyocytic contractions. Journal of Bionanoscience, 11(4), 319-322.

Wei, Y., & Xu, Q. (2015). An overview of micro-force sensing techniques. Sensors and Actuators A: Physical, 234, 359-374.

Wiese, S. R., Anheier, P., Connemara, R. D., Mollner, A. T., Neils, T. F., Kahn, J. A., & Webster, J. G. (2004). Electrocardiographic motion artifact versus electrode impedance. IEEE transactions on biomedical engineering, 52(1), 136-139.

Windmiller, J. R., & Wang, J. (2013). Wearable electrochemical sensors and biosensors: a review. Electroanalysis, 25(1), 29-46.

Yang, J. (2005). An introduction to the theory of piezoelectricity (Vol. 9). New York: Springer.

Yin, S., Zhang, X., Zhan, C., Wu, J., Xu, J., & Cheung, J. (2005). Measuring single cardiac myocyte contractile force via moving a magnetic bead. Biophysical journal, 88(2), 1489-1495.

You, J., Moon, H., Lee, B. Y., Jin, J. Y., Chang, Z. E., Kim, S. Y., ... & Kim, J. (2014). Cardiomyocyte sensor responsive to changes in physical and chemical environments. Journal of biomechanics, 47(2), 400-409.

Ziegler, C. (2004). Cantilever-based biosensors. Analytical and bioanalytical chemistry, 379(7-8), 946-959.

10 ORIGINAL PUBLICATIONS

sensors

MDPI

Article

Evaluation of Dry Electrodes in Canine Heart Rate Monitoring

Juhani Virtanen [1,*], Sanni Somppi [2], Heini Törnqvist [2], Vala Jeyhani [1], Patrique Fiedler [3], Yulia Gizatdinova [4], Päivi Majaranta [4], Heli Väätäjä [4], Anna Valldeoriola Cardó [2], Jukka Lekkala [1], Sampo Tuukkanen [1], Veikko Surakka [4], Outi Vainio [2] and Antti Vehkaoja [1]

1 BioMediTech Institute and Faculty of Biomedical Sciences and Engineering, Tampere University of Technology (TUT), P.O. Box 692, FI-33101 Tampere, Finland; vala.jeyhani@tut.fi (V.J.); jukka.lekkala@tut.fi (J.L.); sampo.tuukkanen@tut.fi (S.T.); antti.vehkaoja@tut.fi (A.V.)

2 Department of Equine and Small Animal Medicine, University of Helsinki (UH), P.O. Box 57 (Viikintie 49), FI-00014 Helsinki, Finland; sanni.somppi@helsinki.fi (S.S.); heini.tornqvist@helsinki.fi (H.T.); anna.valldeoriola@helsinki.fi (A.V.C.); outi.vainio@helsinki.fi (O.V.)

3 Institute of Biomedical Engineering and Informatics, Technische Universität Ilmenau, Gustav-Kirchhoff-Straße 2, 98693 Ilmenau, Germany; patrique.fiedler@tu-ilmenau.de

4 Research Group for Emotions, Sociality, and Computing, Faculty of Communication Sciences, University of Tampere (UTA), Pinni B Building, Kanslerinrinne 1, FI-33014 Tampere, Finland; julia.kuosmanen@uta.fi (Y.G.); paivi.majaranta@uta.fi (P.M.); heli.vaataja@tut.fi (H.V.); veikko.surakka@uta.fi (V.S.)

* Correspondence: juhani.virtanen@tut.fi; Tel.: +358-50-4114940

Received: 24 April 2018; Accepted: 29 May 2018; Published: 30 May 2018

Abstract: The functionality of three dry electrocardiogram electrode constructions was evaluated by measuring canine heart rate during four different behaviors: Standing, sitting, lying and walking. The testing was repeated (n = 9) in each of the 36 scenarios with three dogs. Two of the electrodes were constructed with spring-loaded test pins while the third electrode was a molded polymer electrode with Ag/AgCl coating. During the measurement, a specifically designed harness was used to attach the electrodes to the dogs. The performance of the electrodes was evaluated and compared in terms of heartbeat detection coverage. The effect on the respective heart rate coverage was studied by computing the heart rate coverage from the measured electrocardiogram signal using a pattern-matching algorithm to extract the R-peaks and further the beat-to-beat heart rate. The results show that the overall coverage ratios regarding the electrodes varied between 45–95% in four different activity modes. The lowest coverage was for lying and walking and the highest was for standing and sitting.

Keywords: dry electrode; heart rate canine

1. Introduction

Animal computer interaction (ACI) is a new, emerging discipline with significant commercial potential [1]. Its roots are in agriculture, animal welfare, and animal behavior research [2]. However, research specifically focusing on interaction between humans, animals and technology is still rather scarce, and mostly exploratory [3]. At the same time, especially the business related to tracking and monitoring of pets' behavior is growing fast [4]. One emerging direction in developing measurement technology is to interpret and understand how animal well-being relates to dog's emotions and emotional problems [5]. Dogs can suffer from anxiety, phobias and aggression. A range of serious anxiety-related behavior problems, including noise phobias, separation anxiety and aggression have been found to exist in dogs [6].

It has been suggested that measurement of heart rate (HR) and heart rate variability (HRV) could reflect a dog's emotional responses and stress, as well as serve as an indicator of a dog's welfare [3,5]. However, there is a need for further validation on the association of a dog's well-being with HRV [6–8]. In addition to that, the measurement technology for obtaining HRV information should be improved to suit for continuous everyday use. Polar technology [9], for example, has been validated for HRV measurement in dogs. However, the studies have applied relatively narrow circumstances in which the dog was steady in a standing position [10,11]. Thus, there is a clear need to develop technology that could function reliably in more versatile conditions, like standing and walking outside of clinical contexts and other similar situations.

Due to the above reasons, there has been a growing interest to monitor pet HR and respiratory activity. Electrocardiogram (ECG) electrodes have also been reported to be used with animals [8]. Typically, the HR of dogs has been measured using rubber electrodes (e.g., Polar® chest strap, Polar Electro oy, Kempele, Finland) with electrically conductive gel [12] or adhesive disposable electrodes that require shaving of the fur [5]. These techniques are questionable when HR is monitored outside the clinical applications in everyday environments. Recurrent shaving of a dog's fur is not convenient for the dog or the owner, nor is the use of conductive gel. Despite the conductive gel, poor electrode conduction may cause problems while the dog is moving freely [12]. This mandates a need for a maintenance-free electrode system which could provide the HR data constantly and reliably for long periods of time.

In this study, the main focus was to concentrate on the dry electrodes that could be used with thick and dense haired animals without shaving the fur and also without using electrolyte gels or other conductivity promoters. Our goal was to find out whether these electrodes could be used in maintenance-free canine heart rate monitoring. A literature review revealed that different types of pin electrodes, patches and tape electrodes have been used in animal HR measurements. In this study, the pin type electrode was taken into a more detailed investigation as it is the type of electrode that demonstrated promising results when placed on the hairy regions of a dog (e.g., [13]). Two new types of pin electrodes and one new molded polymer electrode were created and tested in this study. Preliminary measurements were carried out to obtain information about the reliability and usefulness of the electrodes in different use scenarios, and produce insights into further investigation and improvement of the measurement technology. The electrodes were evaluated in terms of heart rate coverage. The found individual heartbeats were further used to calculate heart rate coverage during different activities. In particular, the effect of different dog activity modes—standing, sitting, lying and walking—to the heart rate coverage was in the study focus. The results were verified by a human observer to ensure that the algorithm performed correctly.

2. Materials and Methods

The measurement system consisted of four electrodes in their respective housings. These were attached to a harness, which the dog wore during the measurements. The data was collected as an ECG potential measurement with a portable device, which along with the ECG data also recorded the accelerometer information. This collected data was later downloaded from the measurement device and further processed offline.

2.1. The Mechanical Setup of the Electrodes

Electrodes and the housings in which the electrodes were attached during the measurements were designed and constructed. Additionally, a wearable neoprene harness was designed and fabricated for fixing and attaching the electrodes to the desired locations on the dog's body. At first, fixtures and fixture molds were designed, CAD modeled and 3D-printed from polylactide (PLA) using an FDM printer (Prusa i3 MK2, Prusa Research s.r.o., Prague, Czech Republic). Later, silicone rubber fixtures were cast into the 3D-printed molds.

Two different spring-loaded electrodes were newly constructed and evaluated. Additionally, polymer electrodes with Ag/AgCl coating, prepared by the University of Ilmenau, were studied [14]. The spring-loaded electrodes were fabricated by soldering spring-loaded test pins in an array form on a printed wiring board. The first electrode type contained 37 test pins of type j75-1. Additionally, this electrode had a 5 mm thick PLA plate on it, as shown in Figure 1a. The second electrode type, a non-spring-loaded Ag/AgCl-coated polymer electrode with 30 pins, is shown in Figure 1b and the third electrode with 12 gold-plated test pins of type Tangda M1071, is shown in Figure 1c. The height of the pins of all electrodes was approximately 6 mm. All the pins in the electrodes were electrically connected together and, therefore the electrical potential was integrated over the contact area of all pins. The electrode configurations are also listed in Table 1.

Table 1. Electrode housing configurations used in the study.

Electrode	Peak	Polymer	Gold
Contacts	j75-1	Ag/AgCl-polymer	M1071
Housing	Neoprene	Silicone rubber	Silicone rubber
Pins	37	30	12

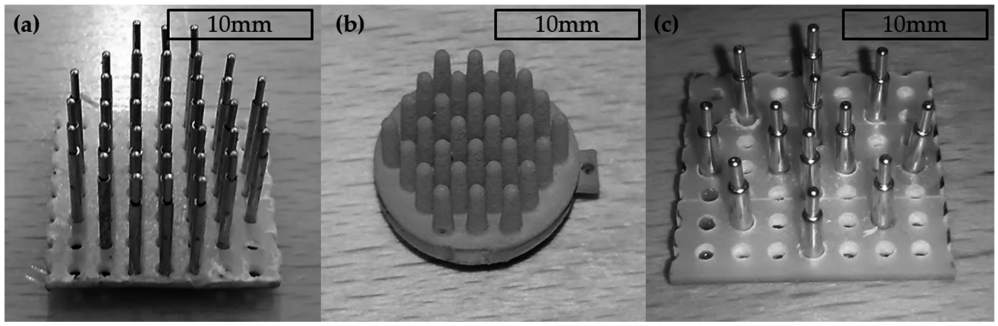

Figure 1. Electrodes: (**a**) The spring-loaded j75-1 test pins; (**b**) The Ag/AgCl-coated polymer electrode; (**c**) The electrode with gold-plated spring-loaded test pins.

2.2. The Housing of the Electrodes

Two different electrode housings were fabricated. The first housing was constructed of a printed PLA plate, shown in Figure 2a, and a sheet 2 mm thick, textile-coated neoprene rubber through which the spring-loaded pins were pushed, as Figure 2d illustrates.

The second type of housing was cast from silicone rubber (Zhermack ZA RTV 30-60, Zhermack SpA, Badia Polesine, Italy) into a custom designed 3D-printed two-part casting mold. This housing was used with both polymer and gold electrodes. Figure 3a shows a top and bottom view of the silicone rubber mold. The molded fixation parts are shown in Figure 3b. The aim of using silicone rubber in the housing was to enable more evenly distributed surface pressure and more comfortable wearing of the electrode.

After the initial casting, the electrodes were placed in to the cast silicone fixtures and a second casting was performed in order to make an integral electrode silicone rubber structure. This is illustrated in Figure 2b,c, where the polymer and gold electrodes are placed in to the initial castings, respectively. The polymer and gold electrodes after the second silicone rubber casting are shown in Figure 2e,f, respectively.

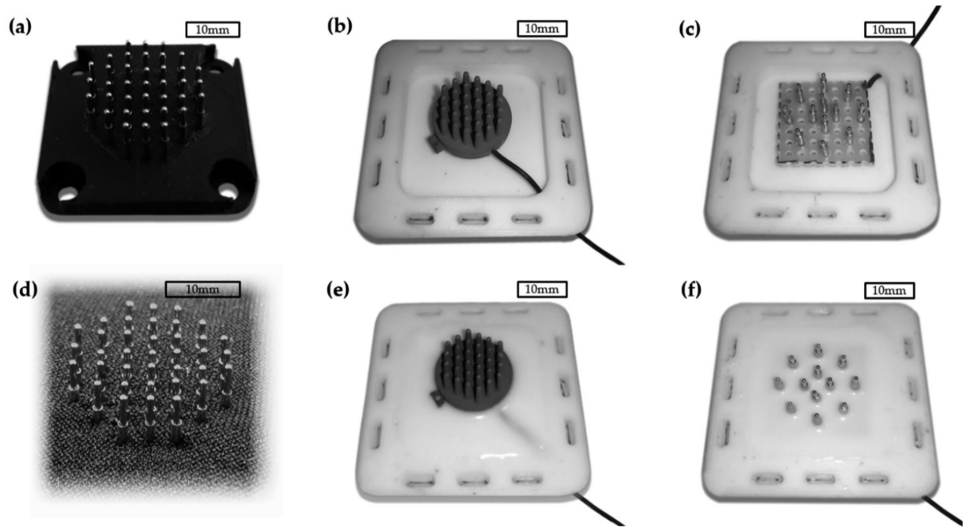

Figure 2. The electrodes embedded into housings: (**a**) Peak electrode with PLA plate; (**b**) Ag/AgCl-coated polymer electrode before the second casting; (**c**) Gold electrode before the second casting; (**d**) Peak electrode in the neoprene fixture; (**e**) Ag/AgCl coated polymer electrode in the silicone rubber fixture; (**f**) Gold electrode in the silicone rubber fixture.

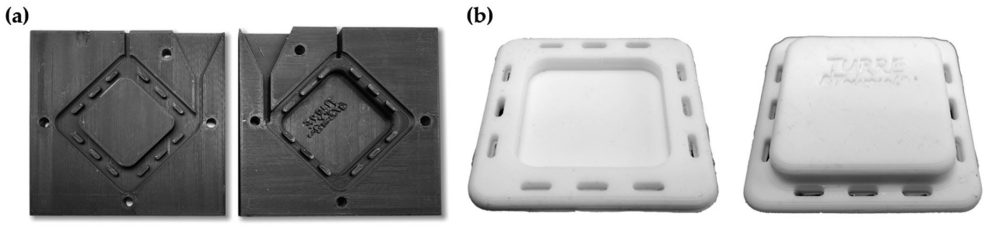

Figure 3. (**a**) Mold for the silicone rubber housing casting; (**b**) Cast silicone rubber electrode housing.

2.3. The Harnesses

Two different harnesses were used during the measurement to ensure a proper location of the electrodes and as equal surface pressure conditions as possible for all electrodes. Both harnesses were constructed of textile-coated elastic neoprene rubber. The first version was made of 2 mm neoprene with a velcro-coated outside layer. The second version was made of 3 mm thick neoprene and in addition to the velcro layer, it had polyester lining. The harnesses consisted of separately adjustable parts (chest belt around the dog's thorax and frontal belt around the chest), which were attached together with velcro fastener ensuring that the harnesses were ergonomic and comfortable for dogs. The electrodes were integrated to the lower part of the belt around the chest, two electrodes near to both armpits. The harnesses with the integrated electrodes and monitoring device were put on the dog as shown in Figure 4a. Four electrodes were used in a single measurement setup the of locations of the particular electrodes. The attachment of the polymer and gold electrodes can be seen in Figure 4b. The hair of the dogs was not shaved for the measurements. Neither was any electrode paste or other electrolyte used.

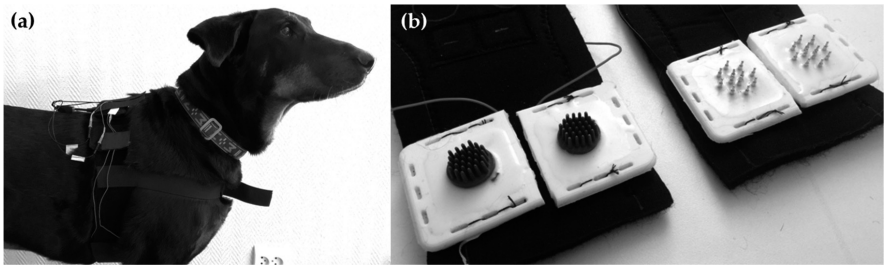

Figure 4. (**a**) The second version of the neoprene harness placed on the dog; (**b**) Polymer and gold electrodes attached to the neoprene harness.

2.4. Measurement Electronics

A custom made physiological monitoring device named SpiritCor9D was used to record ECG data with 250 Hz sampling frequency. In particular, the measurement device recorded three channels of ECG, impedance pneumography signal, and 3D acceleration and gyroscope data. The data was stored on the internal memory of the monitoring device and later extracted for the analysis performed on a PC computer. Unshielded electrode wires were used to connect the measurement electronics with the electrodes.

2.5. Measurement Trial Configuration

The animal experiments were conducted at the University of Helsinki. The procedures were approved by the Ethical Committee for the Use of Animals in experiments at the University of Helsinki (statement 2/2018). Three dogs were invited to participate in the test measurements. The dogs were two female Beauce Shepherds (Dog 1: 9 years, 32 kg; Dog 3: 8 years, 38 kg, short hair with undercoat) and one male Hovawart (Dog 2: 11 years, 35 kg, and long hair with undercoat).

The testing was organized in 36 different measurement scenarios (three electrodes, three dogs, four activities). Each of these measurement scenarios were repeated nine times (n = 9) in three testing sessions to obtain more reliable measurement results. One testing session consisted of three cycles of a sequence of behaviors, namely, standing 60 s; sitting 60 s; lying 60 s; and walking 60 s, with a settling time of approximately 10 s. The blocks were performed in succession forming a total duration of 12 min per session. The four different activity or posture modes were: standing, sitting, lying and walking. During the walking mode, the handler moved at walking speed while the dog followed unleashed keeping the same speed. The dogs were allowed to trot and pace to keep their speed. Walking mode included multiple sharp turns. Before each testing session, the dog was freely moving for one minute, to get accustomed to the harness. The measurement harness was taken off and put back on between the measurement sessions.

2.6. Heartbeat Detection and Heart Rate Analysis

The three electrode types were compared using ECG R-peak coverage ratios. R-peak was defined as the ratio between a successfully recovered R-peak time divided by the total test measurement time. Thus, a fully recovered HR data would yield a coverage ratio of 1.

R-peak detection is a standard operation in HR monitoring devices. There is a large variety of methods developed and published for R-peak detection from the measured EGC data, some of them were developed especially for integration on a low-performance microcontroller [15–17]. A pattern matching type R-peak detection method, derived from the method proposed by Dobbs et al. [16] was applied to detect the R-peaks in this study. The principles of the algorithm used in this evaluation have been presented with ECG compression algorithms [18]. In short, the data firstly filtered and scaled, and after this a pattern matching method was applied as follows.

Coverage ratios were computed for each activity mode and each dog. The measured raw ECG and filtered ECG data with different respective activity modes, is presented in Figure 5. The measurement data was manually split into to groups. In the figure, the horizontal time axis is matched such that the graphs are vertically aligned. The red rectangle in each of the graphs represents the area that is zoomed in to reveal more details in the data. The zoomed graphs (red rectangles from Figure 5) that represent a time period of 4 s, are shown in Figure 6.

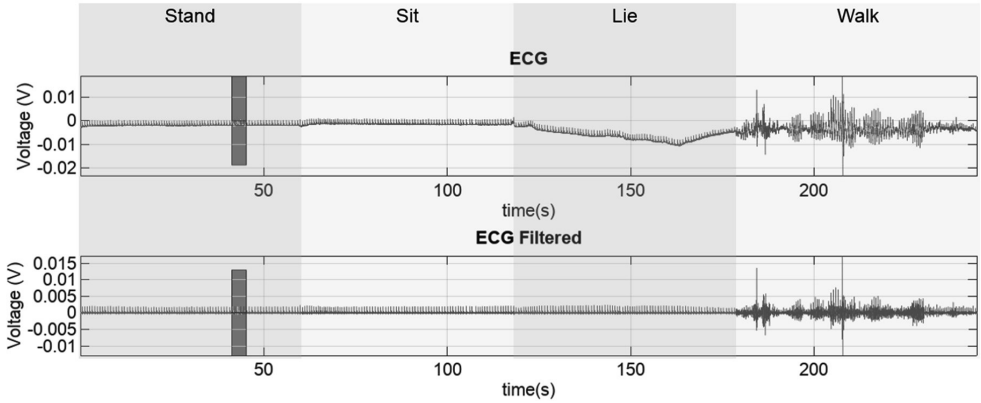

Figure 5. Illustration of the measured and filtered ECG data. Red rectangles denote the parts of the original signal that will be depicted in detail in Figure 6.

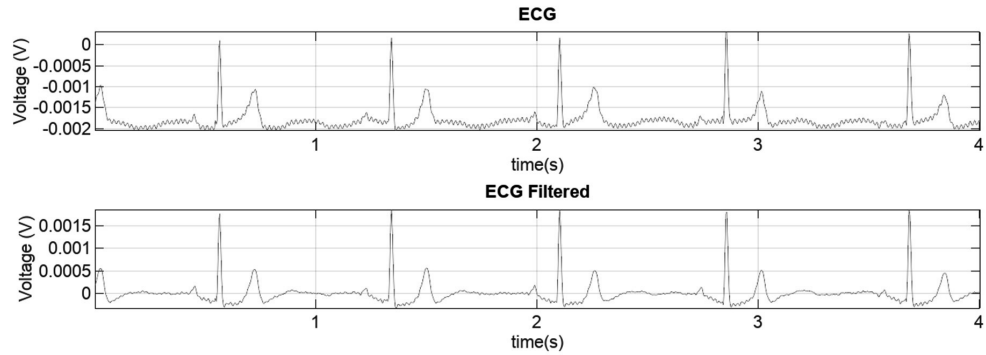

Figure 6. Zoomed-in raw and filtered ECG data. The data comes from the original signals presented in Figure 5 that are marked by red rectangles.

The processing was carried out by first applying a fourth order 2–30 Hz Butterworth forward-backward band pass filtering. Next, a pattern finder procedure was applied to the filtered data to find individual heartbeats in the ECG and to obtain the HR. In this procedure, first a typical template (Figure 7) of ECG pattern is selected. In particular, the pattern was obtained by visually analyzing the filtered ECG data and selecting a typical ECG pattern. The template pattern contains all essential components of an ECG from P to T waves in order to minimize the false detection of the complexes. This templated pattern was 250 ms in length in all analyzed computations. The template length was selected empirically to contain all the ECG components of one cardiac cycle from atrial depolarization (P-wave) to ventricular repolarization (T-wave). Next, the template was normalized such that the maximum value of the template (R-peak) corresponded to a value of 1 and all other values in this ECG vector were scaled linearly with the same normalizing factor.

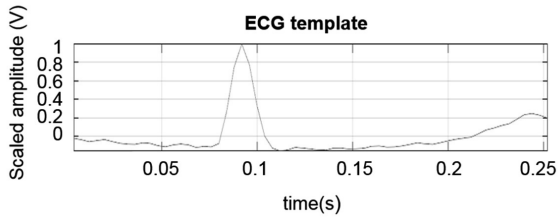

Figure 7. A typical scaled EGC template pattern that was used in pattern matching.

After the template assignment, the data was split into windows to perform adaptive amplitude scaling for the data. This processing phase started by defining an observation window length. The length was selected in such a way that it was longer than the maximum normal R-R-interval to ensure that in this window at least one R-peak would be present. In this particular case, the window length was selected to be 2 s to ensure the presence of the potential R-peak. Next, the data in the observation window was processed such that the sample with a maximum value in the data window was scaled to 1 and all other values in the vector were scaled linearly with the same coefficient. The actual pattern matching was then performed by computing the sum of the squared difference of the template and the observation window when the template was moved along the observation window vector. This windowing procedure was repeated to process the whole data.

In order to distinguish the matched pattern, a threshold of the distances which identifies a matched pattern was defined. Below this threshold level, the two vectors were interpreted to match and thus an R-peak was detected. The threshold level was visually observed from the output of the pattern match distance calculation. Care was taken to select the practical threshold level empirically such that false R-peak detections were minimized. In this particular study, an empirically defined threshold value of 0.3 was used. This yielded to less than 1% of false R-peak detections when the result was visually inspected against the filtered ECG data.

Thresholding the pattern matcher output data gives the location of the pattern match. This can also be interpreted as the location of the R-peak or the local minimum of the template data distance. This data was then used to compute the R-R interval signal values, which is the time elapsed between two detected R-peaks. A graph of the raw pattern match data and the respective RR-interval tachogram along with the different respective activity modes, is presented in Figure 8. A zoomed in (red rectangle) representation of these values can be seen in Figure 9. Finally, the coverage was computed as the ratio of successfully detected R-R interval signal time versus total measurement time.

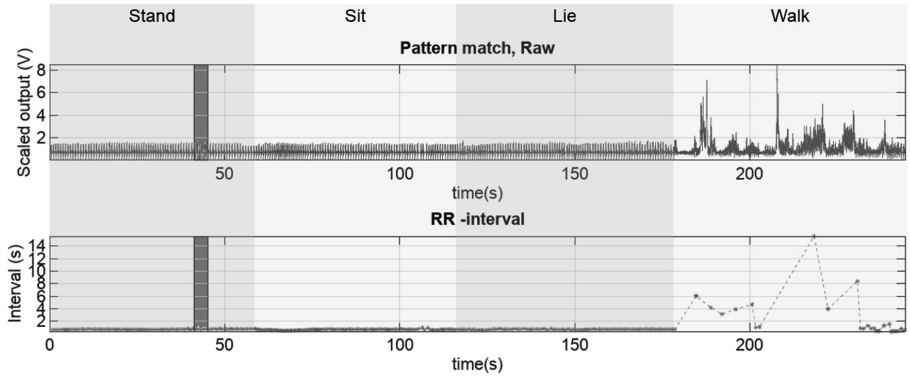

Figure 8. Raw pattern match data and its respective RR interval graph. Red rectangles denote the parts of the original signal that will be depicted in detail in Figure 9.

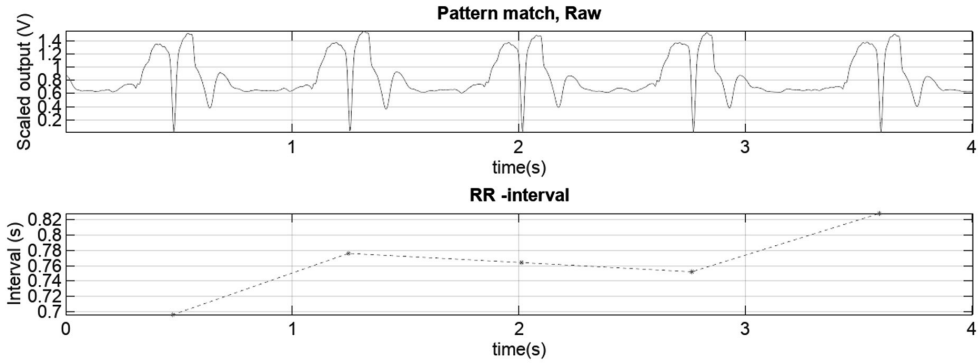

Figure 9. A zoomed-in representation of the scaled vector distance from the template pattern and the respective zoomed-in RR interval graph.

3. Measurement Results

Electrode coverage ratio averages (n = 27/activity) including all dogs and all electrodes varied between 0.45 and 0.95 with respect to the different activity. The standard deviation of the RR-interval coverage varied between 0.08 and 0.36. Furthermore, the median values varied between 0.44 and 0.99. Finally, the coverage ratio ranges varied between and 0.35 and 0.98. These average, standard deviation, median and range values are listed in Table 2. When additionally considering all the measurement scenarios and activity modes in separate cases regarding different electrodes (n = 9/activity), the average coverage ratios varied between 0.18 and 0.96, standard deviations between 0.06 and 0.42, medians between 0.17 and 1.00, and finally ranges between 0.08 and 0.97. The results are listed in Table 3 according to each electrode. The maximum and minimum values in all categories are highlighted in a bold typeface in Tables 2 and 3.

The heart rate/heartbeat detection coverages for each electrode type and activity obtained with all three dogs and in all test repetitions (n = 27/activity) are presented as boxplots in Figure 10. In Figure 11, the same results are presented for each dog separately (n = 9/activity).

Statistically significant differences in electrodes were investigated by performing a Mann-Whitney test on the coverage data. The data was organized such that the electrode data was accumulated (n = 27 for each activity mode) to represent each electrode in each activity mode. The computed p-values for the null hypothesis test are listed in the Table 4.

The analysis shows that there are statistically significant differences in the electrode coverage performance especially with standing and sitting activity modes. In this analysis null hypothesis is rejected when $p < 0.05$ and these cases are marked with bold typeface in the Table 4. The null hypothesis is rejected when there is a statistically significant difference detected between the test pairs. Therefore, in the standing and sitting activity modes peak electrodes are separable from both polymer and gold electrodes.

Table 2. Average coverage ratios and their respective standard deviations of each electrode in all activity modes combined. The maximum and minimum values are highlighted in bold typeface.

Activity	**Stand**				**Sit**				**Lie**				**Walk**			
Electrode	**Avg**	**Sd**	**Md**	**R**	**Avg**	**Sd**	**Md**	**R**	**Avg**	**Sd**	**Md**	**R**	**Avg**	**Sd**	**Md**	**R**
Peak	0.68	0.23	0.74	0.88	0.76	0.26	0.87	0.97	0.70	0.35	0.85	0.97	0.57	0.26	0.51	0.81
Polymer	0.74	**0.36**	0.93	**0.98**	0.81	0.34	0.98	0.95	0.61	0.32	0.58	0.90	**0.45**	0.17	0.44	0.62
Gold	0.93	0.13	**0.99**	0.53	**0.95**	**0.08**	**0.99**	**0.35**	0.75	0.25	0.80	0.71	0.49	0.24	0.53	0.91

Table 3. Average coverage ratios with different measurement scenarios regarding the different electrode design. The maximum and minimum values are highlighted in bold typeface.

Peak																
Activity	**Stand**				**Sit**				**Lie**				**Walk**			
	Avg	**Sd**	**Md**	**R**	**Avg**	**Sd**	**Md**	**R**	**Avg**	**Sd**	**Md**	**R**	**Avg**	**Sd**	**Md**	**R**
Dog 1	0.58	0.26	0.58	0.80	0.66	**0.35**	0.67	**0.97**	0.66	0.35	0.79	**0.97**	0.49	0.34	0.46	0.87
Dog 2	0.72	0.24	0.61	0.54	0.74	0.33	0.88	0.89	0.62	0.33	0.76	0.87	**0.42**	0.35	0.34	0.81
Dog 3	0.63	0.31	0.56	0.89	0.71	0.19	0.72	0.49	**0.85**	0.19	**0.93**	0.57	**0.42**	0.15	0.40	0.44
Polymer																
Activity	**Stand**				**Sit**				**Lie**				**Walk**			
	Avg	**Sd**	**Md**	**R**	**Avg**	**Sd**	**Md**	**R**	**Avg**	**Sd**	**Md**	**R**	**Avg**	**Sd**	**Md**	**R**
Dog 1	0.77	**0.39**	**1.00**	0.92	0.78	0.33	0.92	0.86	0.60	0.36	0.66	0.85	0.27	0.14	**0.23**	0.38
Dog 2	0.63	0.33	0.72	0.92	0.80	0.32	0.91	**0.97**	0.37	0.28	0.35	0.77	**0.23**	0.11	0.25	0.30
Dog 3	0.76	0.33	0.98	0.76	0.69	0.34	0.88	0.83	**0.86**	0.18	0.95	0.40	**0.23**	**0.07**	0.25	**0.19**
Gold																
Activity	**Stand**				**Sit**				**Lie**				**Walk**			
	Avg	**Sd**	**Md**	**R**	**Avg**	**Sd**	**Md**	**R**	**Avg**	**Sd**	**Md**	**R**	**Avg**	**Sd**	**Md**	**R**
Dog 1	0.94	0.12	**1.00**	0.39	**0.96**	0.08	**1.00**	0.25	0.85	0.24	**1.00**	0.60	0.47	**0.29**	0.37	**0.91**
Dog 2	0.83	0.25	0.94	0.77	0.92	0.09	0.95	0.24	0.64	0.24	0.73	0.72	0.31	0.13	0.39	0.32
Dog 3	0.94	0.08	0.96	0.22	0.86	0.12	0.87	0.31	0.83	0.29	0.95	0.86	**0.18**	**0.03**	**0.17**	**0.08**

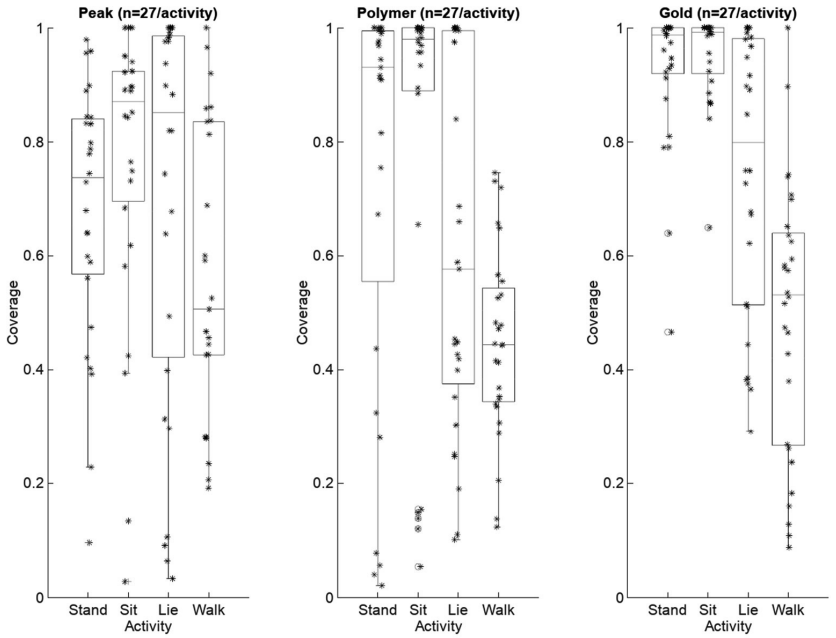

Figure 10. Combined heart rate coverage boxplots with observation points which represent a coverage ratio computed from a 60 s measurement case. The observations are marked with stars while the outliers are marked with red circles.

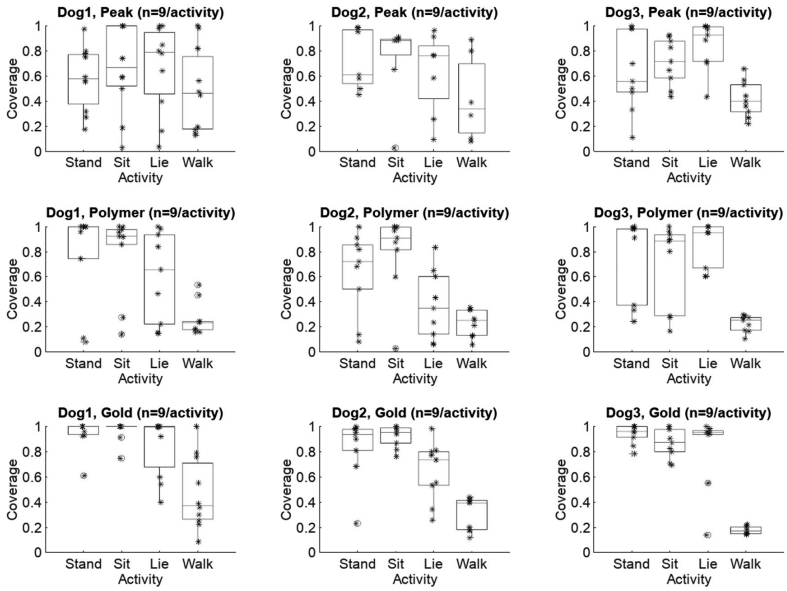

Figure 11. Boxplots of coverage ratios in different configurations with the respective observation points included in the plots. The observations are marked with stars while the outliers are marked with red circles.

Table 4. The computed *p*-values of Mann-Whitney test (n = 27) regarding the electrodes in different activity modes.

	Stand	**Sit**	**Lie**	**Walk**
Peak/Polymer	**0.027**	**0.029**	0.510	0.117
Peak/Gold	**0.000**	**0.000**	0.897	0.418
Polymer/Gold	0.053	0.252	0.184	0.354

4. Discussion

In this study, we evaluated the performance of three different dry electrodes for maintenance-free canine heart rate monitoring. The results showed that the electrodes performed differently in certain activity modes when evaluated in terms of heart rate coverage ratios. The highest coverage ratios (over 90%) were achieved with relatively stationary postures when the dogs were standing or sitting; while the lying and walking modes resulted in coverage ratios of 75% and 49% on average, respectively. The results are in line with those obtained by Brugarolas [13].

There are several factors that might have affected the performance of the electrodes. Likely, the variation in the coverage ratios may be due to the thickness and quality of the animal hair as well as the flexibility and elasticity of the electrodes. Additionally, the actual electrode length, pin density (pin-to-pin distance), and effective contact pressure may have contributed to the performance by affecting the penetration of the electrode through the hair. Contact pressure was shown prior to considerably affect the contact stability and the signal quality of dry-contact electrodes.

Beyond the different activity modes, there are other interfering factors due to the physiological properties of the tested dog breed. Further, it appears that there are also anatomical factors like the structure of the thorax (or even torso) area, which can have an effect on how the electrodes are able to retain the necessary skin contact. The dog thorax shape changes in different postures, affecting the position and the tension of the electrodes in the harness. The effect of the thorax shape change on the coverage ratio is probably the best observed in lying position, where the thorax flattens when

compared to, for example, standing position. Future long-term studies are needed to investigate and improve the dry electrode design to adapt with canine thorax shape changes.

The limitations of this study are related to the relatively small sample size of the dogs and dog breeds. Therefore, even though the results certainly reveal logical behavior of the electrode harness combination in the different activity modes, it is possible that the results of this study are not generalizable as such. Even though the data was carefully visually inspected to ensure the reliability of the R-peak detection, some part of the uncertainty in the measurement results is also possible because of the lack of a validated ECG measurement reference (e.g., Holter device). However, it is estimated that this does not contribute significantly to the measurement results reliability.

This is an ongoing work and we presented the initial results of the first trials of canine ECG electrode measurements, showing that the proposed electrodes can be used to record ECG with sufficient quality for further processing into reliable HR data. When thinking of the mass production of the electrodes studied, it can be concluded that all the tested electrode structures are relatively simple constructions and conceptually mass producible. Whereas, the spring-loaded electrodes are a multipart construction, the polymer electrode could be a single shot injection molded part. This makes the polymer electrodes potentially less expensive to produce in large production volumes.

In future studies, other measures could also be used, such as simultaneously measured cortisol in saliva and behavior, to improve the interpretation of heart rate data with regard, for example, to a dog's emotional responses and stress [19]. Also, several topics may be addressed in the future research such as improving the accuracy and the reliability of the proposed R-peak detection method by applying adaptive methods, multiple pattern recognition and dynamic thresholding.

5. Conclusions

In this work, three types of dry ECG electrodes were studied. The evaluation included studying the effect of different activity modes in the electrode evaluation. In particular, the interest was in the dry electrodes that could be conveniently used in the canine ECG measurement without the need of gel or shaving of the animal hair. To carry out the evaluation, a method for QRS complex and R-R interval from the ECG signal was constructed. The R-R interval coverage ratio as an output measure of the performance of the electrodes was evaluated to be as high as over 0.9 in favorable measurement scenarios. However, there was rather large variation in the computed coverage ratios in different cases, which may suggest that the studied electrodes may not be as suitable for all dog breeds. It was found that the metal spring-loaded type electrodes work rather satisfactorily with short-haired breeds while the longer and thick-haired dogs may be more challenging for this particular electrode type. Heart rate monitoring in more dynamic activity modes such as walking was found to be less reliable in terms of heart rate coverage.

Author Contributions: J.V. constructed most of the electrodes evaluated in the study, developed the signal processing method used in the evaluation and performed the data analysis. He also is the main responsible for writing most parts of the article and coordinated the collaborative writing process. S.S., Y.G., P.M., H.V., A.V.C., S.T., V.S., and A.V. also contributed in writing the manuscript. S.S. designed the electrode harness and data collection procedure and performed the data collection with H.T. V.J. provided the data acquisition technology and contributed to finalizing the graphical element of the manuscript. P.F. provided some of the evaluated electrodes. A.V., V.S., O.V. and J.L. supervised the research and were responsible in acquiring funding for the project. All authors have participated in reviewing and proofreading of the material.

Funding: This research was funded by Business Finland, a Finnish national research funding organization, grant numbers (1665/31/2016, 1894/31/2016, 7244/31/2016) in the context of "Buddy and the Smiths 2.0" project.

Conflicts of Interest: The authors declare no conflict of interest.

References

1. Essner, A.; Sjöström, R.; Ahlgren, E.; Lindmark, B. Validity and reliability of Polar® RS800CX heart rate monitor, measuring heart rate in dogs during standing position and at trot on a treadmill. *Physiol. Behav.* **2013**, *114*, 1–5. [CrossRef] [PubMed]

2. Mancini, C. Animal-computer interaction: A manifesto. *Interactions* **2011**, *18*, 69–73. [CrossRef]
3. Katayama, M.; Kubo, T.; Mogi, K.; Ikeda, K.; Nagasawa, M.; Kikusui, T. Heart rate variability predicts the emotional state in dogs. *Behav. Process.* **2016**, *128*, 108–112. [CrossRef] [PubMed]
4. Lawson, S.; Kirman, B.; Linehan, C.; Feltwell, T.; Hopkins, L. Problematising upstream technology through speculative design: The case of quantified cats and dogs. In Proceedings of the 33rd Annual ACM Conference on Human Factors in Computing Systems (CHI), Seoul, Korea, 18–23 April 2015; pp. 2663–2672. [CrossRef]
5. Zupan, M.; Buskas, J.; Altimiras, J.; Keeling, L.J. Assessing positive emotional states in dogs using heart rate and heart rate variability. *Physiol. Behav.* **2016**, *155*, 102–111. [CrossRef] [PubMed]
6. Wormald, D.; Lawrence, A.J.; Carter, G.; Fisher, A.D. Reduced heart rate variability in pet dogs affected by anxiety-related behaviour problems. *Physiol. Behav.* **2017**, *168*, 122–127. [CrossRef] [PubMed]
7. Gácsi, M.; Maros, K.; Sernkvist, S.; Faragó, T.; Miklósi, Á. Human analogue safe haven effect of the owner: Behavioural and heart rate response to stressful social stimuli in dogs. *PLoS ONE* **2013**, *8*, e58475. [CrossRef] [PubMed]
8. Von Borell, E.; Langbein, J.; Després, G.; Hansen, S.; Leterrier, C.; Marchant-Forde, J.; Marchant-Forde, R.; Minero, M.; Mohr, E.; Prunier, A.; et al. Heart rate variability as a measure of autonomic regulation of cardiac activity for assessing stress and welfare in farm animals—A review. *Physiol. Behav.* **2007**, *92*, 293–316. [CrossRef] [PubMed]
9. Polar Electro Oy ("Polar"), Finland. Available online: https://www.polar.com/en (accessed on 4 April 2018).
10. Essner, A.; Sjöström, R.; Ahlgren, E.; Gustås, P.; Edge-Hughes, L.; Zetterberg, L.; Hellström, K. Comparison of Polar® RS800CX heart rate monitor and electrocardiogram for measuring inter-beat intervals in healthy dogs. *Physiol. Behav.* **2015**, *138*, 247–253. [CrossRef] [PubMed]
11. Jonckheer-Sheehy, V.; Vinke, C.M.; Ortolani, A. Validation of a Polar (R) human heart rate monitor for measuring heart rate and heart rate variability in adult dogs under stationary conditions. *J. Vet. Behav. Clin. Appl. Res.* **2012**, *7*, 205–221. [CrossRef]
12. Mubanga, M.; Byberg, L.; Nowak, C.; Egenvall, A.; Magnusson, P.K.; Ingelsson, E.; Fall, T. Dog ownership and the risk of cardiovascular disease and death—A nationwide cohort study. *Sci. Rep.* **2017**, *7*, 15821. [CrossRef] [PubMed]
13. Brugarolas Brufau, R. Towards Automated Canine Training: Wearable Cyber-Physical Systems for Physiological and Behavioral Monitoring of Dogs. Ph.D. Thesis, North Carolina State University, Raleigh, NC, USA, 2016.
14. Fiedler, P.; Pedrosa, P.; Griebel, S.; Fonseca, C.; Vaz, F.; Supriyanto, E.; Zanow, F.; Haueisen, J. Novel multipin electrode cap system for dry electroencephalography. *Brain Topogr.* **2015**, 647–656. [CrossRef] [PubMed]
15. Jiapu, P.; Tompkins, W.J. A real-time QRS detection algorithm. *IEEE Trans. Biomed. Eng.* **1985**, *32*, 230–236. [CrossRef]
16. Dobbs, S.E.; Neil, M.S.; Haluk, S.O. QRS detection by template matching using real-time correlation on a microcomputer. *J. Clin. Eng.* **1984**, *9*, 197–212. [CrossRef]
17. Gao, Z.; Kong, F.; Xu, Z. Accurate and rapid QRS detection for intelligent ECG monitor. In Proceedings of the 3rd International Conference on Measuring Technology and Mechatronics Automation (ICMTMA), Shangshai, China, 6–7 January 2011. [CrossRef]
18. Kim, T.-Y.; Noh, Y.-H.; Jeong, D.-U. Template matching compression algorithm for wearable ECG measurement system based on multi wireless transmission platform. In Proceedings of the IEEE 29th International Conference on Advanced Information Networking and Applications Workshops (WAINA), Gwangiu, Korea, 24–27 March 2015. [CrossRef]
19. Beerda, B.; Schilder, M.B.; van Hooff, J.A.; de Vries, H.W.; Mol, J.A. Behavioural, saliva cortisol and heart rate responses to different types of stimuli in dogs. *Appl. Anim. Behav. Sci.* **1998**, *58*, 365–381. [CrossRef]

Dry contact electrodes performance in canine ECG

Juhani Virtanen
Joni Leivo
Antti Vehkaoja
BioMediTech Institute and Faculty of Biomedical Sciences and Engineering, Tampere University of Tampere, Finland

Sanni Somppi
Heini Törnqvist
Department of Equine and Small Animal Medicine, University of Helsinki
Helsinki, Finland

Patrique Fiedler
Institute of Biomedical Engineering and Informatics, Technische Universität Ilmenau,
Ilmenau, Germany

Heli Väätäjä
Veikko Surakka
Research Group for Emotions, Sociality, and Computing, Faculty of Communication Sciences, University of Tampere (UTA),
Tampere, Finland

ABSTRACT
Measuring the heart rate of animals is an important area of research which can be applied to numerous analyses. In this work we evaluate the performance of two dry contact electrocardiogram (ECG) electrode structures for monitoring the heart rate of domestic pets. The aim was to improve the operation of previously evaluated electrodes with some modifications. First, the thirty-pins of a previously studied polymer electrode with a silver/silver chloride (Ag/AgCl) coating were reduced to 12. Second, a 12-pin gold-plated metal electrode was coated with poly (3,4 - ethylenedioxythiophene) polystyrene sulfonate (PEDOT:PSS). These electrodes were attached to a specifically designed measurement harness and the performance of the electrodes was evaluated in terms of heartbeat detection coverage. The heart rate coverage was measured during four different behaviors: standing, sitting, lying, and walking (N=27/activity). The results were, in general, comparable to the previously reported performance but having fewer pins on a polymer electrode seemed to cause more variation in the coverage values. However, when measures such as the median value of the coverages are considered, there was no obvious difference, especially when the coverage values were observed altogether. Thus, new electrode solutions are worthy of further research.

Author Keywords
Canine; Electrocardiogram; Dry Electrode

ACM Classification Keywords
[Hardware; Communication hardware, interfaces and storage; Sensors and actuators];

ACI18, December 4–6, 2018, Atlanta, GA, USA

ACM ISBN 978-1-4503-6219-1/18/12.
https://doi.org/10.1145/3295598.3295609

INTRODUCTION

Heart rate monitoring is increasingly popular with pets; the motivation being to obtain information about the physical and emotional well-being of the animal of which pet-owners are always interested in [1,4]. There are some currently-available commercial devices for monitoring the heart rate of animals in their everyday lives. However, all such devices are limited by the fact that the information is not always reliable, or if the devices are able to differentiate and extract reliable heart rate information, the coverage of the readings is low so no heart rate is usually obtained during movement. Furthermore, there is no way to perform electrocardiogram (ECG) monitoring with the currently available devices. There are various reasons for this, one of the most obvious ones being that the available devices often require wet-gel patch electrodes which entail shaving the animal's fur to get a sufficiently high-quality electrical contact with the skin. Shaving the skin and applying conductive gel for the everyday monitoring of a pet has always been problematic, so the need for low-maintenance electrodes is clear. One possible approach to this problem is to use dry electrodes. Although promising results have been reported for both human and animal applications [2,5,6], there are challenges in measuring ECG with dry electrodes. These are mainly associated with disturbances caused by motion artefacts, often resulting in the total loss of electrical contact between the electrode and the skin. These phenomena are particularly apparent in so-called dynamic activity modes, such as walking of the dog.

The performance of our ECG electrodes was assessed using a previously published methodology [6] in which the performance of three dry ECG electrodes was evaluated in terms of ECG coverage ratio. The coverage ratio was defined as the ratio between the time when the R- peaks were successfully recovered against the total testing time. The coverage ratio value '1' represents 100% recovery of the R-peaks and the value '0' represents 0% R- peak detection. [6]. Thus, the methodology and evaluation criteria applied in this study are the same as the ones presented in the previous study [6]. Both of the electrodes evaluated in this study are modifications or improved versions of the ones presented in

the previous study. Our aim was to see whether reducing the number of pins on the polymer electrode, or coating the metal pin electrode with a PEDOT:PSS would improve the coverage rate.

MATERIALS AND METHODS

Electrodes

Two types of electrode were constructed. The first one was modified from the above-mentioned Ag/AgCl-coated polymer pin electrode manufactured by the University of Ilmenau, Germany. The electrode pin distribution was made less dense by using fewer pins. The hypothesis here was to improve the performance of the electrode by improving its penetration through the animal's fur and simultaneously increasing the applied surface pressure. The second electrode was a modification of the gold-plated metal pin electrode used in the previous study. This electrode was modified by giving it a PEDOT:PSS coating to enhance the electrochemical performance at the electrode/skin interface.

The polymer electrode

The silver/silver chloride- (Ag/AgCl)-coated polymer electrode [3] was prepared for the measurements by removing 60 % of the pins in the original design. Therefore, 18 pins from of the original 30-pin electrode were cut out, giving us a 12-pin polymer electrode for the tests. The trick was to remove the pins so that the remaining pins would form as evenly distributed a pattern as possible. There were two reasons for this. One was to observe the effect of having fewer pins, and the other was to observe the effect of the higher surface pressure of the electrode in the skin contact. The modified electrode and the electrode used in the silicone rubber casting are presented in Figures 1. a) and 2. a) respectively. This electrode is henceforth referred to as the Polymer12 electrode.

Spring-loaded electrode with a PEDOT:PSS coating

The PEDOT:PSS electrode was prepared by dipping the tips of a spring-loaded gold-plated electrode into a 2.5 wt. % PEDOT:PSS/deionised water solution for 1 h in order to enhance the electrochemical interface at the skin-electrode interface. The mechanical design of this particular electrode was identical to the one studied previously in [6]. Both the electrode itself, and the electrode embedded in the silicone rubber casting are shown in Figures 1. b) and 2. b) respectively. This electrode is henceforth referred to as the PEDOT -electrode.

The fixtures for the electrodes

The silicone rubber fixtures were prepared by molding a lump of silicone rubber into a 3D –printed mold. The fixtures were used to house the electrodes and make it easier to attach the electrode-fixture to the harness. The electrodes and fixtures were joined together using a second silicone rubber molding in which the fixtures became integral electrode-fixture structures. These fixtures were then attached to a harness, which was put on the test animal. The way the silicone rubber fixtures were made is described in detail in [6].

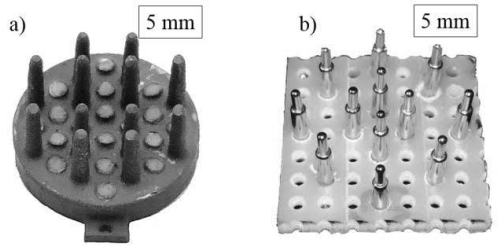

Figure 1. Electrodes a) Reduced pin count polymer (Polymer12) electrode b) PEDOT:PSS coated (PEDOT).electrode

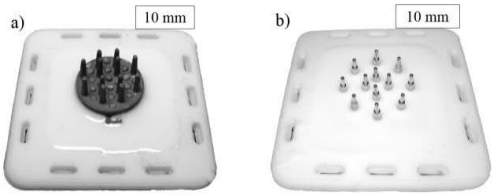

Figure 2. Electrodes in the silicone cast housings a) Reduced pin count polymer (Polymer12) electrode b) PEDOT:PSS coated (PEDOT) electrode in the housings.

The Harness

The electrode fixtures, comprising a total of four electrode fixtures, were attached to the harness in order to fix the locations of the measurements on the dog. This is illustrated in Figure 3, where the dog, a Golden retriever, is wearing the harness containing the electrode fixtures. The electrode locations in the harness are marked with circles.

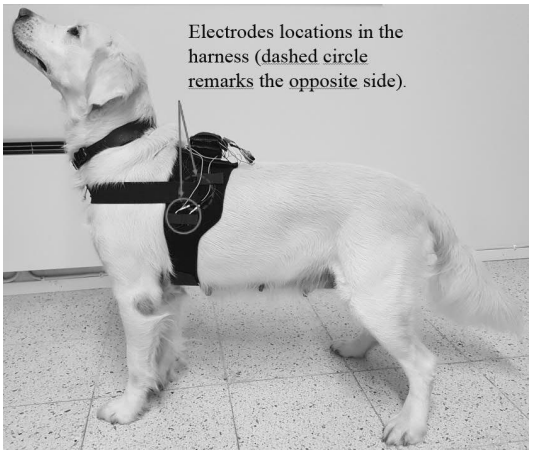

Figure 3. The dog, a Golden retriever, and harness with electrode locations. The solid circle represents the left-hand electrode while the dashed circle is the right-hand electrode.

Testing procedure

All the tests and measurements were conducted by the University of Helsinki according to statement 2/2018 of the Ethical Committee for the Use of Animals in Experiments. The three dogs that were chosen to participate in the measurement sessions, two female Beauce Shepherds and one male Hovawart, were the same dogs that had been used in the previous study [6]. The testing procedure involved four activity modes: standing, sitting, lying and walking. Each of the activities were measured for one minute making the length of each 'testing block' 4 minutes. The blocks were then repeated three times, making a total of 12 minutes for each test session. The test sessions were repeated three times, and the harness was removed between each session. All of the electrodes were tested in the same way, giving a total number of one-minute activities (N=9) in each configuration. The total recording time in the test was therefore 216 minutes, representing 216 1-minute activity-mode samples.

The measurement electronics

A custom-made physiological measuring apparatus, the SpiritCor9D monitoring device, was used to record the ECG biopotential data at a sampling frequency of 500 Hz. The measurement device was exactly the same as the one used in the previous work except that it had a higher sampling frequency. This was taken into account later in the data-processing stage to ensure comparability with the previous measurements. In order to collect the measurement data, the electrodes in the harness were physically connected to the measurement device by wire. The recorded ECG data was later processed and analyzed with a standard desktop home computer .

Data analysis

A digital Butterworth band pass filter (2-30 Hz) was applied to the raw ECG measurement data. This filtering was done to remove power line noise, baseline wander and motion artefacts from the measured ECG signal. After this filtering, a pattern-matching algorithm was applied to the filtered signal which matched a predefined ECG template, and could therefore extract the R-peaks. The coverage ratios were then computed from this R-peak detection data. This procedure is described in more detail in [6].

RESULTS

The measurement results are shown in Tables 1 to 3 and visualized in the box plots in Figures 4 and 5. The tables present the results in statistical terms of average, mean, range and standard deviation in both their consolidated forms (Table 1) and broken down into the individual measurements taken from each dog (Tables 2-3). Moreover, the coverage of each activity mode is also listed separately in the tables. Figure 4 shows the total coverage boxplots of the two electrodes, while Figure 5 shows the boxplots broken down so that they represent the measurements of each dog separately. The average, the standard deviation, the median and the range values of the overall coverage varied between 0.15-0.81, 0.08-0.37, 0.14-0.80 and 0.21-0.34 respectively. These values are shown in Table 1. In the individual test case break-downs, the coverage average, standard deviation, median and range values with the Polymer12 and the PEDOT are 0.29-0.83, 0.15-0.34, 0.25-0.94, 0.39-0.97 (Table 2); 0.13-0.96, 0.08-0.37, 0.03-0.99, 0.21-0.97 (Table 3.) for the two electrodes respectively.

Overall	Stand				Sit				Lie				Walk			
	Avg	Sd	Md	R	Avg	Sd	Md	R	Avg	Sd	Md	R	Avg	Sd	Md	R
Polymer12	0.78	0.19	0.72	0.28	0.69	0.30	0.41	0.24	0.81	0.12	0.77	0.34	0.15	0.08	0.14	0.21
PEDOT	0.78	0.21	0.80	0.25	0.45	0.37	0.47	0.30	0.81	0.12	0.77	0.34	0.15	0.08	0.14	0.21

Table 1. Overall coverages obtained with both electrodes. Avg = average, Sd = standard deviation, Md = median, R = range

Polymer12	Stand				Sit				Lie				Walk			
	Avg	Sd	Md	R	Avg	Sd	Md	R	Avg	Sd	Md	R	Avg	Sd	Md	R
Dog1	0.78	0.20	0.83	0.63	0.65	0.34	0.71	0.97	0.83	0.21	0.94	0.53	0.50	0.26	0.59	0.66
Dog2	0.83	0.15	0.83	0.39	0.82	0.16	0.83	0.41	0.60	0.34	0.57	0.93	0.43	0.27	0.50	0.66
Dog3	0.73	0.20	0.69	0.60	0.69	0.30	0.82	0.80	0.63	0.32	0.69	0.83	0.29	0.17	0.25	0.46

Table 2. Individual coverages of Polymer12 electrode. Avg = average, Sd = standard deviation, Md = median, R = range

PEDOT	Stand				Sit				Lie				Walk			
	Avg	Sd	Md	R	Avg	Sd	Md	R	Avg	Sd	Md	R	Avg	Sd	Md	R
Dog1	0.76	0.17	0.69	0.41	0.68	0.37	0.76	0.97	0.42	0.36	0.47	0.92	0.50	0.26	0.59	0.65
Dog2	0.90	0.19	0.99	0.59	0.96	0.08	0.99	0.24	0.13	0.18	0.03	0.44	0.75	0.12	0.79	0.39
Dog3	0.70	0.23	0.79	0.60	0.76	0.15	0.77	0.48	0.81	0.12	0.77	0.34	0.15	0.08	0.14	0.21

Table 3. Individual coverages of PEDOT coated electrode. Avg = average, Sd = standard deviation, Md = median, R = range

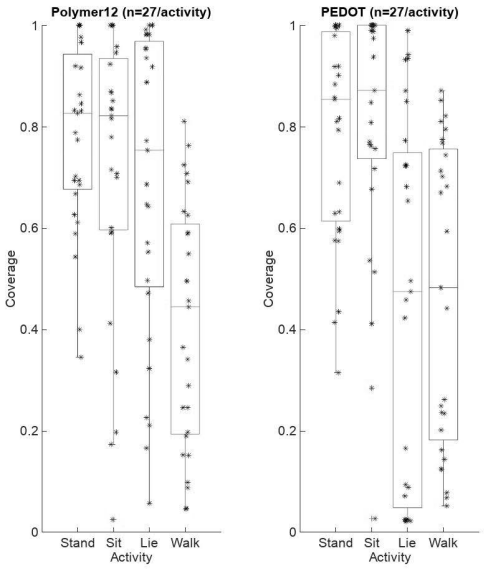

Figure 4. Overall coverage boxplots of the two electrodes in different activities. A star represents an individual coverage observation.

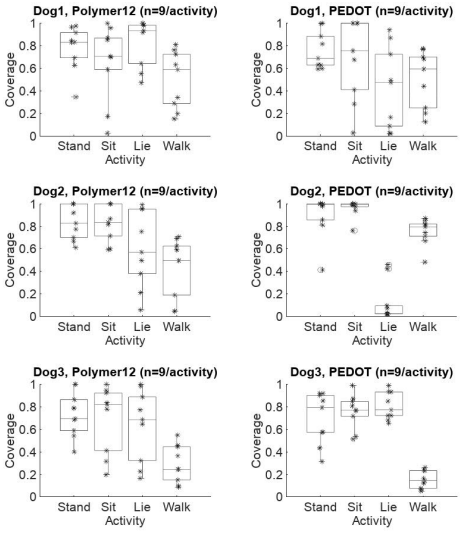

Figure 5. Coverages boxplots of the different electrodes for each measured dog. A star represents an individual coverage observation while a red circle represents an outlier.

CONCLUSIONS

The results of this study show that the canine heart rate coverage measurements are similar to those reported previously in [6]. As expected, the dry electrodes tend to perform more reliably in stationary postures such as stand and sit. The sitting position is particularly favorable and consistently yields high coverage ratios. As the study was not particularly extensive in that the measurement data was only collected from three dogs, the results should be interpreted as indicative, rather than conclusive. However, the results do indicate that this topic is worthy of further study.

The measurement results give a deeper insight into the effect of having fewer pins on a cast polymer electrode as this seems to cause greater variation in the coverage values. This conclusion is supported by observing the individual electrode canine test-case results. However, if statistical measures such as the median value of the computed coverages are considered, the difference is not particularly great, especially when the coverage values are taken as a whole. Another conclusion is that because the results from the PEDOT:PSS coated electrode are very similar to those from the plain gold-plated electrodes reported earlier, there is no support for the hypothesis that a PEDOT:PSS coating improves the skin-electrode interface. Nevertheless, there still remains the fact that the coverage values are lower than expected in the lying posture. This may have been caused by a change in the electrode-harness attachment during the test as is indicated in one particular test-case (Dog2/PEDOT). Additionally, in this test-case the coverages for walking, standing and sitting are high. This anomaly also motivates further study of this particular phenomenon as dynamic activity modes such as walking have previously been reported as being more challenging. Another possible reason for the differences in the results of this study compared to the previous one [6] may be variations in the testing procedure. Although the tests followed the same protocol and the dogs and testers were the same, which should enable a direct comparison of the results, it is difficult to standardize the behavior of the dogs in absolute terms, particularly when they are walking.

Although the durability of the devices and the effects of long-term wear were not specifically studied, it seems safe to assume that the thin coatings on the electrodes will have a limited lifetime, especially in high-activity operation. Therefore. if these kinds of coatings were to be used for the consumer market, further studies would be required to investigate the long-term durability of the electrodes, which could perhaps be optimized via the coatings and their manufacturing processes. Further studies are also needed to determine how the wear of the electrode influences the quality of the coverage ratio.

Another important aspect of wearable electrodes not covered in this study is the comfort of the electrodes, especially for long-term use. Although the authors did not notice any abnormal behavior from the dogs when they (the dogs) were

wearing the harness, and the comfort of the electrodes was also declared not to be too irritating by the authors, it is difficult to know what the animals felt about wearing the harness. Despite the importance of this topic, there are currently no objective methods for measuring the degree of comfort or discomfort felt by animal test-subjects.

ACKNOWLEDGMENTS

This research was funded by Business Finland, a Finnish national research funding organization, grant numbers 1665/31/2016, 1894/31/2016, 7244/31/2016 in the context of "Buddy and the Smiths 2.0" project.

REFERENCES

1. Abbott, Jonathan A. "Heart rate and heart rate variability of healthy cats in home and hospital environments." *Journal of feline medicine and surgery* 7.3 (2005): 195-202.
2. Brugarolas, Rita, et al. "Wearable heart rate sensor systems for wireless canine health monitoring." *IEEE Sensors Journal* 16.10 (2016): 3454-3464
3. Fiedler, Patrique, et al. "Contact Pressure and Flexibility of Multipin Dry EEG Electrodes." *IEEE Transactions on Neural Systems and Rehabilitation Engineering* (2018).
4. Katayama, Maki, et al. "Heart rate variability predicts the emotional state in dogs." *Behavioural processes* 128 (2016): 108-112.
5. Salvo, Pietro, et al. "A 3D printed dry electrode for ECG/EEG recording." *Sensors and Actuators A: Physical* 174 (2012): 96-102.
6. Virtanen, Juhani, et al. "Evaluation of dry electrodes in canine heart rate monitoring." *Sensors (Basel, Switzerland)* 18.6 (2018).

Piezoelectric dual axis cantilever force measurement probe

Juhani Virtanen, Arno Pammo, Antti Vehkaoja, *Member IEEE*, and Sampo Tuukkanen
Faculty of Medicine and Health Technology, Tampere University (TAU) Tampere, Finland

Abstract—**A piezoelectric cantilever force sensor consisting of a mechanical cantilever probe, an analog amplifier and an embedded digital signal processing unit is presented. The sensor is constructed from a lead zirconate titanate (PZT) piezo disc, which was cut into four segments and a 33-mm-long metal probe attached to it perpendicularly to the piezo disc plane. The signal of the piezoelectric elements was amplified with a four channel operational amplifier circuit having voltage gain of 10 (20 dB) in each channel and input resistance of 50 MΩ. The digital signal processing was implemented on an Arduino Due -based hardware. Signal pre-processing block consists of three cascaded digital infinite impulse response (IIR) filters were composed: A DC-blocking filter, a notch filter and a low pass filter. Additionally, a moving average filter was implemented to further enhance the system tolerance to power line interference and to reduce the sampling rate to 50 Hz. Finally, a LabVIEW software is used to provide an interface for the Arduino Due. The calibration of the system was carried out with a texture analyzer and it was capable of sensing biaxial forces in the range of 2 millinewton with a RMS error of less than 60 micro Newton and hysteresis in the order of 0.25 millinewton or 12.5% of the full scale reading. Cross talk ratio between axes was 25.3 or 28.0 in dB. The applicable force measurement frequency range was 0.5 – 10 Hz.**

Keywords—Force measurement, dual axis, piezoelectric

I. Introduction

During recent two decades, there has been an increasing trend towards miniaturization and micromanipulation in many fields, such as biomedical engineering, robotics, industrial automation and materials sciences. In the miniaturized systems, force measurement becomes critical not only due to the small forces to be measured but also because the miniaturized equipment are easily damaged [1]. The force sensing solutions range from resonant tactile force sensors for robotic touch sensing, in which the change in the resonant frequency of piezoelectric force sensor changes as a function of applied force [2], to screen printed thick film piezoelectric slip sensor, which is used to enhance the functionality of a prosthetic hand by decreasing the complexity of the touch sensing system [3]. Along with a piezoelectric sensor principle, piezoresistive sensing can be applied in similar sensing applications, except the piezoelectric sensor cannot detect static forces. For example, a screen printed piezoresistive cantilever sensor proposed by Lakhmi *et al*. has shown capability to measure static forces in micronewton range [4].

In addition to varying physical operation principle, different approaches, such as utilizing piezoelectric foils or membranes, are suitable for force sensing. For example, polyvinylidene fluoride (PVDF) based piezoelectric membrane sensors have been proposed for single cell biological force measurements [5] or in defining mechanical properties such as shear strength of paper fiber [6]. Further, sensors processed on a silicon wafer are commonly utilized in micro electromechanical systems (MEMS) providing capability down to nanonewton range force sensing [7]. More advanced three-axis silicon membrane based piezoresistive force sensor has been reported to measure forces below micronewton range [8].

However, it should be noted that the low force detection capability in millinewton or smaller scale is not limited solely to piezoelectric or piezoresistive properties. For example, strain gauge-based resistive, capacitive, piezo magnetic, optical, vision-based, and electroactive force sensors have been developed [1]. Common challenge to all low force sensing techniques relying on a linear elastic material property is tailoring the elastic properties of the measurement system such that the actual force measurement dominantly takes place instead of only a displacement or movement observation [1].

Sophisticated low force measurement and manipulation techniques provide interesting opportunities to study and quantify behavior of small scale biological organisms. Recently, there has been increasing interest towards *in vitro* cardiac contraction force measurement for engineered tissues. Regarding the utilization of piezoresistive sensing principle, Sasaki *et al*. proposed a force measurement approach based on cell construct cultivation on a specific fibrin sheet "cell sheet engineering" [9] and Wang *et al*. reported utilization of an elastic sheet with carbon nanotubes (CNT) [10]. Linder *et al*. demonstrated pressure based force sensing by using an elastic membrane with a gas chamber and a pressure sensor "cell drum technology" [11]. Mannhardt *et al*. reported a force measurement based on optical analysis of a cell structure cultured between two adjacent bending beams [12]. There are several reports about utilization of atomic force microscope (AFM) cantilever for a direct contraction force measurement [13-15]. Similarly, Gaitas *et al*. reported a direct cardiomyocyte contractile force measurement based on piezoresistive sensor embedded on a polyimide micro cantilever arrangement [16].

In our previous work, we have developed a customized single axis cantilever force measurement technique, which is composed of one sensing element [17]. Here, we present a dual axis approach which is based on piezoelectric four-element sensor attached to a metallic cantilever capable of sensing forces in two directions. In the previous work, we are limited to measurement of force in only one direction, which places a challenge on proper alignment of the measurement

probe. In the engineered tissues the tissue structures and cells are often randomly oriented requiring the contraction force measurement orientate accordingly. In this application it would be beneficial to have at least two axis force sensing capability. The dual axis force measurement capability enables positioning of the measurement probe tip to an area of interest without having to accurately align it with contraction direction. Thus making the force measurement incur better repeatability. This type of biomeasurement can be used to study for example toxicity of potential drugs before moving to clinical phase in the drug development. From the ethical point of view, the amount of animal testing could be reduced with this approach.

Open source hardware development platform such as Arduino [18-20], provide cost effective and versatile alternative for implementation of various embedded electronic measurement systems with low costs. For example a range of customizable biomeasurement instrumentation can be built onto these kind of platforms reducing a black box problem where the operation of the measurement devices is not completely understood by the developer.

In this work, a dual axis force measurement system was developed using Arduino Due open source platform and in-house developed piezoelectric cantilever sensor. Our interest was to study the capabilities of this customizable measurement platform with added functionalities such as embedded digital signal processing and to study the performance of the piezoelectric dual axis cantilever force sensor performance.

II. Materials and Methods

A piezoelectric cantilever based force measurement system, consisting of a piezoelectric dual axis mechanical cantilever probe, an analog voltage amplifier and a digital signal processing unit, was developed for applications requiring sub-mN force measurement. A LabVIEW (National Instruments corporation, Austin, USA) user interface program was developed for further processing, visualization and storing of the measurement data.

A. The dual axis force measurement probe sensor

The cantilever probe arrangement was constructed from a 15 mm diameter lead zirconate titanate (PZT) piezo disc that was first cut into four symmetric segments. The cutting was done with a rotary diamond cutting disc. The sensing segments are labeled from E1 to E4. The schematic sensor arrangement is illustrated in the in Fig. 1. Further a 33 mm long metal cantilever probe pointing at *z*-direction was attached in the middle of the segment apexes perpendicularly to the piezo disc plane. The attachment was done by soldering the probe to the piezo disc. Being significantly thicker than the piezo disc, the joint was considered to be much firmer than the piezo disc, thus not affecting the force measurement results. Further, the segments were fixed to a printed wiring board (PWB) frame in *xy*-plane from the opposite sides to the apexes. When a radial force is applied to the cantilever tip, stress is induced to the piezoelectric elements. This results in charge separation in the piezo elements which then can be measured as voltage output using the voltage amplifier. Depending on the force direction, the stress applied to the different piezo elements changes, resulting to a separation of forces in *x* and *y* -directions. To some extent, this kind of construction is also capable of sensing *z*-directional forces but this was not in the interest of this study. The working principle of the force sensor is similar to what has been presented earlier in [17, 21-23].

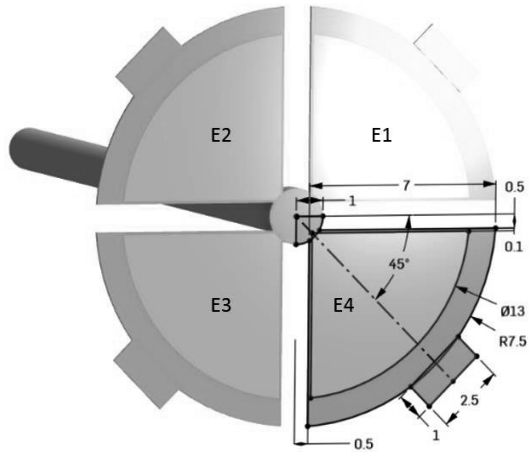

Fig. 1. The piezoelectric cantilever sensor probe. All measures are given in millimeters. (Figure adapted from reference: [18]).

The sensor functionality was first simulated with a finite element method (FEM) (COMSOL Multiphysics, Stockholm, Sweden). This simulation involved a linear elastic physics model simulation combined with a piezoelectric model. This FEM model was used to compute the displacement and electrical field at 2 mN static load at the probe tip to represent the maximum output amplitude in an electrically unloaded situation. This information was then used to compute the spring constant and sensitivity estimates for the sensor. The sensitivities and spring constants were computed in both 0-degree and 45-degree orientation. The potential field in 0-degree results are shown in Fig. 2a and the electric potential field in 45-degree orientation in Fig. 2b. It was also confirmed with FEM simulation that *z*-axis load does only have a negligible effect (less than 0.01 %) on the *xy*-plane force measurement results.

The actual *x* and *y* force components are computed as a linear combination of the sensor element signals. This is done is such way that the components divided by the axis of interest are first weighted with opposing signs and then integrated. The resulting formulas are presented in (1) for *x*-axis and (2) for the *y*-axis.

$$x = (E1+E4) - (E2+E3) \quad (1)$$

$$y = (E1+E2) - (E3+E4) \quad (2)$$

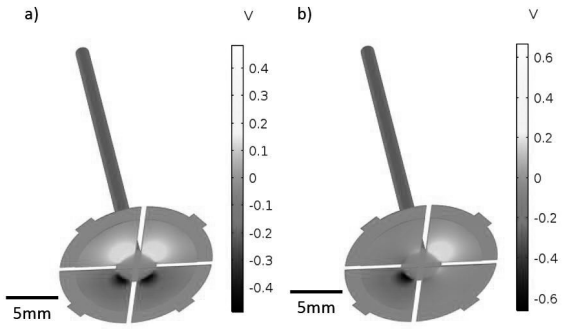

Fig. 2. Electric potential field for 2 mN load in a) 0 degrees orientation b) 45 degrees orientation.

A frequency response simulation was also carried out to obtain parameters for a second order mechanical resonator model. The natural frequency and the damping factor were obtained from the frequency response simulation. The usable frequency band was initially computed from the numerical model and later confirmed with actual impulse response measurements. The analytical model for cantilever transfer function is shown in Equation 3. It represents a second order mechanical system response characterized with a natural frequency (ω_0) and a damping factor (ζ). From the simulation a ω_0 of 1330 rad/s (212 Hz) and a zeta of 0.37 was obtained. Thus, it was concluded that the resonance of the cantilever system is outside of the desired measurement frequency band of approximately from 0.5 to 10 Hz.

$$H(s) = \frac{{\omega_0}^2}{s^2 + 2\zeta\omega_0 s + {\omega_0}^2} \qquad (3)$$

B. The measurement hardware

A four channel analog voltage amplifier circuit was designed to interface the force sensor segments. This amplifier output was sampled with 12-bit analog to digital converter (ADC) of the Arduino board. Each channel of the analog front-end consisted of a voltage amplifier with voltage gain of 20 dB (10x). The input resistance of the amplifier was 50 MΩ. This input was driven directly by the piezo disc transducer having 2.5 nF capacitance. This arrangement described in Fig. 3 resulted a high pass behavior of the piezo sensor with pole frequency of 1.27 Hz.

The amplifier circuit was implemented with AD8691 (Analog Devices incorporated, Norwood, USA) precision operational amplifiers. Moreover, the amplifier had a first order low pass filter with a cut off frequency of 40 Hz to reduce the overall noise and prevent aliasing. An analytical model of the transfer function of the amplifier was constructed and this was later used to analyze the total behavior along with the other transfer functions. The values of the discrete components of the amplifier are listed in Table I.

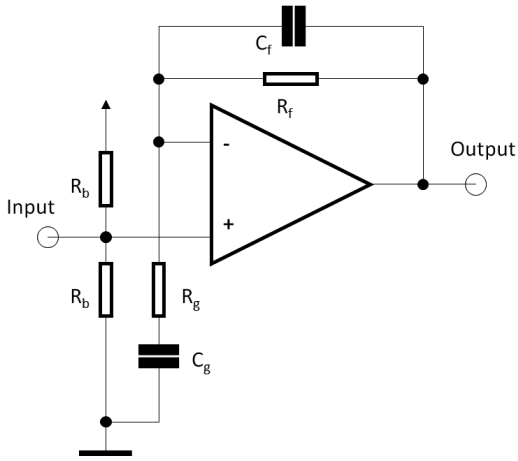

Fig. 3. Front-end amplifier schematic.

TABLE I. Component values of the front-end amplifier.

Component	R_b	R_g	C_g	R_f	C_f
Value	100 MΩ	100 kΩ	10 µF	0.91 MΩ	4.7 nF

The transfer function of the amplifier is shown in Equation 4.

$$A(s) = \frac{R_f}{(R_f C_f s + 1)} \cdot \frac{C_g s}{(R_g C_g s + 1)} \qquad (4)$$

A photograph of the PWB of the sensor-amplifier is shown in Fig. 4. The top side sensor PWB with the measurement probe attached to is shown in Fig. 4a, and the bottom side in Fig. 4b.

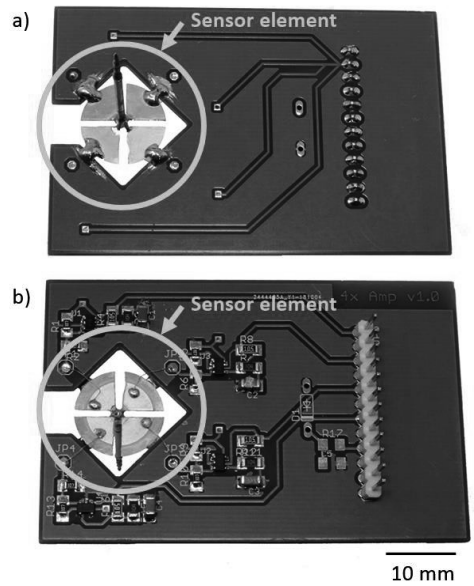

Fig. 4. Photographs of the sensor PWB from a) bottom (sensor) side and b) top (electronics) side.

C. Digital signal processing

The signal processing was done using an Arduino Due as the hardware platform. It consists of an Atmel SAM3x8E (Microchip corporation, Chandler, USA) microcontroller having a 32-bit ARM processor architecture operating at 84 MHz clock frequency with a floating point processing unit. In addition, it contains an integrated multiplexed 10 channel 12-bit ADC unit. Moreover, the platform contains a native Universal Serial Bus (USB) communication unit integrated on the chip. The controller and its peripherals are described in more detail in the microcontroller data sheet [24].

The analog four channel signal was first sampled with the Arduino Due with sampling frequency of 3 kHz. This was chosen such that the later the averaging filter would have zeros at 50 Hz and at its harmonic frequencies. This was to remove the most prominent 50 Hz power line interference from the measured signal. An averaging filter was used to reduce the sampling rate to 50 Hz, which was assumed adequate for the proposed application. The reason to down sample the signal was to prepare the measurement system to be able to operate in a large sample quantity measurement simultaneously. For example, a standard cell cultivation well plate may have multiple wells reaching up to several hundred of them, increasing the data flow to the recording and analyzing systems accordingly. The signal was first filtered with three types of digital infinite impulse response (IIR) filters. Initially three IIR filters were composed and later they were cascaded to form a 7th order IIR filter which was then embedded into the Arduino system [25]. The overall transfer function of the IIR filter is shown in (5) while the IIR filter coefficients are shown in Table II.

$$H(z) = \frac{\sum b_n z^{-n}}{\sum a_n z^{-n}} \; ; \; n = [0...7] \qquad (5)$$

TABLE II. 7th order IIR filter coefficients.

Order	A	B
z^{-0}	1	4.3549E-07
z^{-1}	-6.83482	4.4026E-07
z^{-2}	20.03316	-1.2922E-06
z^{-3}	-32.6413	-1.2969E-06
z^{-4}	31.93014	1.2969E-06
z^{-5}	-18.75189	1.2922E-06
z^{-6}	6.12171	-4.4026E-07
z^{-7}	-0.85699	-4.3549E-07

After the IIR filtering, block averaging was applied batch wise to further remove noise and down sample the signal. The other advantage of this procedure is that as the noise in the ADC input is assumed Gaussian distributed, the resolution of the ADC will be increased proportional to the square root of the average length. In this case, the increase is approximately three bits [26, 27]. The amplitude and the phase responses of the combined filter transfer function are shown in Fig. 5.

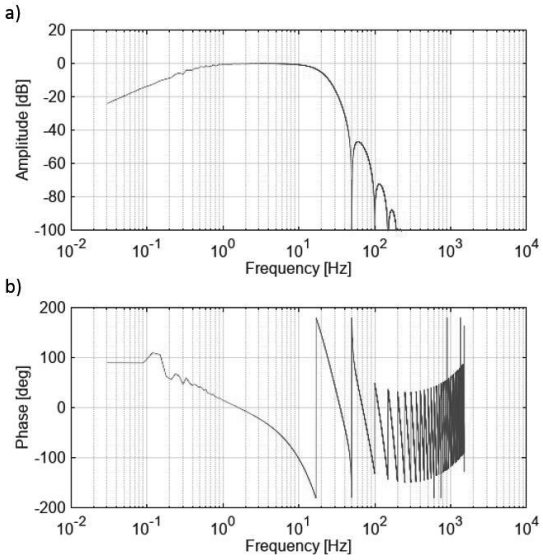

Fig. 5. The Amplitude and phase response of the cascaded filter (figures adapted from reference [18]).

III. RESULTS AND DISCUSSION

A. Cantilever sensor system impulse response

The simulation was carried out in frequency domain and the actual measurement in time domain. The time domain impulse response was obtained by creating an impulse-like excitation to the tip of the sensor by tapping it in *xy* -plane direction. The frequency response was then obtained from the time domain measurement of the impulse response by taking a discrete Fourier transform. The sensitivity measurement was then used to match the absolute level of the impulse response. This impulse response data was then further analyzed by computing a discrete Fourier transform (DFT) to obtain frequency response of the cantilever probe. The time domain impulse response is illustrated in Fig. 6a.

Comparison of the measured and simulated amplitude responses are shown in Fig. 6b. Fig. 6 shows good correlation between the simulated and measured amplitude response. In addition, it shows that the frequency range is suitable for low frequency force measurements. Even though the piezoelectric force measurement principle is dynamic in its nature, the force measurement capabilities suit the proposed application. The applicable frequency range of 0.6 – 3.0 Hz has been proposed earlier for cardiac cell contraction force measurement [5].

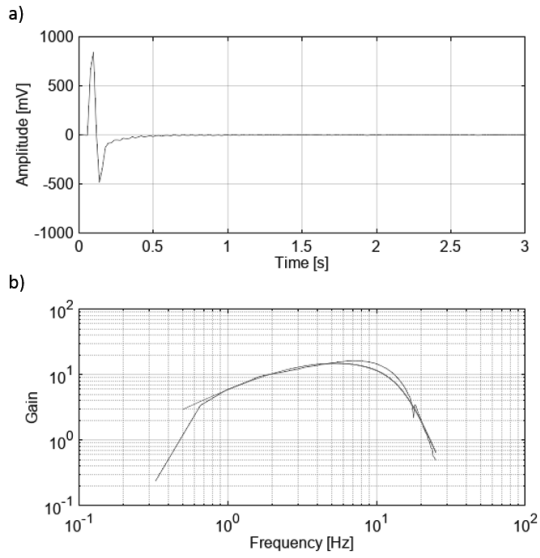

Fig. 6. a) Measured impulse response in time domain. b) Measured (blue) and analytical (red) frequency response of the cantilever sensor system.

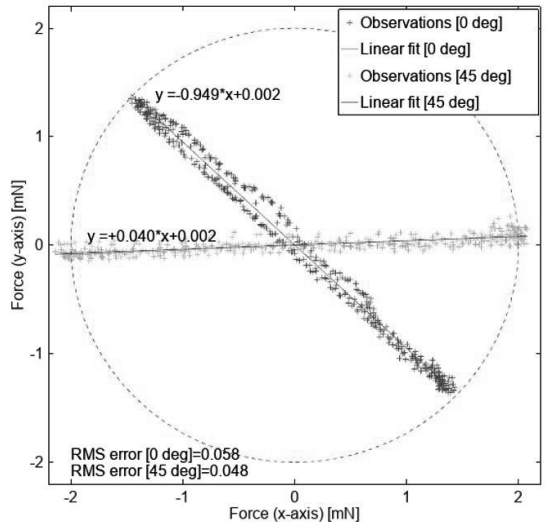

Fig. 7. Calibration results with the measurement observations and their corresponding linear fitted lines. Red circle represents a constant 2 mN load.

B. Calibration and sensitivity measurements

The calibration of the force measurement probe as well as the measurement repeatability analysis was carried out using a TA.XTPlus (Stable Micro Systems Ltd, Surrey, United Kingdom) texture analyzer. The applied calibration method is described in more detail in a previous paper [21]. The procedure consisted of two ±10 µm linear 10 cycle sinusoidal displacement sweeps in *xy*-plane at 0 degrees (*x*-axis direction) and 45 degrees rotated orientation with respect to the *x*-axis. The 10 µm displacement corresponded approximately 2 mN force amplitude. From the calibration data the sensor system sensitivity and the spring constants were computed. The analytical and the measured sensitivity values are listed in Table III. Furthermore, theoretical resolution of the sensor was computed based on the analog-to-digital conversion, which yielded theoretical resolutions of 0.11 µN and 0.12 µN in 0 degrees and 45 degrees orientation, respectively.

The measurement results are presented in Fig. 7. Due to the nature of the in-house assembled prototype sensor there was an orientation error in both of the axes of the piezo sensor elements, which caused systematic error to the sensor readings. Also, the non-optimized alignment of the sensor into 0 and 45 degrees angle with the excitation direction caused some inevitable error to the calibration measurement. However, when the repeatability of the measurement system was studied, it was assumed that this error can be corrected and therefore the repeatability figures were computed relative to the linear fitted axes, which represent in this case the calibration-corrected force excitation directions. The amber and blue scatter plots show the measurement observations. The repeatability computations resulted RMS error of 48 µN in 0 degrees (represented as amber crosses in Fig. 7) and 58 µN in 45 degrees orientation (blue crosses). This corresponds to hysteresis of 0.18 mN and 0.25 mN or 8.75 % and 12.5 % in 0 degrees and 45 degrees orientation respectively. A constant force circle (red) is also drawn in the Fig. 7 to display 2 mN force range.

The sensor output in *x* and *y* -directions were computed in linear combination of all sensor element outputs. The total axis output signals were calculated by adding the potentials on one side (segments E1 and E4 described in Fig. 1 for *x*-signal and segments E1 and E2 described in Fig. 1 for *y*-signal) separated by the axis in interest and subtracting the potentials (segments E1 and E2 in Fig. 1 for *x*-signal and segments E3 and E4 in Fig. 1 for *y*-signal) on the opposing side. There was no axis correlation term used in this calculus. When comparing the maximum deviation in both 0 and 45 degree orientations this shows rather consisted readings suggesting that the sensor design has only small mechanical cross correlation component between *x* and *y* -axes. This result confirmed the sensitivity estimation that was computed in FEM simulation. The crosstalk component is visualized in Fig. 8b. There the excitation has been performed in 45 degree angle. Based on the simulations, the other component should theoretically have been cancelled totally, as the sensor signals should have been equal but opposite. However, due to non-optimized hand-manufactured prototype sensor, this cross correlation component is visible in the measured data presented in Fig. 8b.

In Fig. 8a, combined sensor element output signals are shown when the sensor load is applied at 0 degree angle. There sensor signal component in *x* and *y* -direction are showing similar sized amplitudes in opposite phases. In Fig. 8b, the signals are combined when the load is applied in 45 degree orientation. There the *x* component is much larger than the *y* component. Based on the FEM simulation the individual sensor output components S1 and S3 should cancel each other in this configuration and yield a *y*- component with a zero value. However, with the sensor prototype, this component is clearly measurable and it can be expressed as cross talk between the axes. Here the cross talk is defined as a ratio of the main axis amplitude divided by the orthogonal axis amplitude. Here the ratio was 25.3 or 28.0 dB.

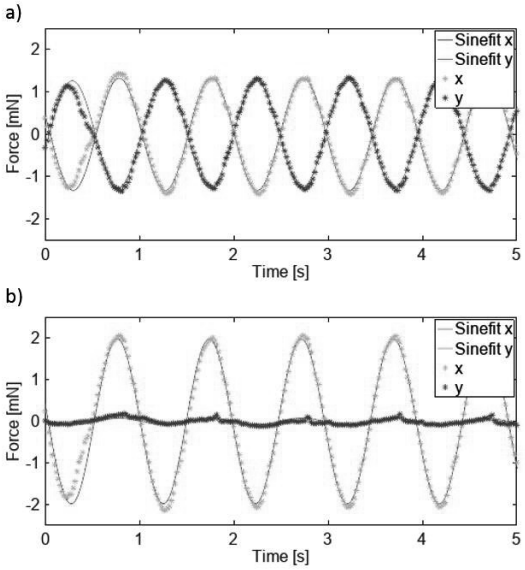

Fig 8. Cross talk (Cross correlation) of a) combined sensor output components in 0 degrees and b) 45 degrees combined signal.

TABLE III. Simulated and measured sensitivities and spring constants.

Parameter	Numerical	Measured
Spring constant 0° [N/m]	209.42	183.08
Sensitivity 0° [V/N]	934.12	932.75
Spring constant 45° [N/m]	209.78	198.48
Sensitivity 45° [V/N]	931.36	826.10

The temperature effect of the sensor was also considered based on literature. It was found that the temperature and humidity have effect on PZT sensitivity [28-31]. However, this was not investigated in this work because especially the proposed biological applications have a high degree of temperature control and used temperature range is small.

As a limitation of the proposed approach, it is noticed that the form factor of the sensor may not be suitable for all proposed applications. For example, the sensor may be too large to be used in single cell level measurements. Also, the operation of the sensor itself is based on linear elastic cantilever, which fixes the spring constant to a certain value. If different mechanical properties are required in the measurement application, the sensor design must be altered accordingly. If miniaturization is desired the sensor electronics and the current PWB approach may not be suitable. In addition, the sensor presented in this work has a prototype nature and the mass production challenges need to be addressed when further developing this force measurement concept. These reasons, and the fact that the sensor is not industrially fabricated but a handmade prototype, are most likely causing large variation in the sensor performance in the case of multiple prototype like sensors are compared. Therefore, certain things such as repeatability was not extensively studied, but the focus was on the sensor design itself. In addition, if for example the repeatability and reproducibility are to be studied in larger context, it involves observing effects such as operator to operator variance. In the future, work on these issues is a very important development aspect and this also involves work on manufacturability to minimize the variance between individual sensor elements. Also, when the sensor fabrication process will be improved to for example reduce sensor-to-sensor variation, it makes it sensible to conduct a series of application measurements and more thorough characterization measurements.

IV. Conclusion

We have demonstrated a dual axis piezoelectric force measurement system capable of measuring forces below 2 mN which was the range of the design input specification. The device studied here has piezoelectric operation principle instead of piezo resistive principle often used in, for example, MEMS sensors. The capability of the developed dual axis force measurement system was demonstrated using an embedded software approach, which provides wide range of possibilities for customized measurement arrangements using open source tools. As an example, measurement of small muscular contraction forces present in in-vitro cardiac tissue constructs is a possible application for the proposed system.

We have also demonstrated an embedded signal processing tool chain with four IIR filters. The filtering successfully removes power line interference and its harmonics from the measurement signal and enables calculating the 2D force components from the four sensor signals. The measurement system was able to carry out 4 channel sampling at 3 kHz sampling frequency and perform the proposed filtering as well as communication with LabVIEW based PC software in real time.

Acknowledgment

This work was funded by the Academy of Finland in the context of “In vitro cardio” -project (grant number 310527) and in the context of “University profiling grant” (grant number 292477).

References

[1] Wei, Y., & Xu, Q. (2015). An overview of micro-force sensing techniques. Sensors and Actuators A: Physical, 234, 359-374.

[2] Krishna, G. M., & Rajanna, K. (2004). Tactile sensor based on piezoelectric resonance. IEEE sensors journal, 4(5), 691-697.

[3] Cotton, D. P., Chappell, P. H., Cranny, A., White, N. M., & Beeby, S. P. (2007). A novel thick-film piezoelectric slip sensor for a prosthetic hand. IEEE sensors journal, 7(5), 752-761.

[4] Lakhmi, R., Debéda, H., Dufour, I., & Lucat, C. (2010). Force sensors based on screen-printed cantilevers. IEEE Sensors Journal, 10(6), 1133-1137.

[5] Wenming, X., & Hui, Z. (2008, January). Bio-manipulation probe integration with micro-force sensor. In 2008 3rd IEEE International Conference on Nano/Micro Engineered and Molecular Systems (pp. 393-396). IEEE.

[6] Saketi, P., Latifi, S. K., Hirvonen, J., Rajala, S., Vehkaoja, A., Salpavaara, T., ... & Kallio, P. (2015). PVDF microforce sensor for the measurement of Z-directional strength in paper fiber bonds. *Sensors and Actuators A: Physical*, *222*, 194-203.

[7] Kim, K., Cheng, J., Liu, Q., Wu, X. Y., & Sun, Y. (2008, January). MEMS capacitive force sensors for micro-scale compression testing of biomaterials. In 2008 IEEE 21st International Conference on Micro Electro Mechanical Systems (pp. 888-891). IEEE.

[8] Qin, Y., Zhao, Y., & Wang, W. (2015, April). Development and characterization of three-axis micro-force sensor series. In 10th IEEE International Conference on Nano/Micro Engineered and Molecular Systems (pp. 103-106). IEEE.

[9] Sasaki, D., Matsuura, K., Seta, H., Haraguchi, Y., Okano, T., & Shimizu, T. (2018). Contractile force measurement of human induced

pluripotent stem cell-derived cardiac cell sheet-tissue. *PloS one*, *13*(5), e0198026.
[10] Wang, L., Dou, W., Malhi, M., Zhu, M., Liu, H., Plakhotnik, J., ... & Hamilton, R. (2018). Microdevice Platform for Continuous Measurement of Contractility, Beating Rate, and Beating Rhythm of Human-Induced Pluripotent Stem Cell-Cardiomyocytes inside a Controlled Incubator Environment. ACS applied materials & interfaces, 10(25), 21173-21183.
[11] Linder, P., Trzewik, J., Rüffer, M., Artmann, G. M., Digel, I., Kurz, R., ... & Artmann, A. T. (2010). Contractile tension and beating rates of self-exciting monolayers and 3D-tissue constructs of neonatal rat cardiomyocytes. Medical & biological engineering & computing, 48(1), 59.
[12] Mannhardt, I., Breckwoldt, K., Letuffe-Brenière, D., Schaaf, S., Schulz, H., Neuber, C., ... & Klampe, B. (2016). Human engineered heart tissue: analysis of contractile force. *Stem cell reports*, *7*(1), 29-42.
[13] Qu, Y., Zhao, F., Wang, X., Liu, J., Li, J., Song, Z., & Wang, Z. (2019). Cardiomyocyte contractile force changes in response to AGRWE detected by AFM. Micro & Nano Letters.
[14] Nagarajan, N., Vyas, V., Huey, B. D., & Zorlutuna, P. (2016). Modulation of the contractility of micropatterned myocardial cells with nanoscale forces using atomic force microscopy. Nanobiomedicine, 3, 1849543516675348.
[15] Pesl, M., Pribyl, J., Acimovic, I., Vilotic, A., Jelinkova, S., Salykin, A., ... & Rotrekl, V. (2016). Atomic force microscopy combined with human pluripotent stem cell derived cardiomyocytes for biomechanical sensing. Biosensors and Bioelectronics, 85, 751-757.
[16] Gaitas, A., Malhotra, R., Li, T., Herron, T., & Jalife, J. (2015). A device for rapid and quantitative measurement of cardiac myocyte contractility. Review of Scientific Instruments, 86(3), 034302.
[17] Virtanen, J., V. Sariola, and S. Tuukkanen. "Piezoelectric cantilever force sensor sensitivity measurements." *Journal of Physics: Conference Series*. Vol. 1065. No. 4. IOP Publishing, 2018.
[18] Badamasi, Y. A. (2014, September). The working principle of an Arduino. In 2014 11th International Conference on Electronics, Computer and Computation (ICECCO) (pp. 1-4). IEEE.
[19] D'Ausilio, A. (2012). Arduino: A low-cost multipurpose lab equipment. Behavior research methods, 44(2), 305-313.
[20] Jayetileke, H. R., De Mei, W. R., & Ratnayake, H. U. W. (2014, December). Real-time fuzzy logic speed tracking controller for a DC motor using Arduino Due. In 7th International Conference on Information and Automation for Sustainability (pp. 1-6). IEEE.
[21] Tibrewala, A., Hofmann, N., Phataralaoha, A., Jäger, G., & Büttgenbach, S. (2009). Development of 3D force sensors for nanopositioning and nanomeasuring machine. Sensors, 9(5), 3228-3239.
[22] Liang, Q., Zhang, D., Coppola, G., Wang, Y., Wei, S., & Ge, Y. (2014). Multi-dimensional MEMS/micro sensor for force and moment sensing: A review. IEEE Sensors Journal, 14(8), 2643-2657.
[23] Kan, T., Takahashi, H., Binh-Khiem, N., Aoyama, Y., Takei, Y., Noda, K., ... & Shimoyama, I. (2013). Design of a piezoresistive triaxial force sensor probe using the sidewall doping method. Journal of Micromechanics and Microengineering, 23(3), 035027.
[24] Microchip corporation, "SAM3X/SAM3A Series embedded 32-bit processor", ATSAM3X8E Data sheet, March 3 2015 [Revised March 23 2015]
[25] Virtanen J., Vehkaoja A., Tuukkanen S.. Piezoelectric dual axis cantilever sensor for dynamic low force measurements on an open source based platform , I3S2019
[26] Matsuya, Y., Uchimura, K., Iwata, A., Kobayashi, T., Ishikawa, M., & Yoshitome, T. (1987). A 16-bit oversampling A-to-D conversion technology using triple-integration noise shaping. IEEE Journal of Solid-State Circuits, 22(6), 921-929.
[27] Harpe, P., Cantatore, E., & van Roermund, A. (2014, February). 11.1 An oversampled 12/14b SAR ADC with noise reduction and linearity enhancements achieving up to 79.1 dB SNDR. In 2014 IEEE International Solid-State Circuits Conference Digest of Technical Papers (ISSCC) (pp. 194-195). IEEE.
[28] Shrout, T. R., & Zhang, S. J. (2007). Lead-free piezoelectric ceramics: Alternatives for PZT?. Journal of Electroceramics, 19(1), 113-126.
[29] Wolf, R. A., & Trolier-McKinstry, S. (2004). Temperature dependence of the piezoelectric response in lead zirconate titanate films. Journal of applied physics, 95(3), 1397-1406.
[30] Gubinyi, Z., Batur, C., Sayir, A., & Dynys, F. (2008). Electrical properties of PZT piezoelectric ceramic at high temperatures. Journal of Electroceramics, 20(2), 95-105.
[31] Fang, M., Rajput, S., Dai, Z., Ji, Y., Hao, Y., & Ren, X. (2019). Understanding the mechanism of thermal-stable high-performance piezoelectricity. Acta Materialia, 169, 155-161..

Juhani Virtanen received his M.Sc. (Tech) degree electronics and telecommunications engineering from Tampere University of Technology, Tampere, Finland in 1994. He has 20 years of industrial work experience in various positions. He is currently a doctoral student with research interests in sensor technology, measurements, physiological measurements and signal processing. He has 9 authored internationally peer reviewed articles and 7 internationally granted patents.

Arno Pammo received his B.Sc. (tech.) from Tampere University of Technology in 2016. Alongside of his master's studies in biomedical engineering, he has been working in research groups in the field of biomeasurements and renewable materials.

Antti Vehkaoja received his D.Sc. (Tech.) degree in automation science and engineering from Tampere University of Technology, Tampere, Finland in 2015. He has authored more than 70 scientific articles. He is currently an assistant professor (tenure tract) of sensor technology and biomeasurements at Tampere University. His research interests include development of embedded measurement technologies for physiological monitoring and related signal processing and data analysis methods with a focus on the assessment of vascular condition.

Sampo Tuukkanen received his P.hD. in applied physics from Department of Physics, University of Jyväskylä, Jyväskylä, Finland, in 2006. He is currently holding Associate Professor (tenure track) position at Tampere University, Tampere, Finland. His research interests are related to biomeasurements and bio-based devices. He has authored over 60 scientific articles, and having the h-index 19 (Google Scholar).

Current Applied Physics 20 (2020) 155–160

Contents lists available at ScienceDirect

Current Applied Physics

journal homepage: www.elsevier.com/locate/cap

Direct measurement of contraction force in human cardiac tissue model using piezoelectric cantilever sensor technique

J. Virtanen[a], M. Toivanen[b], T. Toimela[b], T. Heinonen[b], S. Tuukkanen[a,*]

[a] Faculty of Medicine and Health Technology, Tampere University, Tampere, Finland
[b] FICAM (Finnish Center for Alternative Methods), Faculty of Medicine and Health Technology, Tampere University, Finland

ARTICLE INFO

Keywords:
Cardiomyocyte
Piezoelectric sensor
Cantilever
Contraction force

ABSTRACT

A proof-of-concept method for measuring cardiac tissue contraction force using an in-house-developed piezoelectric cantilever sensor system is demonstrated. Contracting forces of 7.2–16.6 μN (n = 5) were measured from a human cardiac tissue construct. Beating cardiac tissue constructs were monitored in-situ under a microscope during the contraction force measurements. Development of the measurement method allows very low forces such as the ones that appear in biological small scale systems to be determined.

1. Introduction

Cardiotoxicity is one of the leading causes for drug attrition during a drug development process and for post-approval drug withdrawal [1,2]. Animal experiments are poor predictors of drug-induced toxicity in humans [3]. Human stem cell-based tissue and organ models would be more reliable and ethical than experiments on animals [4]. The development of a functional cardiac tissue model requires advanced and controlled cell culture techniques combined with highly sensitive measuring technology. The generation of the contraction force is a key element in the functioning of the heart, so drugs affecting the contraction function of cardiomyocytes pose a potentially high risk for cardiac safety [5]. Therefore, there is an urgent need for a reliable method to measure the contraction force in cardiomyocytes. At present, there are only a few reports in the literature describing varying approaches to overcome this issue [6–10].

Our highly sensitive force sensors were constructed from a metallic cantilever attached to a piezoelectric sensor, which was connected to in-house-built dedicated hardware and a user interface plate. The measurement system was a further development from a previous study [11].

In this paper, we demonstrate a proof-of-concept technique for directly measuring the contraction force of a human cardiac tissue model in-situ under microscope. The measurement method is based on the fact that the piezoelectric sensor detects the movement of the cantilever when it is brought into contact with the cardiac tissue construct.

2. Materials and methods

2.1. Cardiac tissue construct fabrication

The use of human umbilical vein endothelial cells (HUVECs) from scheduled caesarean sections and human adipose stromal cells (hASCs) obtained from surgical operations was approved by the Ethics Committee of the Pirkanmaa Hospital District (permit numbers R08028 and R03058, respectively).

The human-induced pluripotent stem cells (ATCC-BXS0116 hiPSC) were differentiated into cardiomyocytes using a PSC Cardiomyocyte Differentiation Kit (Gibco Invitrogen, A2921201). The cells were maintained at 37 °C and 5% CO_2 in a humidified incubator, and the medium was replaced every 2–3 days.

The cardiac tissue constructs were fabricated by a technique adapted from previous work [12,13]. A punched polydimethylsiloxane (PDMS, Sylgard 184, Dow Corning, USA) sheet was reversibly bonded to a cell culture dish and the holes (d = 5 mm) were coated with fibrinogen (Sigma Aldrich, F3879). The hASCs and HUVECs were propagated separately and a co-culture was formed in the PDMS holes to produce vascular-like networks as previously described in Ref. [14]. Two days later, hiPSC-derived cardiomyocytes were seeded on top of the vascular structures. After cardiomyocyte seeding, a serum-free stimulation medium (SFSM) consisting of DMEM/F12, 2.56 mM L-glutamine, 0.1 nM 3,3′,5-Triiodo-L-thyronine sodium salt, ITS™ Premix: 1.15 μM: 6.65 μg/ml insulin, 6.65 μg/ml Transferrin, 6.65 ng/ml selenious acid, 1% Bovine serum albumin, 2.8 mM Sodium pyruvate, 200 μg/ml Ascorbic acid, 0.5 μg/ml Heparin, 2 μg/ml Hydrocortisone,

* Corresponding author.
E-mail address: sampo.tuukkanen@tuni.fi (S. Tuukkanen).

https://doi.org/10.1016/j.cap.2019.10.020
Received 23 August 2019; Received in revised form 15 October 2019; Accepted 25 October 2019
Available online 28 October 2019

10 ng/ml VEGF, and 1 ng/ml FGF-β as described in Ref. [15] was replaced by a 1:1 Cardiomyocyte maintenance medium (Gibco Invitrogen, A209208) and SFSM. A few days later, the cardiomyocytes regained their contracting function and the PDMS sheets were removed to allow the vascularized cardiac tissue constructs to form spontaneously. This process also detached the edges of the tissue constructs which provided attachment points to the force measurement cantilever. The beating cardiac tissue constructs remained functional over 21 days.

2.2. Piezoelectric cantilever sensors

A piezoelectric cantilever sensor was used to measure the force of the cardiac cell contraction. A cantilever sensor has linear elastic behaviour and is characterized by a spring constant. A piezoelectric sensor element in the cantilever then converts the cantilever strain to electric energy. The operation of the piezoelectric sensor element was first simulated with a finite element method and later the simulation results were verified with actual measurements from the cantilever sensor prototype. The frequency response of the cantilever measurement system was obtained via impulse response measurements. These showed a very good fit with the theoretical computations. Labview software was used to control and capture the results of the measurements obtained with the measurement hardware. The measurement hardware itself consisted of an AD8691 (Analog Devices inc, Norwood, USA), operational amplifier circuit as a buffer amplifier with a voltage amplification of 1. This amplified signal was read with an Arduino Due analog-to-digital converter and then sent through a serial communication link to Labview software [11] for further processing and analysis.

2.3. Finite element simulation of the cantilever

The functionality of the piezoelectric cantilever sensor was simulated with a COMSOL (Comsol AB, Stockholm, Sweden) multiphysics finite element method (FEM) simulator. Both linear elastic and piezoelectric models were used in conjunction with each other in the simulation. In the static simulation a 200 μN force was applied to the tip while the other end was fixed. The total displacement of the tip with this 200 μN load was 192 μm. This represents a cantilever spring constant of 0.96 N/m. In addition, the electric potential field was computed with the simulator on the piezoelectric material. The material parameters were taken from the Lead Zirconate Titanate (PZT) library material. The bottom electrode was fixed to zero electric potential and the electric potential as computed on the top of the piezoelectric element. This potential strength varied between 0.14 and 0.68 V along the piezo material depending on the stress produced when the 200 μN force was applied to the cantilever tip. Furthermore, to obtain the electric potential of the top electrode an average potential over this layer was computed. This average potential was 308 mV and represented the simulated output voltage of the cantilever sensor under a 200 μN load. Thus, the simulated sensitivity was 1.55 kV/N. The deflection of the cantilever beam under the load is illustrated in Fig. 1 a) while the electric field is shown in Fig. 1 b). The simulated and measured sensitivities and spring constants are listed in Table 1.

The piezoelectric cantilever frequency response was also simulated with FEM and later an analytical transfer function model was constructed to model both the mechanical and electrical behaviour of the cantilever measurement system. The modeled and measured frequency response graphs were then compared.

2.4. The prototype cantilever sensor

This sensor element was constructed in-house by soldering a 33 mm long test probe pin (P100-D2-1.5 mm) to a 15 mm diameter circular piezo disc with brass plate thickness of 70 μm and PZT –layer thickness of 50 μm thus a total thickness was 130 μm (Farnell P/N 2667639). The top electrode was located on top of the PZT layer. The piezo disc was

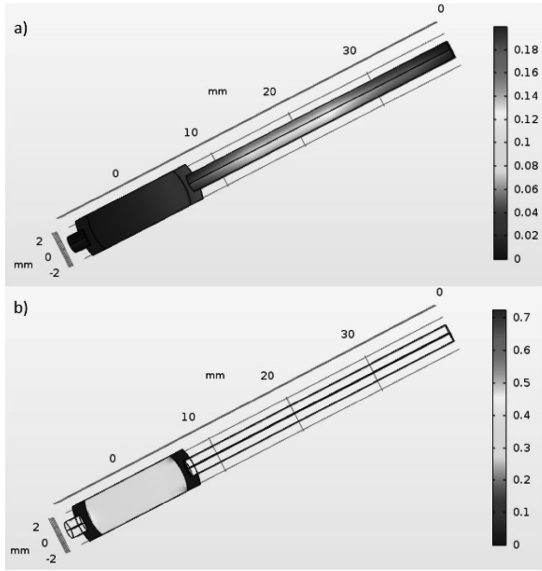

Fig. 1. A FEM computed response with a 200 μN stationary load at the cantilever tip a) total displacement in mm b) electric potential field in Volts.

Table 1
Simulation and calibration results for the cantilever sensor sensitivity.

	Simulated	Measured
Sensitivity	1.55 kV/N	1.97 kV/N
Spring constant	0.96 N/m	0.78 N/m

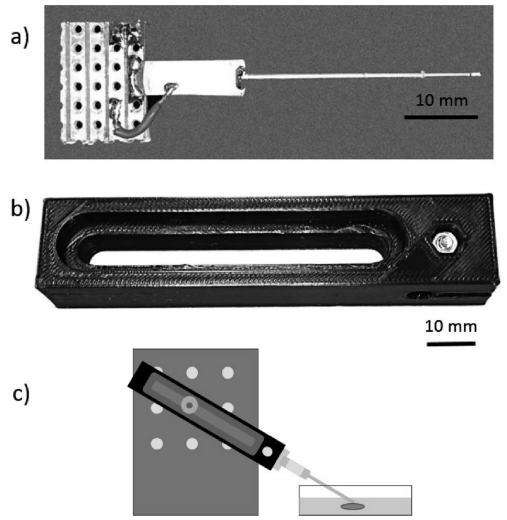

Fig. 2. a) Piezoelectric cantilever sensor probe used in the measurements. b) A 3d-printed mounting fixture for the sensor probe. c) The probe and the arm in the measurement setup.

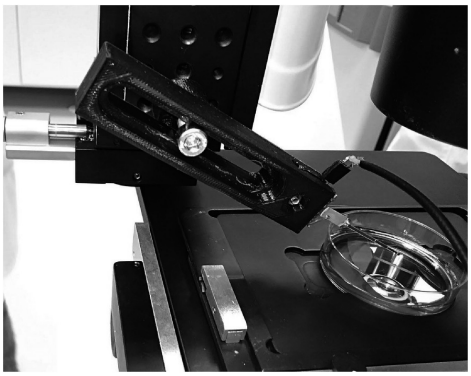

Fig. 3. Cantilever sensor probe attached into the 3-axis micromanipulator to in-situ microscope measurement setup.

further narrowed with a diamond blade cutter to a 5 mm width perpendicular to the orientation of the probe. The cantilever sensor probe prototype is shown in Fig. 2a. The other side of the narrowed piezo disc (ground electrode) was attached to a prototyping wiring board with a solder joint. This formed a fixed point for the cantilever and was also an attachment point to a 3d-printed fixture arm, which is shown in Fig. 2b. This structure was finally attached to a 3-axis linear micro manipulator (Newport Corporation, Irvine, USA) to enable accurate alignment of the probe tip during the measurements (see Figs. 2c and 3). The probe was set to 30° angle to the cultivation dish and the tip was put into the medium as shown in Fig. 2c.

2.5. Cantilever sensor sensitivity measurements

The voltage versus force sensitivities for the prepared cantilever sensors were measured using texture analyser Stable Micro Systems TA. XTPlus (Stable Micro Systems Ltd, Surrey, United Kingdom). In the calibration procedure a 1 Hz sinewave force excitation with 200 μm amplitude was applied to the cantilever tip and the sensor output was measured. This calibration method and data analysis are described in more detail in our previous study [11]. Here, the amplitude of the sensitivity measurement force was 157.5 μN, which yielded a 200 μm displacement and a 329 mV peak voltage reading in the sensor output. Thus, the measured sensitivity of the sensor was 1.97 kV/N and the spring constant of the cantilever 0.78 N/m. The sensor sensitivities from both the simulations and the calibration measurements are summarized in Table 1.

The differences in the simulated and measured sensitivities of the cantilever sensor may be caused by the piezoelectric material's parameters. In the specification sheet for the piezo disc there was no detailed information of the piezoelectric material, so the parameters in our simulation may not be accurate. However this was not a problem since the actual sensor operation was carefully measured.

The standard deviation in the force measurements during calibration was 2.11 μN. This was computed from the deviation from the sinusoidal excitation signal used in the calibration procedure. This is illustrated in Fig. 4a, in which the continuous line represents the excitation signal and the stars show the measurement observations. In Fig. 4b a calibration curve of the sensor is shown. Furthermore, the distribution of the measurement error is shown in Fig. 4c. This shows that the average error (AVG) is 0.47 μN and the standard deviation of the error (STD) is 2.11 μN.

2.6. Impulse response measurement of the cantilever sensor

The impulse response measurement of the system was conducted to ensure that the cantilever measurement was operating in the right frequency range and that the sensitivity measurements could be interlinked in the frequency domain. The impulse response was measured by knocking the sensor element and measuring the time-domain response. This time-domain impulse response is shown in Fig. 5a. The frequency response of the cantilever sensor was then computed by performing a fourier transform on the impulse response data. The comparison of the modeled and measured frequency responses of the measurement system is shown in Fig. 5b. There, the measured and computed responses show that the usable frequency band is ~0.5 Hz–10 Hz with a resonance peak at ~15 Hz.

2.7. In-situ contraction force measurement setup

An optical microscope (Zeiss Primovert, Carl Zeiss AG, Oberkochen, Germany) was used for in-situ characterization of the cardiac tissue constructs during the force measurements. The use of in-situ microscopy was crucial, both for maneuvering the cantilever into its desired position in the selected cardiac tissue constructs, and also for quantifying the synchronised movement of the cantilever and the cardiac tissue construct. The in-situ microscope setup with the cantilever sensor and cell culture dish are shown in Fig. 6.

The contraction force of the cardiac tissue constructs was measured by placing the cell culture dish under the microscope and preparing the sensor probe tip with fibrin coating to enhance its adhesion to the cardiac tissue construct. The coating procedure was to dip the tip into a 5.5 mg/ml fibrinogen solution 5 times and then let it dry for 60 s. Non-coated and PDMS-coated probe tips were also tried, but they did not give reliable measurement results. Altogether, 5 measurements were conducted using this probe measurement system on the cardiac tissue constructs.

3. Results and discussion

3.1. Microscopic analysis of cardiac tissue constructs

Fig. 7 shows an example of a cardiac tissue construct on a cell culture dish 2 weeks after cardiomyocyte seeding. The cardiac tissue construct has not become partially detached from the cell culture dish like the cardiac tissue construct that was used in the measurements. The diameter of the beating cardiac construct was approximately 5 mm and had a circular shape and the contact area of the tip is marked with amber circle.

3.2. In-situ imaging during force measurement

Fig. 8 shows an example of the images captured from one of the videos (in Supplementary material) filmed during the contraction force measurements. There, the cantilever tip and part of a cardiac tissue construct is shown. The contact area of the cantilever tip and the cell construct is approximately 1 mm^2. Furthermore, the supplementary video material shows the synchronous movement of the probe tip and the cell contraction.

Supplementary video related to this article can be found at https://doi.org/10.1016/j.cap.2019.10.020.

The beating frequency computed from the measured data varied between 43 and 49 beats per minute. This corresponds to beating frequencies of between 0.71 and 0.81 Hz, and thus the measurements fall into the usable range of the cantilever frequency band.

3.3. Contraction force measurements

Fig. 9 shows all the 5 force measurements in a time domain with a 5 s period for the measurements. There are systematic beating patterns for the cardiac tissue constructs. Fig. 10 shows individual plots of the measurements where the contracting and relaxing phases of the cardiac

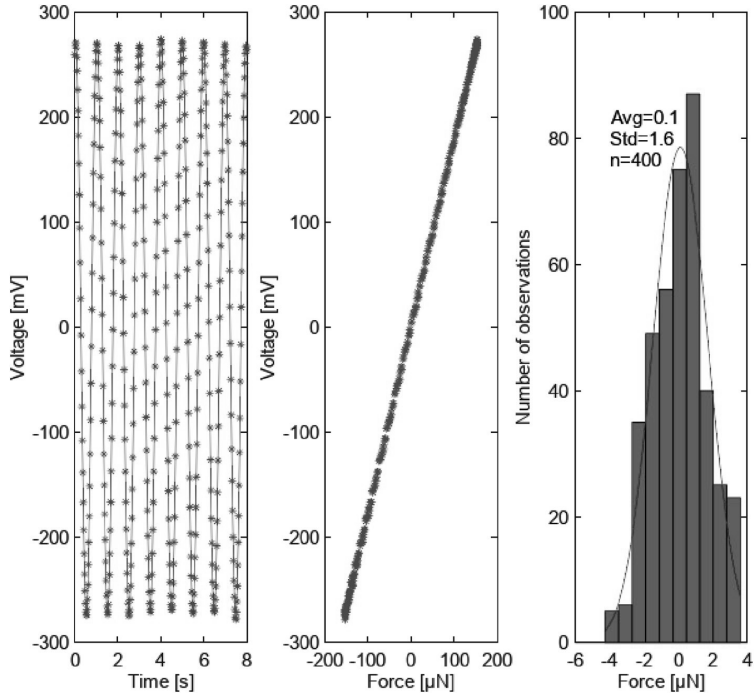

Fig. 4. a) Measurement data fitted to the sinusoidal excitation signal. B) Calibration curve c) Force measurement error distribution.

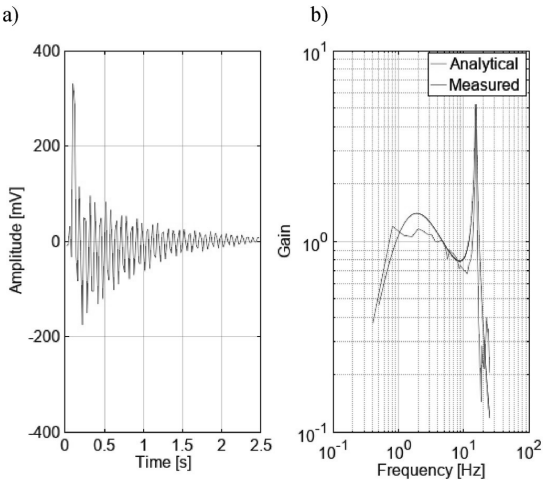

Fig. 5. a) Time domain impulse response of the cantilever measurement system. b) Computed and measured frequency response of the cantilever sensor system in frequency domain.

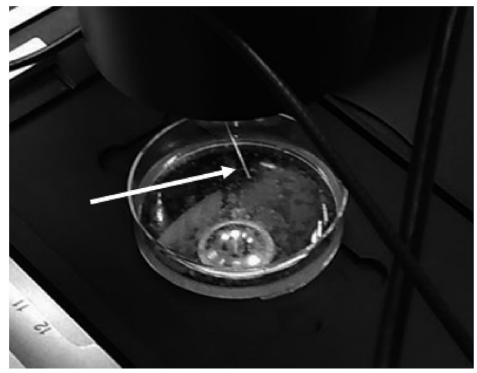

Fig. 6. In-situ measurement setup with a cell culture dish containing the cardiac tissue construct. The measurement cantilever is visible above the Petri dish and marked with the white arrow.

activity can be seen. These stable periodical signals suggest that the fibrin coating enables a good attachment between the tip of the measurement probe and the cardiac tissue construct so that the contracting force is transferred to the probe tip. The beating force from peak to peak of the cardiac tissue construct varied between 7.2 μN and 16.6 μN over the 5 measurements. These values are listed in Table 2 according to the order in which the measurements were taken. As the force measurement results can be considered to be reliable by themselves it should be noted that a biological organism itself may induce variation to the force measurement results. For example the cantilever tip location in the cell construct may be critical in the actual force measurement.

The obtained contraction force measurement results are in line with the previously reported data. Although much higher reported contraction forces have been reported, such as over 1 mN by Sasaki et al. it should be noted that with engineered tissue the total contraction force is a function of the size of the cell population [10]; the larger the cell population, the larger the forces. Accordingly, much lower contraction forces have been recorded right down to the single-cell scale. Such

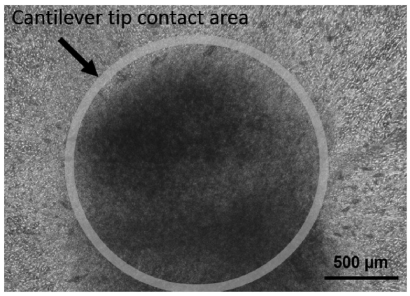

Fig. 7. An example of a cardiac tissue construct 2 weeks after cardiomyocyte seeding with cantilever tip contact area marked with amber circle.

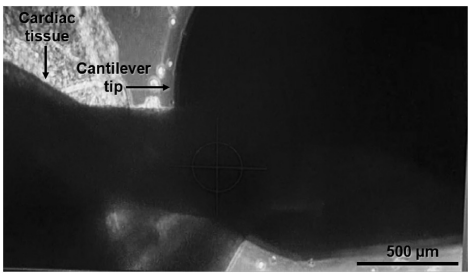

Fig. 8. Microscope image of the cardiac tissue construct and the cantilever during the contraction force measurements. This image is a still from the in-situ video, which is available in the supplementary material.

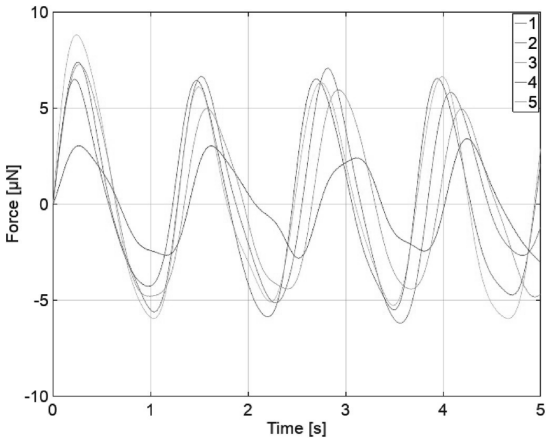

Fig. 9. Contraction force measurement in time domain (all measurements).

small-scale measurements, however, may require cell cultivation directly onto an Atomic Force Microscope (AFM) tip, for example, or onto a dedicated mechanical structure, as described by Linder et al. and Kim et al. [6,9].

In this study, one consideration for the development of this approach is the very concept of force measurement itself. As the elastic force measurement principle combines a force and a displacement measurement, it is important to account for how much the displacement reflects the force measurement readings. This issue is common to any application of this measurement principle, regardless of the scale of the measurement. For example, if the cantilever is very elastic the

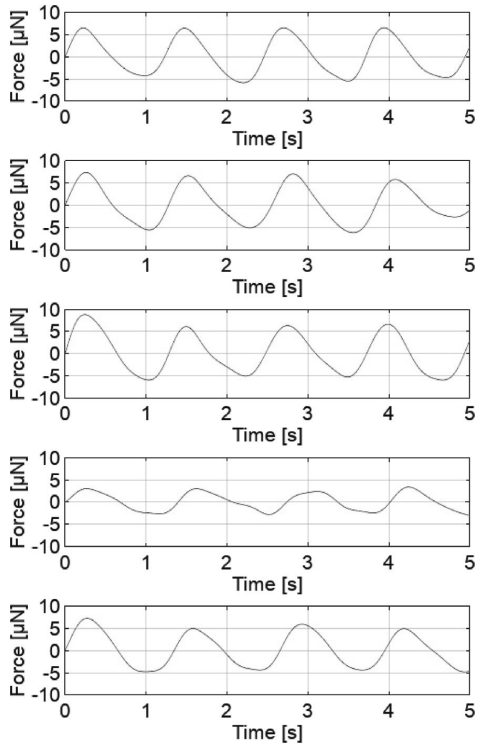

Fig. 10. Individual beating waveforms where the contracting and relaxing phases can be seen.

system may not show the maximum force production, if that is point of interest. Instead, it may more or less measure only the displacement or the movement of the tissue structure. On the other hand, if the probe arrangement is very stiff it may not give any force readings at all as the tissue is too weak to cause any measurable displacement to the tip. Therefore, the role of the spring constant, or the elasticity of the sensor element, become critical. In theory, they need to be tuned to the right range or value to obtain the desired force measurement results. One possibility is to construct a variable load mechanism on the sensor element. With piezoelectric devices, it should be possible to combine a piezoelectric actuator and sensor to provide such a variable load. On the other hand the force measurement probe could be used along with existing force measurement concepts. For example the linear elastic wire video monitoring based measurement (Sidorov et al.) could be replaced with the probe. Potentially simplifying the measurement arrangement. for Nevertheless this is an interesting prospect for the future development of piezoelectric cantilever biomeasurement systems.

The practical arrangements for the force measurement system also require attention. For example, how can the measurements' repeatability be ensured. There are a number of factors that can raise significant challenges for this, not just the sensor itself, but also the mechanism used for attachment to the cells and the properties of the engineered tissue. Repeatability requires standardisation of the cardiac tissue construct itself and its cultivation. Although these challenges have not been much addressed here, it is willingly acknowledged that these are all important considerations if the system is to be applied in, for example, toxicity studies or personalised medicinal applications.

Table 2
Peak To Peak Contraction Force And Recorded Beats per Minute for the 5 Measurements. The Standard Deviation Of The Measurement Error Is 2.11 μN.

Measurement	Peak to peak contraction force [μN]	Beats per minute	Beating frequency [Hz]
1	13.9	48.9	0.81
2	15.2	47.0	0.78
3	16.6	46.9	0.78
4	7.24	43.0	0.71
5	13.6	44.5	0.74

4. Conclusions

In this study we have shown that it is possible to measure cardiac tissue construct contraction forces with a direct force measurement apparatus. The measurements were done with relatively simple devices in a straightforward measurement setup. As this aim of this work was just to prove the concept, there are still many issues to be resolved before this technology reaches its final form. For example, at this stage the method has proved to be suitable only for a multiple cell construct, and is not yet sensitive enough to measure single-cell contraction forces.

However, in this proof-of-concept paper we have demonstrated that a fibrin-coated cantilever connected to a piezoelectric plate sensor can be utilised for measuring cardiac tissue contraction force. The fibrin coating proved itself able to produce reliable force readings, and the measurements of the cells' beating frequency were consistent with the beating frequency obtained from the video (see Supplementary material). The measured cardiac tissue contraction forces from peak to peak ranged from 7.2 to 16.6 μN in amplitude.

Declaration of competing interest

The authors declare that they have no known competing financial interests or personal relationships that could have appeared to influence the work reported in this paper.

Acknowledgement

The authors acknowledge the project funding from the Academy of Finland (grant numbers: 310347 and 310527).

Appendix A. Supplementary data

Supplementary data to this article can be found online at https://doi.org/10.1016/j.cap.2019.10.020.

References

[1] K.E. Lasser, P.D. Allen, S.J. Woolhandler, D.U. Himmelstein, S.M. Wolfe, D.H. Bor, Timing of new black box warnings and withdrawals for prescription medications, J. Am. Med. Assoc. 287 (17) (2002) 2215–2220, https://doi.org/10.1001/jama.287.17.2215.

[2] X. Li, R. Zhang, B. Zhao, C. Lossin, Z. Cao, Cardiotoxicity screening: a review of rapid-throughput in vitro approaches, Arch. Toxicol. 90 (8) (2016) 1803–1816, https://doi.org/10.1007/s00204-015-1651-1.

[3] H. Olson, G. Betton, D. Robinson, K. Thomas, A. Monro, G. Kolaja, P. Lilly, J. Sanders, G. Sipes, W. Bracken, M. Dorato, K. Van Deun, P. Smith, B. Berger, A. Heller, Concordance of the toxicity of pharmaceuticals in humans and in animals, Regul. Toxicol. Pharmacol. 32 (1) (2000) 56–67, https://doi.org/10.1006/rtph.2000.1399.

[4] T.C. Stummann, M. Beilmann, G. Duker, B. Dumotier, J.M. Fredriksson, R.L. Jones, M. Hasiwa, Y.J. Kang, C.-F. Mandenius, T. Meyer, G. Minotti, Y.J.-P. Valentin, B.J. Zünkler, S. Bremer, Report and recommendations of the workshop of the European centre for the validation of alternative methods for drug-induced cardiotoxicity, Cardiovasc. Toxicol. 9 (2009) 107–125, https://doi.org/10.1007/s12012-009-9045-3.

[5] R. Wallis, M. Gharanei, H. Maddock, Predictivity of in vitro non-clinical cardiac contractility assays for inotropic effects in humans — a literature search, J. Pharmacol. Toxicol. Methods 75 (2015) 62–69, https://doi.org/10.1016/j.vascn.2015.05.009.

[6] P. Linder, J. Trzewik, M. Rüffer, G.M. Artmann, I. Digel, R. Kurz, A. Rothermel, A. Robitzki, A. Temiz Artmann, Contractile tension and beating rates of self-exciting monolayers and 3D-tissue constructs of neonatal rat cardiomyocytes, Med. Biol. Eng. Comput. 48 (1) (2010) 59, https://doi.org/10.1007/s11517-009-0552-y.

[7] M.L. Rodriguez, B.T. Graham, L.M. Pabon, S.J. Han, C.E. Murry, N.J. Sniadecki, Measuring the contractile forces of human induced pluripotent stem cell-derived cardiomyocytes with arrays of microposts, J. Biomech. Eng. 136 (5) (2014) 051005, https://doi.org/10.1115/1.4027145.

[8] V. Vyas, N. Nagarajan, P. Zorlutuna, B.D. Huey, Nanostethoscopy: atomic force microscopy probe contact force versus measured amplitude of cardiomyocytic contractions, J. Bionanoscience 11 (4) (2017) 319–322, https://doi.org/10.1166/jbns.2017.1441.

[9] D.-S. Kim, Y.-J. Jeong, B.-K. Lee, A. Shanmugasundaram, D.-W. Lee, Piezoresistive sensor-integrated PDMS cantilever: a new class of device for measuring the drug-induced changes in the mechanical activity of cardiomyocytes, Sens. Actuators B Chem. 240 (2017) 566–572, https://doi.org/10.1016/j.snb.2016.08.167.

[10] D. Sasaki, K. Matsuura, H. Seta, Y. Haraguchi, T. Okano, Tatsuya Shimizu, Contractile force measurement of human induced pluripotent stem cell-derived cardiac cell sheet-tissue, PLoS One 13 (5) (2018) e0198026, , https://doi.org/10.1371/journal.pone.0198026.

[11] J. Virtanen, V. Sariola, S. Tuukkanen, Piezoelectric cantilever force sensor sensitivity measurements, J. Phys. Conf. Ser. 1065 (2018) 042005, , https://doi.org/10.1088/1742-6596/1065/4/042005.

[12] H. Vuorenpää, L. Ikonen, K. Kujala, O. Huttala, J. Sarkanen, T. Ylikomi, K. Aalto-Setälä, T. Heinonen, Novel in vitro cardiovascular constructs composed of vascular-like networks and cardiomyocytes, In Vitro Cell. Dev. Biol. Anim. 50 (2014) 275–286, https://doi.org/10.1007/s11626-013-9703-4.

[13] H. Vuorenpää, K. Penttinen, T. Heinonen, M. Pekkanen-Mattila, J. Sarkanen, T. Ylikomi, K. Aalto-Setälä, Maturation of human pluripotent stem cell derived cardiomyocytes is improved in cardiovascular construct, Cytotechnology 69 (2017) 785–800, https://doi.org/10.1007/s10616-017-0088-1.

[14] T. Toimela, O. Huttala, E. Sabell, M. Mannerström, J.R. Sarkanen, T. Ylikomi, T. Heinonen, Intra-laboratory validated human cell-based in vitro vasculogenesis/angiogenesis test with serum-free medium, Reprod. Toxicol. 70 (2017) 116–125, https://doi.org/10.1016/j.reprotox.2016.11.015.

[15] O. Huttala, H. Vuorenpää, T. Toimela, J. Uotila, H. Kuokkanen, T. Ylikomi, J. Sarkanen, T. Heinonen, Human vascular model with defined stimulation medium - a characterization study, ALTEX 32 (2) (2015) 125–136, https://doi.org/10.14573/altex.1411271.